Southern Ocean Precipitation and Aerosol-Cloud-Precipitation Interactions: A Synthesis of Aircraft Observations, Simple Process Model, and Earth System Model

Litai Kang

A dissertation

submitted in partial fulfillment of the

requirements for the degree of

Doctor of Philosophy

University of Washington

2024

Reading Committee:

Roger Marchand, Chair

Robert Wood

Qiang Fu

Program Authorized to Offer Degree:

Atmospheric Sciences

University of Washington

Abstract

Southern Ocean Precipitation and Aerosol-Cloud-Precipitation Interactions: A Synthesis of Aircraft Observations, Simple Process Model, and Earth System Model

Litai Kang

Chair of the Supervisory Committee:

Roger Marchand

Department of Atmospheric Sciences

Atmospheric Sciences

The Southern Ocean (SO) plays a crucial role in the climate system with ubiquitous low clouds and a preindustrial-like pristine environment. However, accurately representing its aerosols, clouds, and precipitation remains challenging for climate models. Moreover, the properties of SO aerosols and precipitation are not currently well-constrained by satellite observations.

The overarching objective of this dissertation is to characterize precipitation from the SO summertime stratocumulus using aircraft observations collected during the Southern Ocean Clouds Radiation Aerosol Transport Experimental Study (SOCRATES), and study sources and

sinks of SO aerosols using both a simple theoretical budget model and simulations from the Energy Exascale Earth System Model (E3SM) run at high-resolution for a climate model, about 3 km.

In Chapter 2, data from airborne radar, lidar, and in situ probes are used to derive liquid precipitation properties based on a hierarchy of retrieval methods from simple Z-R relationships to more complex radar reflectivity-velocity and radar-lidar retrievals. The retrieved rain rate from all three methods shows good agreement with in-situ aircraft estimates, with rain rates typically being quite light (<0.1 mm hr^{-1}). The derived data are further used to study the vertical distribution of a variety of precipitation properties and to examine the dependence of rain rate on cloud depth and aerosol concentration.

In Chapter 3, a simple source-and-sink budget model for cloud droplet number (N_d) is constrained by aircraft observations and is used to examine the relative influence of processes that determine N_d in SO stratocumulus clouds. The model predicts N_d with little bias and a correlation coefficient of ~0.7 compared with observations. Coalescence scavenging is found to be an important sink of CCN in precipitating stratocumulus and reduces the predicted N_d by as much as 90% depending on the precipitation rate. I also find that the free tropospheric aerosol controls N_d more strongly than the surface aerosol source during the austral summer.

In Chapter 4, a diverse set of simulations and observations are used to evaluate and untangle biases in E3SMv2 simulated clouds, aerosols, and sulfur aerosol species. The default E3SMv2 underestimates cloud droplet numbers and aerosol concentration when compared with observations. Updating the DMS emission and chemistry improves agreement between the model and the observations in cloud droplet numbers and boundary layer aerosols, though biases remain in the free troposphere aerosols, likely attributable to insufficient particle growth, and in simulated sulfur species, due to incomplete DMS chemistry.

TABLE OF CONTENTS

LIST OF FIGURES

LIST OF TABLES

Chapter 1 Introduction

Surrounding Antarctica, the Southern Ocean (SO) is the second smallest of the five ocean basins, yet it plays an outsized role in the climate system. The SO is estimated to account for about 75% of the oceanic heat uptake and about 30-40% of the carbon uptake (Frölicher et al., 2015; Khatiwala et al., 2009), and thus acts as a strong buffer against climate change.

The SO is one of the cloudiest places on Earth, with an annual mean cloud fraction over 80% (Kay et al., 2012; Matus and L'Ecuyer, 2017) and ubiquitous low clouds (Huang et al. 2016; Grise and Medeiros; 2016; Mace et al., 2020). These clouds are of critical importance to the climate because they reflect solar shortwave radiation back to space, cooling the planet, locally reducing heat uptake by the ocean (Sallée et al. 2013, Schneider and Reusch 2016) and profoundly affecting global ocean and atmospheric circulations. SO low clouds influence the position of the Southern Hemisphere midlatitude jet (Ceppi et al. 2012, 2013), cross-hemispheric energy transports and the position of the Inter-Tropical Convergence Zone (ITCZ) (Hwang and Frierson 2013, Kay et al 2016), and cloud feedbacks and global climate sensitivity (Gettelman et al 2019, Zelinka et al. 2020).

Moreover, due to the remoteness of the SO, clouds in such a pristine environment can be sensitive to aerosol changes, making the SO a unique natural laboratory to study aerosol-cloud interactions (ACI). Arguably, the SO can serve as a modern surrogate for aerosol conditions in the pre-industrial era (Hamilton et al. 2014). A better understanding of aerosols in the preindustrial era is needed to constrain the radiative forcing from anthropogenic aerosols during the industrial era (Carslaw et al., 2013; Ghan et al., 2013; McCoy et al., 2020).

Aerosols and precipitation play a key role in shaping low cloud cover and cloud microphysical properties, and ultimately the cloud radiative impact (Wood, 2012). In liquid phase clouds, cloud droplet number concentrations are largely controlled by the concentration of boundary layer aerosols that serve as cloud condensation nuclei (CCN), while subsequent collision-coalescence of cloud droplets leads to precipitation, removes cloud water, and reduces the aerosol concentration and number of available CCN. The removal of aerosols by their activation into cloud droplets and their merger into precipitation-sized particles through collision-coalescence, hereafter coalescence scavenging, has long been recognized as a leading (if not the dominant) mechanism by which aerosols are removed from the lower atmosphere (Feingold et al. 1996, Wood et al. 2012). This includes the Southern Ocean, where aircraft observations have shown that aerosols which serve as CCN have lower concentrations in the boundary layer under cloudy conditions than clear conditions (Hudson et al. 1998, Yum et al. 2004).

Satellite observations show that SO low clouds have significant seasonal and latitudinal dependencies. Low clouds have higher mean droplet number concentrations(N_d) and smaller effective radii on average during the SO summer than during the winter, as well as higher droplet concentrations (and smaller effective radii) as one approaches Antarctica (south of 55° to 60°S) (McCoy et al. 2014, 2020; Mace et al., 2023). However, previous studies reveal that climate models systematically underestimate N_d over SO in austral summer (McCoy et al., 2020; Zhou et

al. 2021; Atlas et al., 2020; Tang et al., 2023), highlighting the need to understand the model deficiency with detailed analysis.

Aerosols in the pristine summertime SO marine boundary layer are primarily sourced from natural origins, including: (1) primary sea spray aerosols, consisting largely of sea salt with varying amounts of organics, generated through sea spray and bubble bursting from the ocean surface, and (2) secondary sulfate and organic aerosols, formed from biogenic volatile sulfurous and organic compounds, such as dimethyl sulfide (DMS) (McCoy et al., 2015; Fossum et al., 2018; Revell et al., 2019; Humphries et al., 2023; Sanchez et al., 2021). Sea spray aerosols, which are strongly wind-driven, have a significant impact on the SO accumulation and coarse mode aerosols, especially during austral winter (Humphries et al., 2023; Chubb et al., 2016). The overall seasonal cycle of the SO CCN is closely linked to ocean biology-sourced secondary aerosols, with CCN peaking in the biologically-active austral summer and reaching a minimum in winter (Ayers and Gras, 1991; Korhonen et al., 2008; Humphries et al., 2023). In particular, DMS is an abundant natural source of sulfur (Bates et al., 2004; Chen et al., 2018), and is found to be closely related to cloud properties (e.g., Charlson et al., 1987; Ayers and Gras, 1991; Korhonen et al., 2008; Mahajan et al., 2015; Hopkins et al., 2023).

On the other hand, differences in aerosol sources compete with precipitation sinks in explaining the latitudinal dependence, and may play a role in the seasonal cycle. Using a simple budget model (Wood et al. 2006) in combination with CloudSat-derived estimates for precipitation, McCoy et al. (2020) find that the observed latitudinal gradient in stratocumulus cloud droplet number can be reasonably explained by increases in coalescence scavenging. Specifically, McCoy et al. (2020) suggests that coalescence scavenging may drive down the mean N_d to about 30% of the value that would occur without coalescence scavenging over the SO storm track, while poleward of the storm track (65°S), its influence is weaker, perhaps reducing N_d to only about 70% of the value that would occur without this sink. There is little doubt that aerosols from biological sources (and DMS in particular) play a large role in both the aforementioned seasonal and latitudinal variations in shallow SO cloud droplet number concentrations. However, coalescence scavenging is likely equally important as the largest sink of CCN, and its influence over the SO remains poorly understood.

In addition to its effect on cloud and aerosol, precipitation is important to the surface energy budget and is a major source of freshwater into the SO (Pauling et al. 2016). Changes in the input of freshwater via precipitation into the SO alongside with melting glacier around the Antarctica are believed to be responsible for freshening of the SO in recent decades, and this is thought to be causing stronger ocean stratification, a reduction in oceanic vertical heat transfer and surface cooling which has contributed to an increase in sea ice cover (de Lavergne et al., 2014; Pauling et al., 2016; Swart et al., 2018; Pan et al., 2022).

Due to the remoteness of the SO and a general lack of surface and in situ observations, satellite observations have long been an indispensable tool to study SO precipitation. Arguably the best available source of satellite data on SO precipitation rates is provided by CloudSat (W-band radar), which has greater sensitivity to light precipitation than passive sensors (Tansey et al., 2022, Eastman et al., 2019). CloudSat has provided an unprecedentedly broad picture of SO precipitation: Ellis et al. (2009) showed that the precipitation occurrence frequency peaks around

50°-60°S; Mitrescu et al. (2010) found that the SO has a high occurrence of very light precipitation with rain rates smaller than 1 mm h^{-1} having a frequency of 15%. Although compared to other satellite measurements, CloudSat better detects light precipitation and is better able to determine the rain rate, CloudSat is nonetheless affected by ground clutter which severely corrupts the reflectivity measurements within about 750 m of the surface (Marchand et al., 2008). CloudSat precipitation retrievals are also largely limited to situations where the measured near-surface (750 to 1000m) reflectivity is larger than -15 dBZ (Haynes et al., 2009), although the precipitation is often observed falling from SO clouds with reflectivity factors less than -15 dBZ (e.g., Mace and Protat, 2018). As shown by Tansey et al. (2022), who evaluated CloudSat retrievals using surface precipitation measurements during the Macquarie Island Cloud Radiation Experiment (MICRE), the CloudSat 2C-Precip-Column product misses most precipitation with a precipitation rate less than 0.5 mm hr^{-1}. In addition, CloudSat radar reflectivity measurements provide very limited information regarding the phase of the precipitation. The current operational CloudSat precipitation products categorize precipitation into liquid, snow, or mixed phase based largely on temperature profiles extracted from ECMWF analysis and identifying melting layers, rather than any directly measured quantity.

The overarching objective of this dissertation is to characterize precipitation from the SO summertime stratocumulus using aircraft observations collected during the Southern Ocean Clouds Radiation Aerosol Transport Experimental Study (SOCRATES), and to study sources and sinks of SO aerosols using both a simple theoretical budget model and simulations from the Energy Exascale Earth System Model (E3SM) run at high-resolution about 3 km. More specifically:

- Chapter 3 provides characterization of in-and-below cloud precipitation properties using a combination of SOCRATES Doppler cloud radar, High-spectral-resolution lidar (HSRL) and in situ observations.
- Chapter 4 uses a simple source-and-sink budget model for cloud droplet number (N_d) constrained by aircraft observations to examine the relative influence of processes that determine N_d in SO stratocumulus clouds.
- Chapter 5 uses a diverse set of simulations and observations are used to evaluate and untangle biases in E3SMv2 simulated clouds, aerosols, and sulfur aerosol species, and seek pathways for model improvement through observation-informed analysis and sensitivity tests.
- Chapter 6 provides conclusions and discusses avenues for future work.

Chapter 2 Stratocumulus Precipitation Properties over the Southern Ocean Observed from Aircraft during the SOCRATES campaign

2.1 Introduction

Surrounding Antarctica, the Southern Ocean (SO) is the second smallest of the five ocean basins, yet it plays an outsized role in the climate system. The SO is estimated to account for about 75% of the oceanic heat uptake and about 30-40% of the carbon uptake (Frölicher et al., 2015; Khatiwala et al., 2009), and thus act as a strong buffer against climate change. Due to the lack of anthropogenic aerosols, the SO is also a pristine environment, and it has been argued that SO observations can be used as a present-day proxy for pre-industrial conditions as regards trying to constrain anthropogenic aerosol effects (Hamilton et al., 2014; McCoy et al., 2020), which remain a large source of uncertainty in the climate projections (Lee et al., 2016; Bellouin et al., 2020). More generally, SO clouds, especially low clouds, also have attracted much research interest in recent years because of their importance to the global radiative energy budget (Trenberth and Fasullo, 2010; Bodas-Salcedo et al., 2016; Cesana et al., 2022) as well as cloud feedbacks and climate sensitivity (Tan et al., 2016; Zelinka et al., 2020; Mülmenstädt et al., 2021).

Precipitation impacts stratocumulus behavior via complex feedbacks that operate on both macrophysical and microphysical scales (Wood, 2012), and has been found to be a key player in the transition of stratocumulus regimes, from closed cells to open cells, and the maintenance of open cells, at least in subtropical stratocumulus (Wang and Feingold, 2009; Yamaguchi and Feingold, 2015; Smalley et al., 2022). Moreover, recent studies highlight the importance of precipitation formation as a dominant sink of cloud condensation nuclei and its control on the cloud droplet number over the SO (McCoy et al., 2020; Kang et al., 2022). Despite the importance of precipitation in low clouds, many climate models and reanalysis data struggle to accurately represent precipitation, including over the SO (Zhou et al., 2021). Mülmenstädt et al. (2021) point out that precipitation biases persist in CMIP6 models, with warm clouds precipitating too frequently, thus shortening cloud lifetime and underestimating their cooling effect. This problem is especially pernicious for the SO because the error grows in importance, with a reduction in mixed-phase clouds as the climate warms (Bjordal et al., 2020).

Due to the remoteness of SO and a general lack of surface and in situ observations, satellite observations have long been an indispensable tool to study SO precipitation. Arguably the best available source of satellite data on SO precipitation rates is provided by CloudSat (W-band radar), which has greater sensitivity to light precipitation than passive sensors (Tansey et al., 2022, Eastman et al., 2019). CloudSat has provided an unprecedentedly broad picture of SO precipitation: Ellis et al. (2009) showed that the precipitation occurrence frequency peaks around 50°-60°S; Mitrescu et al. (2010) found that the SO has a high occurrence of very light precipitation with rain rates smaller than 1 mm h^{-1} having a frequency of 15%; Mace and Avey (2017) using both CloudSat and Moderate Resolution Imaging Spectroradiometer (MODIS) data

found that precipitation processes in SO warm clouds vary seasonally with a stronger precipitation susceptibility to cloud droplet number in winter. Although compared to other satellite measurements, CloudSat better detects light precipitation and is better able to determine the rain rate, CloudSat is nonetheless affected by ground clutter which severely corrupts the reflectivity measurements within about 750 m of the surface (Marchand et al., 2008). CloudSat precipitation retrievals are also largely limited to situations where the measured near-surface (750 to 1000m) reflectivity is larger than -15 dBZ (Haynes et al., 2009), although the precipitation is often observed falling from SO clouds with reflectivity factors less than -15 dBZ (e.g., Mace and Protat, 2018). As shown by Tansey et al. (2022), who evaluated CloudSat retrievals using surface precipitation measurements during the Macquarie Island Cloud Radiation Experiment (MICRE), the CloudSat 2C-Precip-Column product misses most precipitation with a precipitation rate less than 0.5 mm hr^{-1}. In addition, CloudSat radar reflectivity measurements provide very limited information regarding the phase of the precipitation. The current operational CloudSat precipitation products categorize precipitation into liquid, snow, or mixed phase based largely on temperature profiles extracted from ECMWF analysis and identifying melting layers, rather than any directly measured quantity.

In the face of biases and uncertainty in satellite retrievals and modeling, precipitation observations from multiple sources such as islands, ships, and aircraft provide us with an important opportunity to obtain a more detailed view of SO precipitation. Such precipitation observations were made in several recent collaborative field campaigns (McFarquhar et al., 2021), including the aforementioned MICRE during 2016-2018, the Clouds Aerosols Precipitation Radiation and atmospheric Composition over the Southern Ocean (CAPRICORN) campaign in 2016 and 2018, the Measurements of Aerosol, Radiation, and Clouds over the Southern Ocean (MARCUS) campaign during 2017-2018, and the Southern Ocean Cloud Radiation and Aerosol Transport Experimental Study (SOCRATES) during Jan-Feb 2018. For example, Tansey et al. (2022) created a 1-year "blended" surface precipitation dataset (which combines W-band radar, tipping buck and disdrometer data) for MICRE and used these data to study the diurnal, synoptic, and seasonal variability of near-surface precipitation. These authors found that total accumulation was comprised of about 74% rain, 16% ice or mixed phase precipitation, and 10% small particle precipitation (whose phase could not be determined). In a study based on the CAPRICORN datasets, Montoya Duque et al. (2022), applied a K-means clustering technique to radiosonde data to classify the atmosphere into seven thermodynamic clusters, and found that the highest occurrence of surface precipitation was associated with warm frontal clusters and high-latitude cyclone clusters (poleward of the polar front near cyclones), with warm rain dominating in the former and the largest fraction of snow in the latter. Shipborne precipitation observations from CAPRICORN have also been included along with observations from other research vessels in the Ocean Rain and Ice-Phase Precipitation Measurement Network (OceanRAIN), the first global and comprehensive along-track in-situ water cycle surface reference dataset (Klepp et al., 2018). Protat et al. (2019a,b) used OceanRAIN data to investigate discrepancies among satellite products at high latitudes and found large latitudinal and convective-stratiform variability in the drop size distribution (DSD). Protat et al. (2019a) pointed out that the Southern hemisphere's high latitudes stood out as regions with a systematically higher frequency of occurrence of light precipitation with rates < 1 mm h^{-1}. Protat et al. (2019a) also noted that the shape parameter μ for the precipitation drop size distribution (DSD) in high latitudes and midlatitudes ranges from -1 to 1, which is lower than the assumed μ of 2 or 3 in the Global Precipitation Measurement Mission (GPM) rainfall algorithms (Grecu et al., 2016; Seto et

al., 2013). Protat et al. (2019b) found that the Southern Hemisphere high latitude (−67.5°S to −45°S), along with Northern Hemisphere polar latitude bands, stood out with a fundamentally different relationship between radar observables and rainfall properties, such as radar reflectivity to rain rate (Z-R) relationship, mainly because of much lower rain rates over the SO, suggesting that specific relationships are needed for these regions.

In this study, we use data collected during SOCRATES to study the precipitation properties of austral summertime SO stratocumulus, leveraging observations from airborne W-band HIAPER Cloud Radar (HCR), High Spectral Resolution Lidar (HSRL), and in situ probes. In particular, we examine the occurrence of liquid and ice phase precipitation, and for liquid precipitation we derived precipitation properties such as rain rate, using a hierarchy of retrieval methods from simple Z-R relationships to a more complex radar reflectivity-velocity retrieval (ZV retrieval) and radar-lidar retrieval. We also apply the precipitation observations and retrievals to study the in-and-below cloud precipitation properties and rain rate dependence on cloud depth and aerosol concentration.

This chapter is organized as follows: Section 2.2 introduces the datasets, instruments, as well as the analysis and retrieval methods used in this study. Section 2.3 provides a campaign overview and discusses phase partitioning. Section 2.4 examines Z-R relationships and liquid precipitation retrievals and compares these remote sensing data to in situ measurements. Section 2.5 provides a statistical summary of the liquid precipitation properties, and Section 2.6 explores the relationship of stratocumulus rain rate with cloud depth and aerosol concentration, ending with conclusions in Section 2.7.

2.2 Data and Methods

In this section, we introduce the data and methods that we use to characterize in-and-below cloud precipitation properties. Section 2.2.1 describes the SOCRATES campaign sampling strategies, remote sensors (W-band Cloud Radar, HCR, and High Spectral Resolution Lidar, HSRL), and in situ instruments. Section 2.2.2 describes how we use in situ data to analyze in-cloud and below-cloud precipitation properties, as well as how we estimate Z-R relationships. In section 2.2.3, we describe reflectivity-velocity (ZV) and radar-lidar retrievals.

2.2.1 Instrumentation and data

In this study, we use data collected during the SOCRATES campaign to study the precipitation properties of stratocumulus. The SOCRATES campaign happened in January-February 2018 (McFarquhar et al., 2021), when the NSF/NCAR Gulfstream GV aircraft conducted 15 research flights over the SO. After taking off from Hobart (Tasmania), the aircraft typically flew south at high altitude and then descended to just above cloud top for several 10's of minutes, before heading back towards Hobart. On the return, the aircraft would descend into low clouds and sample aerosols, clouds, and precipitation with a repeating series of activities that included in-, below-, and above-cloud level legs (where the aircraft flew at a nearly fixed altitude), as well as sawtooth legs (where the aircraft ascended or descended through the cloud layer). Figure 2.1 shows a schematic of the typical flight, as well as the 15 flight tracks flown during SOCRATES.

To characterize in-and-below cloud precipitation properties, we use observations from both in situ probes and remote sensors. Table 2.1 gives a summary of the instruments and data we use in this study, along with a primary reference. We describe how these in situ data are used in Section 2.2.2.

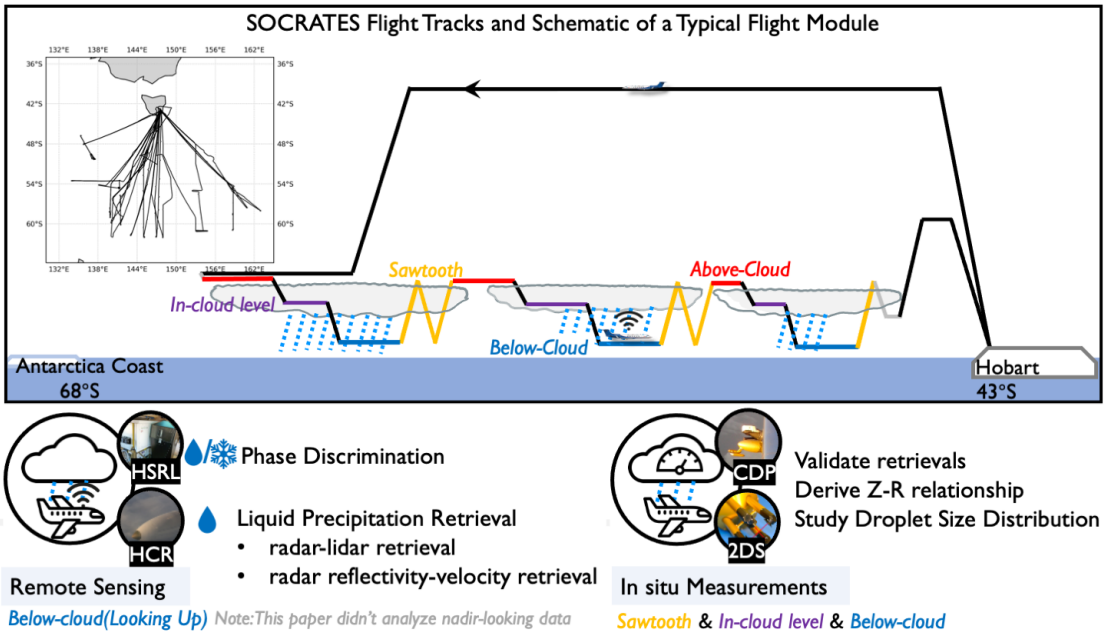

Figure 2.1 A schematic showing the typical flight module during the SOCRATES campaign (with flight tracks map embedded). The black lines show the flight tracks, with different segments highlighted: below-cloud level legs in blue; above-cloud level legs in red; sawtooth legs in yellow; and in-cloud level legs in purple. The graphics below the schematic summarize the main instruments and how the remote sensing and in situ data from different segments were used in this study

Table 2.1 Instruments and Data

Instruments	Data	References
Cloud Droplet Probe (CDP)	Size and concentration of hydrometeors with a diameter between 2-50 µm	Lance et al. (2010) https://data.eol.ucar.edu/dataset/552.002
Two-Dimensional Stereo probe (2DS)	Size and concentration of hydrometeors with a dimension between 10-1280 µm.	Wu and McFarquhar (2019) https://data.eol.ucar.edu/dataset/552.047
Ultra-High-Sensitivity Aerosol Spectrometer	Aerosols with dry diameters between 60 and 1,000 nm	DMT(2013); Sanchez et al. (2021) https://data.eol.ucar.edu/dataset/552.002

(UHSAS)		
CDP, 2DS, Two-Dimensional Optical Array Cloud Probe (2DC), and Rosemount Icing Detector (RICE)	Cloud Phase Product	D'Alessandro et al. (2022) https://data.eol.ucar.edu/dataset/552.142
HIAPER Cloud Radar (HCR)	Reflectivity, Doppler velocity, Spectral width, Signal to noise ratio, etc.	Vivekanandan et al. (2015) https://data.eol.ucar.edu/dataset/552.034
High Spectral Resolution Lidar (HSRL)	Backscatter coefficient, Particle Linear Depolarization Ratio, Extinction coefficient, etc.	Eloranta (2005) https://data.eol.ucar.edu/dataset/552.034

Note: For both CDP and 2DS data are available at 1Hz temporal resolution. CDP data can be found in SOCRATES Navigation, State Parameter, and Microphysics Flight-Level Data. This study uses version 1.4 of this dataset. This study uses version 1.1 of the 2DS dataset, where the raw image data were processed to determine the shape/habit of each particle by the Holroyd scheme in the University of Illinois/Oklahoma Optical Probe Processing Software (UIOOPS, McFarquhar et al. 2018). Cloud Phase Product version 1.0 is also available at 1Hz temporal resolution. The radar and lidar moments data version 3.1 were processed by NCAR/EOL and 2 Hz (0.5 seconds) temporal resolution and 19 meters range vertical resolution. The operational specifications of HCR and HSRL are available at https://data.eol.ucar.edu/dataset/552.034.

Remote sensors include a 94-GHz W-band HIAPER Cloud Radar (HCR) (Vivekanandan et al., 2015) and a 532-nm High Spectral Resolution Lidar (HSRL) (Eloranta, 2005). Based on radar and lidar moments data, we use retrieval techniques to derive precipitation properties, as detailed in section 2.2.3. HCR and HSRL were deployed in previous campaigns, such as CSET (e.g. Schwartz et al., 2019). The radar and lidar data were processed by NCAR/EOL at 2 Hz (0.5 seconds) temporal resolution and have 19 m vertical range resolution. A description of the NCAR/EOL data processing and corrections are given in readme files that are distributed with the data (https://data.eol.ucar.edu/dataset/552.034). This includes a correction of radial velocity for platform motion following Romatschke et al. (2021), in which corrections are applied to the nadir and zenith pointing data separately. For nadir pointing data, radial velocity was corrected following Ellis et al. (2019), where the radial velocity of the surface (assumed to be 0 m/s) is used as a reference to correct the data with a running 3rd-degree polynomial filter. A similar method is applied to the zenith-pointing data, which is the focus of this paper. But for the zenith pointing data, instead of assuming zero velocity of surface, it is assumed that the cloud top velocities from zenith pointing times are similar to those of the neighboring nadir pointing times. Specifically, cloud top velocities are first calculated for both the nadir pointing data and zenith pointing data, then the difference between the two is used to correct the bias in the zenith pointing velocity data. Appendix Figure A1 shows an example of the zenith-pointing velocity fields before and after the correction. Appendix Figure A2 shows the averaged nadir pointing

and zenith pointing velocity profiles from RF13, demonstrating that correction has removed the offset in zenith pointing velocity profiles and resulted in a similar velocity profile between nadir pointing data and zenith pointing times with cloud top velocities around 0 m/s and similar vertical variations.

2.2.2 In situ Measurements

2.2.2.1 Droplet size distribution and phase

This study uses in situ measurements mainly from two particle-sizing-instruments: a Cloud Droplet Probe (CDP) and a Two-Dimensional Stereo probe (2DS) as listed in Table 2.1. We focus on in situ measurement from these legs (as marked in Figure 2.1): below-cloud level legs, in-cloud level legs, and sawtooth legs (which are further divided into top-half of the cloud, bottom-half of the cloud, and the below-cloud portion as described below). These in situ measurements will be used to derive reflectivity to rain rate relationships (Z-R) relationships (section 2.4.1), to validate the liquid precipitation retrievals (section 2.4.3), and to study in-and-below cloud liquid precipitation properties (section 2.5). In our analysis, we only consider the DSD when the in situ phase identification is liquid only by using the 1Hz SOCRATES Cloud Phase Product developed by D'Alessandro et al. (2021, 2022). The details of the phase classification are described in D'Alessandro et al. (2021), and is based on measurements from 2DS, CDP, and Rosemount Icing Detector (RICE) instruments. In brief, a multinomial logistic regression is used to identify periods when non-spherical particles (indicative of ice) are present in the 2DS images, and periods with low cloud droplet number concentrations from the CDP that contains no indication of icing (due to supercooled liquid) from the RICE are likewise identified as containing ice.

We combine measurements from CDP and 2DS to create a combined droplet size distribution (DSD) by using CDP measurements for bins < 25μm and 2DS for bins > 50 μm. For drops in the intermediate size range (25–50 μm), we take the larger values of the two probes. After combining the DSD from two probes, we further averaged the DSD for different regions and flight segments. Specifically, we examine the top half of the cloud layer from sawtooth legs; the bottom half of the cloud layer from sawtooth legs; the below-cloud portion of the sawtooth legs; the below-cloud level legs in 20s intervals; and in-cloud level legs in 10s intervals. For the purpose of averaging the in-situ data into these categories, we define the aircraft as in-cloud when the liquid water content was greater than 0.03 g m^{-3} (Wood et al., 2011; Kang et al., 2021). Because of the limited sampling volumes of the probes, even with averaging, there can be gaps (and large variability) in the DSD distribution for large particles (where the concentrations are sufficiently low that the probes become increasingly unlikely to observe these particles in a given 10 or 20s period). As needed, we fill gaps in the DSD by fitting an exponential curve following Comstock et al. (2004) and extrapolate DSD (out to a diameter of 2000 μm) to account for the contribution from larger particles.

The DSD measurements from CDP and 2DS exhibit various sources of uncertainty as regards particle droplet size and concentration, and these uncertainties propagate, influencing the accuracy of higher moments derived from the DSD (e.g. liquid water content, LWC). For CDP, common issues include undercounting errors and oversizing errors due to coincidence (Lance et al., 2010). Faber et al. (2018) demonstrated that CDP may overestimate the median diameter by

5-15%, with errors in higher-order moments generally below 10%. Faber et al. (2018) also compared CDP-derived LWC with the Nevzorov hot-wire probe and found that LWC_{CDP} is greater by about 20 % larger than that from the Nevzorov hot-wire. Wang et al. (2020) conducted a comparison of LWC measurements between CDP and the independent King probe (a hot-wire probe) during SOCRATES, and found that LWC from two probes is broadly consistent, with a root mean square error of 0.057 g m^{-3} and correlation coefficient of 0.96. On the other hand, 2DS has large uncertainty related to the depth of field for droplets smaller than 50 μm (D'Alessandro et al., 2021). In our analysis, we primarily rely on CDP measurements for particles smaller than 50 μm when combining the DSD data from 2DS and CDP, as described earlier in this section. While the merging does introduce an uncertainty in the effective radius of about 0.5 microns (see Kang et al. 2021), the LWC is dominated by the small droplets measured by the CDP droplets, and the uncertainty in the LWC is likewise dominated by the uncertainty in the CDP. Another potential issue highlighted by O'Shea et al. (2016) is the limited sampling volume of the 2DS probe when operating at low concentrations. To address this, we mitigate the concern by averaging over 10s or 20s periods, as mentioned above.

2.2.2.2 Liquid precipitation properties

Liquid precipitation properties are derived using the DSD. For different segments, we calculated the rain rate (liquid water flux) as:

$$R = 3600 * \frac{\pi}{6}\rho_w \int_{D_{min}}^{\infty} n(D)\, D^3\, v_f(D) dD \tag{2.1}$$

where ρ_w is the density of liquid water (1000 kg m^{-3}), D is the diameter in m, the 3600 (units of second/hour) is a scaling factor to convert the units of rain rate from kg m^{-2} s^{-1} to mm hr^{-1}, and $v_f(D)$ is the terminal fall velocity (units of m s^{-1}) of droplets in the range from *D* to *D+dD,* and $n(D)$ is the drop size distribution (units of m^{-3} mm^{-1}). We use the terminal fall velocity model of Beard (1976) for $v_f(D)$ term. D_{min} is the lower limit for the integration, and except where stated otherwise is set to 40 μm. In Section 2.4.1, we test the importance of smaller droplets with diameter smaller than 40 μm on the total liquid water flux (LWF_{total}).

Similarly, precipitation number (N_{precip}) is calculated as:

$$N_{precip} = \int_{D_{min}}^{\infty} n(D) dD \tag{2.2}$$

Precipitation liquid water content (LWC_{precip}) is calculated as:

$$LWC_{precip} = \frac{\pi}{6}\rho_w \int_{D_{min}}^{\infty} n(D)\, D^3 dD \tag{2.3}$$

Precipitation liquid water content weighted mean diameter (D_{precip}), which can be thought of as diameter at which half of LWC_{precip} is below and half is above, is calculated as:

$$D_{precip} = \frac{\int_{D_{min}}^{\infty} n(D)\, D^4 dD}{\int_{D_{min}}^{\infty} n(D)\, D^3 dD} \quad (2.4)$$

Precipitation liquid water content weighted width (σ_{precip}) is calculated as:

$$\sigma_{precip} = \sqrt{\frac{\int_{D_{min}}^{\infty} n(D)\, D^3 (D - D_{precip})^2 dD}{\int_{D_{min}}^{\infty} n(D)\, D^3 dD}} \quad (2.5)$$

2.2.2.3 Z-R relationships

To estimate the Z-R relationships from in situ measurements, we calculated radar reflectivity Z and rain rate R, respectively from the in situ droplet size distributions (DSD). Rain rate is calculated as equation 2.1. Reflectivity is proportional to the sixth moment of the DSD:

$$Z = \int_{D_{min}}^{\infty} n(D)\, D^6\, \gamma_f(D) dD \quad (2.6)$$

where $n(D)\, dD$ gives number concentrations from diameter D to $D+dD$, $\gamma_f(D)$ is the Mie-to-Rayleigh backscatter ratio (shown in Figure A3, which is the ratio of the backscatter efficiency of Mie scattering for W-band (94-GHz), calculated here using the miepython package (Prahl, 2023) based on Wiscombe (1979), and backscatter efficiency of Rayleigh scattering (Bohren & Huffman, 1983). With calculated reflectivity and rain rate from the in situ DSD, the Z-R relationship assumes a traditional power-law of the form:

$$Z = aR^b \quad (2.7)$$

Where a and b are coefficients, and Z is the independent variable. Equation 2.7 can also be rearranged as $R = (Z/a)^{1/b}$, which can be used to derive R based on Z observations. Coefficients a and b can be estimated using the least-squares regression in log space following Comstock et al. (2004):

$$logR = \frac{1}{b}\,(-\,log\ a\ +\ log\ Z) \quad (2.8)$$

Note that in Section 2.4.1, we also estimated Z-R relationship based on radar observed reflectivity factor and rain rate from a radar-lidar retrieval (more details in section 2.3.3). We use a moving blocks bootstrapping method following Wilks (1997) to estimate the uncertainty in a and b coefficients, with a block length that is close to the e-folding length.

2.2.3 Precipitation Retrievals based on remote sensors

Precipitation retrievals described in this section use the zenith-pointing data collected when the aircraft was flying level-legs below the cloud. To illustrate, Figure 2.2a shows the flight track altitude and measured radar reflectivity for research flight 13 (RF13). In panel (a), the potions of the flight track which feature below-cloud-level legs are colored blue. Figure 2.2b-f shows the radar and lidar data in more detail, for the below-cloud level leg starting from 03:40 UTC, which is marked by the grey shading in Figure 2.2a. In general, retrievals undertaken for below-cloud level legs have the advantage that the zenith pointing lidar data allows one to determine the position of cloud base, as well as providing measurements of the backscatter (Figure 2.2c) and depolarization ratio (Figure 2.2d) of the precipitation that has fallen from the cloud and can be used to determine the precipitation phase. We describe the retrieval process in the three subsections that follow: (1) determine the cloud boundaries; (2) determine the phase of precipitation; (3) determine the liquid precipitation microphysical properties (such as the rain rate).

2.2.3.1 Determine the cloud boundaries

To determine the cloud base, we use the lidar backscatter coefficient β (e.g. Figure 2.2c) and define the cloud base as the altitude where β first exceeds a threshold of 0.0001 m^{-1} sr^{-1}. The black dots in Figure 2.2c show the cloud base identified using this threshold. Cloud top for our analysis is based on the radar reflectivity data, which have already been masked for significant detections (above the instrument noise floor). The cloud top is taken simply as the maximum height with a valid reflectivity echo (i.e. above the instrument noise floor) below 3km, as marked by grey dots in Figure 2.2b-f.

2.2.3.2 Determine the phase of precipitation below cloud base

With the cloud boundaries identified, the next step is to determine the phase of the precipitation falling from the clouds. Following Mace and Protat (2018), we determine the precipitation phase using the lidar particle linear depolarization ratio (PLDR) (e.g., Figure 2.2d). The basic concept is that the lidar emits linearly polarized light, and scattering by spherical particles (e.g. liquid drops) does not change the polarization state of the light and thus generates little PLDR, while scattering from non-spherical particles (e.g. ice particles) creates significant depolarization and thus generates measurable increase in PLDR. In this study, for each lidar column, we examined the median of the PLDR over the vertical interval between cloud base to the first useable lidar range gate. For clouds with a cloud top temperature greater than 0°C, that is for warm clouds whose precipitation must be liquid, we find the below-cloud base PLDR values to be less than 0.03 about 90% of the time, and to be above 0.05 less than 1% of the time(see Appendix Figure A4 for overall statistics and Figure A5 for an example case). Thus, for cooler cold-topped clouds (which might precipitate ice), we define the precipitation to be liquid phase when the median PLDR < 0.03; ice precipitation when PLDR > 0.05; and ambiguous phase with PLDR values in between. The thresholds we use are broadly similar to Tansey et al. (2023) and Mace and Protat (2018). In Tansey et al. (2023), the liquid phase is defined with a depolarization ratio less than 0.05, and the ice phase with a value greater than 0.1. Mace and Protat (2018) defined the liquid phase with a depolarization ratio less than 0.02, and the ice phase with a value greater than 0.03. These thresholds differ somewhat because of differences in the field-of-view of the lidars used in

each study, but they also represent different subjective choices for the degree of confidence desired. Our thresholds allow for little chance of a false detection of ice (nominally < 1%), but consequently, some unknown fraction of ice will be identified as ambiguous. Somewhat similarly, we can expect that 10% of the cases identified as ambiguous are likely to be liquid phase. Consequently, ambiguous phase does not necessitate mixed phase (meaning both liquid and ice are present), though as we will see later, the occurrence of ambiguous phase is significantly larger than the expected 10% of failed-detection for liquid phase clouds and it is likely that many of the ambiguous cases do contain some ice phase precipitation.

We restrict our focus to the precipitation phase below-cloud, because the lidar signal becomes quickly attenuated in-cloud, and equally problematic, the depolarization ratio increases substantially in-cloud because of multiple scattering. A characterization of the phase at cloud base that accounts for multiple scattering is possible (e.g. Mace et al. 2020), as indeed is estimating vertical phase profiles using a combination of radar and lidar (e.g. Schima et al. 2022), albeit with larger inherent uncertainties.

2.2.3.3 Liquid Precipitation Retrieval

After determining the cloud base and precipitation phase, we can use a hierarchy of retrieval methods with increasing complexity to derive the precipitation properties, starting from (1) a simple Z-R relationship approach where only one variable, the radar reflectivity, Z, is available to derive the rain rate, to (2) a ZV retrieval following Mace et al. (2002) and Marchand et al. (2007), where radar reflectivity, Z, and mean Doppler velocity, V, are known, to (3) a radar-lidar retrieval following O'Connor et al. (2005) based on three observables: radar reflectivity Z, radar Doppler spectral width σ_d, and lidar backscatter β. We briefly describe the radar-lidar and the ZV retrieval in this section, and present retrieval results and evaluate the retrievals using in situ observations in Section 2.4.

The radar-lidar retrieval technique uses three input variables radar reflectivity, Z (Figure 2.2b), doppler spectral width, σ_d (Figure 2.2e), and lidar backscatter, β (Figure 2.2c), to solve for three parameters in an assumed modified gamma distribution (equation 2.9) for the precipitation drop size distribution (Ulbrich, 1983; Illingworth and Blackman, 2002; Petty and Huang, 2011). The three parameters are the shape factor μ, the median equivolumetric diameter D_0, and the normalized droplet concentration N_w:

$$n(D) = N_w f(\mu)\left(\frac{D}{D_0}\right)^{\mu} e^{\left[\frac{-(3.67+\mu)D}{D_0}\right]} \tag{2.9}$$

where D is diameter, and $f(\mu)$ is a function of μ

$$f(\mu) = \frac{6}{3.67^4}\frac{(3.67+\mu)^4}{\Gamma(\mu+4)} \tag{2.10}$$

where Γ is the gamma function. Integration of the droplet size distribution in (9) will yield the precipitation droplet number concentration, N_{precip}, as in equation 2.2.

Following O'Connor et al. (2005), one can show that for a fixed value of the shape factor, μ, the ratio of the radar reflectivity to lidar backscatter is proportional to the fourth power of the mean

drop size, and the combination of radar reflectivity and lidar backscatter can therefore be used to calculate D_0 and N_w. In the retrieval algorithm, this is done assuming an initial value of $\mu = 0$. The Doppler spectral width is then forward calculated and μ is increased or decreased in order to match the observed Doppler spectral width (after applying turbulence corrections as described below). In the retrieval algorithm, we restrict μ to range from -1 to 10 following O'Connor et al. (2005). The algorithm adjusts μ and recomputes D_0 until convergence (with more details given in O'Connor et al., 2005). The forward calculations require a model for the hydrometeor terminal fall velocity, for which we use the model of Beard (1976). Once the three distribution parameters are known, it is straightforward to calculate the rain rate, rain liquid water content, and mean rain drop size, etc. using the fall velocity and equation 2.9. This retrieval technique has been widely used in retrieving drizzle properties (e.g. Ghate & Cadeddu, 2019; Yang et al., 2018), including the CSET campaign with airborne radar and lidar (Schwartz et al., 2019; Sarkar et al., 2021). Our implementation largely follows O'Connor et al. (2005), except for the estimation of the contribution from air turbulence to the observed spectral width. Instead of using the horizontal wind speed to estimate the length scale, we use the aircraft speed (we note O'Connor et al. (2005) originally developed the retrieval for vertically pointing ground-based radar and lidar). Note that spectral broadening caused by aircraft motion was already corrected in the HCR data provided by NCAR/EOL, as described in Romatschke et al. (2021).

In addition to the radar-lidar retrieval technique, we also use a reflectivity-velocity (ZV) retrieval technique (Frisch et al.,1995; Mace et al., 2002; Marchand et al.,2007). The first step in this retrieval is to estimate the precipitation fall velocity from radar measured Doppler velocity, which includes the effect of vertical air motions (i.e., updrafts/downdrafts). We do this following Orr and Kropfli (1999) and partition the measured Doppler velocities into a set of height and reflectivity bins (for each below-cloud zenith-pointing segment) and average the partitioned Doppler velocity as an estimate for the fall velocity (as a function of height and radar reflectivity). The underlying idea is that at a given altitude and reflectivity, there is a characteristic size distribution (with a characteristic fall velocity) and by averaging the Doppler velocities over a narrow range of reflectivity values, one averages out the effect of the updrafts and downdrafts leaving only the mean precipitation fall velocity. In this study we use reflectivity bins are that 2 dBZ wide, and use 200 m vertical bins with 100 m overlap. The results are not particularly sensitive to these choices, as long as there is a healthy number of samples available in each bin (at least 10 samples). Following Frisch et al. (1995), it is straightforward to obtain analytical expressions for distribution parameters D_0 and N_w given the derived fall velocity, measured reflectivity, and an assumed shape factor μ. Except where we state otherwise, we assume the shape factor to be 0. One can show that the modified gamma distribution (equation 2.9) reduces to the exponential distribution when the shape factor is zero. In the radar-lidar retrieval, we find the retrieved shape factor is often quite small and we will examine and discuss the sensitivity of the ZV retrieval to assumed shape factor values in Section 2.4.2.

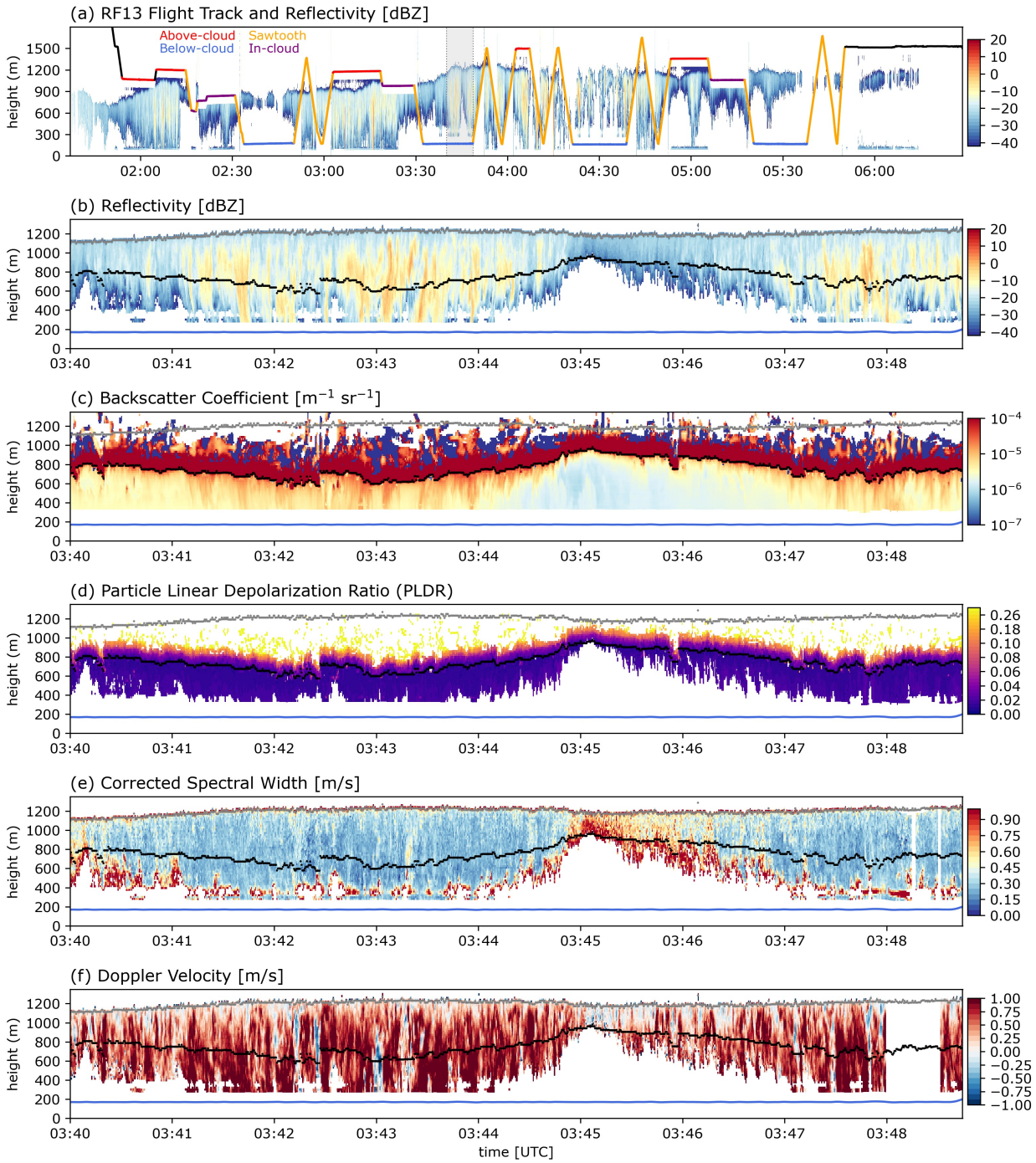

Figure 2.2 Example radar and lidar data collected during the SOCRATES. Panel a shows the flight tracks and reflectivity fields from research flight 13 (RF13), with different segments color-coded as in Figure 2.1. The grey shading in panel a marks a portion of one below-cloud level leg, and a zoom-in view of the radar and lidar fields for this segment are shown in panels b-f: (b) radar reflectivity; (c) lidar backscatter coefficient; (d) lidar particle linear depolarization ratio; (e) radar spectral width; (f) radar doppler velocity. The grey lines show the estimated cloud top,

the black lines show the estimated cloud base, and the blue lines show the location of the aircraft for below-cloud level legs.

2.3 Campaign overview and phase partitioning

To get a general sense of the hydrometers (clouds and precipitation) sampled by the airborne W-band radar during the SOCRATES, Figure 2.3a shows the joint histogram of radar reflectivity with height observed during below-cloud, zenith-pointing periods. Here the histogram is normalized by the number of radar columns, such that the value in each bin indicates how often hydrometers have a reflectivity (with +/– 1 dBZ of the given value) in the given altitude/height range; and the sum at each height (row) will give the hydrometer fraction (Figure 2.3b).

Note that there are no data to the left of the red line in panel a. This is because of the limited radar sensitivity, and as distance increases, the minimum detectable reflectivity factor increases. Likewise, there are no data from 0 to 200 meters altitude because the aircraft's lowest legs were typically flown at around 100-150 m altitude, and the radar blanking interrupt (the region corresponding to the time when the radar outgoing pulse is being, or has just been, transmitted and the radar system has not yet begun measuring the return power) typically extends about 203 m above this (Schwartz et al., 2019).

The maximum frequency of hydrometers observed by the radar occurred between 700m and 1200m, with a hydrometer fraction over 50%. (Note this is not the projected area or the fraction of radar columns with a significant echo at any altitude, that value is near 90%). Reflectivity factors larger than –10 dBZ are relatively rare and the peak or most likely reflectivity factor is between −30 to –20 dBZ. Reflectivity factors larger than -10 dBZ are common over the Southern Ocean (see for example Mace and Protat 2018), but such factors are associated with fronts or convection (including the shallow convection sometimes associated with vigorous open cells) and not typical of the shallow (cloud tops < 2 km) and largely overcast stratocumulus sampled during SOCRATES. Rather there is a single mode or continuum of reflectivity that spans reflectivity factors from about –40 dBZ (where rain rate is very light on the order of 10^{-4} mm hr^{-1}) to values around –10 dBZ (where precipitation is still light but with a rain rate near 1 mm hr^{-1}), and a peak below –20 dBZ. We stress that rain rates near 1 mm hr^{-1} are light but have a substantial impact on cloud condensation nuclei and cloud lifetime (Chapter 3). Most of this stratocumulus is supercooled. Overall, we find that about 80% of the stratocumulus sampled during SOCRATES had a cloud top temperature < 0°C and cloud depth < 600m (figure not shown), and about 62% of the stratocumulus were precipitating, defined as having 3 consecutive radar bins (about 60 meters) below cloud base with a reflectivity greater than –40dBZ. This occurrence of precipitation drops to 34% if a reflectivity threshold of –20 dBZ is applied (rather than –40 dBZ), indicative of the very light nature of much of the precipitation.

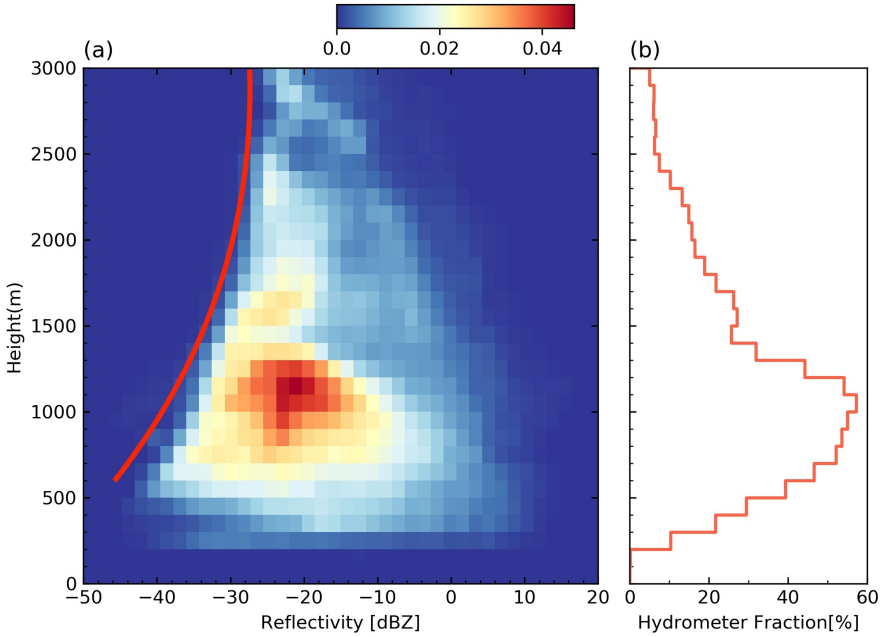

Figure 2.3. (a) Joint histogram of the hydrometer (cloud & precipitation) radar reflectivity with height observed by the airborne W-band radar during below-cloud, zenith-pointing periods (i.e., when aircraft is flying below the cloud, as illustrated in Figure 2.1). The histogram is normalized by the total number of radar "columns" such that the histogram values are the fractional occurrence (see text). (b) hydrometer fraction [%] at each height of all radar "columns". The red line on panel a illustrates the minimum detectable reflectivity values by HCR as a function of height.

What is the phase of the precipitation sampled during the SOCRATES? As described in Section 2.2.3.2, we determine the precipitation phase using the lidar particle linear depolarization ratio PLDR (Figure 2.2d), and interpret the precipitation as liquid phase when PLDR < 0.03; ice phase when PLDR > 0.05; and ambiguous for PLDR values in between. Figure 2.4a shows that around 60% of the precipitation from the zenith-pointing segments are liquid phase and about 20% of the precipitation are ice phase, with the remaining 20% being ambiguous phase. How does precipitation phase relate to the cloud top temperature? Figure 2.4b shows the relative occurrence of precipitation in different phases as a function of cloud top temperature (CTT). For the warm-topped clouds (CTT > 0°C), we expect that all the precipitation should be liquid phase. Temperature is not used in the phase retrieval, and consistent with the discussion in Section 2.2.3.2, the low occurrence of ambiguous or ice phase precipitation with CTT > 0°C is indicative of the low retrieval error. For the cold-topped clouds (CTT <0°C), liquid precipitation still dominates for clouds with CTT between 0 and -10°C, with the ice fraction increasing as temperature decreases. But it is not until about a CTT of -15°C that ice phase appears to dominate.

An interesting question related to phase is whether or not precipitation phase is related to radar reflectivity. Zhang et al. (2017) have shown that lidar depolarization ratios are correlated with radar reflectivity, and for the SO in particular, Mace and Protat (2018) show that W-band radar reflectivity greater than –10 dBZ is associated with ice-phase hydrometeors (based on

CAPRICORN observations). Figure 2.4c shows the occurrence of the different precipitation phases for cold-topped clouds as a function of reflectivity. Overall, it shows that reflectivity factors less than about –10 dBZ are predominantly liquid, while reflectivity factors greater than 0 dBZ are predominantly ice. We will discuss this result in more detail in the conclusions.

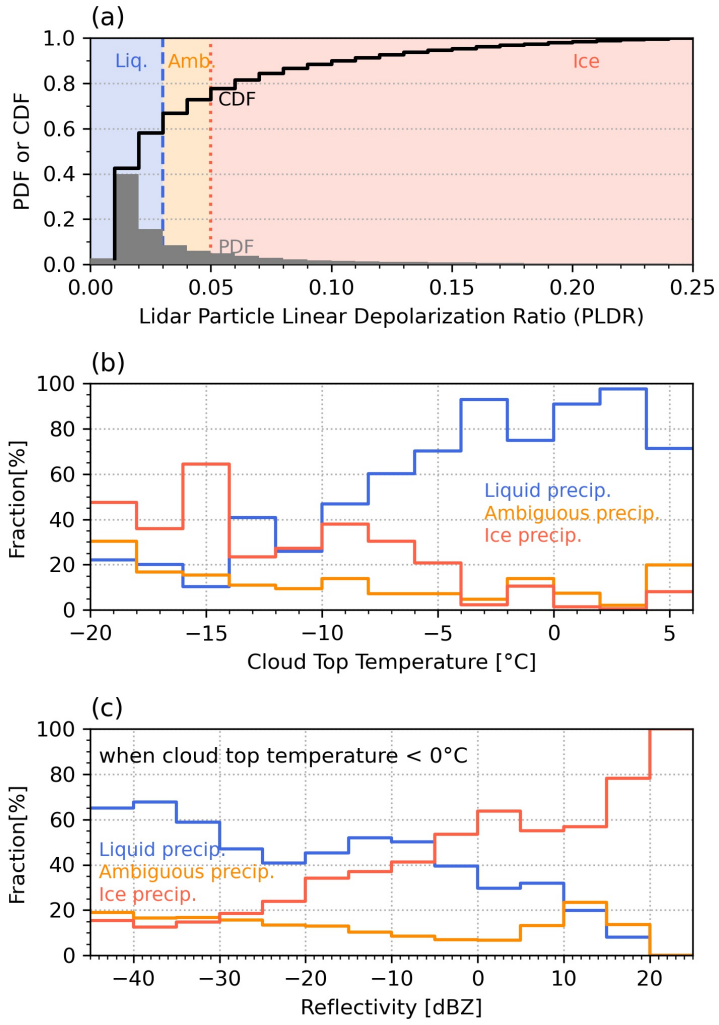

Figure 2.4 (a) Probability and cumulative density functions for lidar particle linear depolarization ratio (PLDR) for below-cloud precipitation, (b) The fraction of liquid, ice, and ambiguous precipitation as a function of cloud top temperature, (c) The fraction of liquid, ice, and ambiguous precipitation as a function of radar reflectivity. To distinguish different precipitation types, liquid precipitation is marked as blue, ice precipitation is marked as red, and ambiguous precipitation is marked as orange.

2.4 Liquid Precipitation Retrievals

In this section, we will explore a hierarchy of retrieval methods based on complexity, from (1) the simplest Z-R relationship approach where only one variable reflectivity Z is known, to (2) a ZV retrieval using two variables (reflectivity Z and Doppler velocity V), to (3) a radar-lidar retrieval based on three variables (reflectivity radar reflectivity Z, doppler spectral width σ_d, and

lidar backscatter β). In section 2.4.1, we will develop Z-R relationships based on in situ data. In section 2.4.2, we will demonstrate the results from ZV and radar-lidar liquid precipitation retrievals using a case example, and in section 2.4.3, we evaluate these retrievals using in-situ aircraft observations from all the segments where retrievals were performed.

2.4.1 Reflectivity to rain rate (Z-R) relationships

One objective of this study is to estimate Z-R relationships of the form $\mathrm{Z} = \mathrm{a}R^b$. Z-R relationships are useful and convenient, requiring only one independent variable (reflectivity Z) to estimate rain rate R. Such relationships have a long history in atmospheric science, and as concerns stratocumulus in particular, relationships have been derived in past studies for stratocumulus over the Eastern Pacific (Comstock et al., 2004), over the north-east Atlantic and in U.K. coastal waters (Wood, 2005), and for nocturnal stratocumulus clouds off the California Coast (VanZanten et al., 2005). More recently, Protat et al. (2019b) estimated Z-R relationships at the surface over the global ocean, including the Southern Ocean, based on surface disdrometer measurements. In this section, we will derive Z-R relationships using SOCRATES aircraft observations following the method presented in Section 2.2.2.3 and compare our results with previous studies.

Figure 2.5 shows the Z-R relationships derived using in situ data taken at different locations relative to the cloud layer and surface (see Figure 2.1 for a schematic). Table 2.2 lists the corresponding a and b coefficients. In Figure 2.5a, we only consider droplets with a diameter larger than 40 μm following Comstock et al. (2004), while in Figure 2.5b, we include all droplets including those droplets with a diameter smaller than 40 μm. We will focus on Figure 2.5a first. Figure 2.5a shows that estimated Z-R relationships do have a vertical dependence. The intercept controlled by coefficient a increases as one moves from the cloud layer to the surface, while the slope controlled by exponent b remains largely unchanged. The vertical dependence of Z-R was also noticed in previous studies (e.g. Comstock et al., 2004; vanZanten et al., 2005). The exponent b estimated in Figure 2.5a ranges from 1.19 to 1.41, with a one-sigma uncertainty that ranges from 0.04 to about 0.07, based on a bootstrap resampling technique (uncertainties are listed in Table 2.2). Note the uncertainties in the a and b coefficients are not independent, but rather are positively correlated such that a larger estimate for the a-value is associated with a larger estimate for the b-values. It is worth also noting that uncertainty estimated by the bootstrapping does not account for the uncertainty in the measurements (section 2.2.2.1). It only accounts for the uncertainty in the relationship given the finite sample size. As described in section 2.2.2.1, this analysis includes only periods identified as liquid phase using the D'Alessandro phase product. Relaxing this restriction has no significant effect on the below-cloud values, but does result in a slight increase in the b coefficient by 0.1 to 0.2 and a decrease in the a coefficient by about 50% for the in-cloud relationships (given in the top three rows). Table 2.2 also lists some Z-R relationships estimated from other studies mentioned above. Overall, we find the exponent b to be similar to that from Comstock et al. (2004), vanZanten et al. (2005), and many other earlier studies summarized in Rosenfeld and Ulbrich (2003) over other regions and other cloud types. Later in this section, we will compare the rain rate derived from Z-R relationships with rain rate derived from two other retrieval methods.

The above analysis is based on the idea that only droplets larger than 40 μm are considered precipitation. But droplets smaller than 40 μm can and do contribute to the flux of liquid water (Nicholls, 1984). What happens if small droplets with a diameter smaller than 40 μm are included when calculating Z and R from in situ DSDs? The results are shown in Figure 2.5b. Comparing Figure 2.5a and 2.5b, one can see that the estimated Z-R relationships are very sensitive to whether one excludes smaller drops, especially for the data collected in the cloud. Differences in the estimated Z-R are less dramatic when using in situ data outside of the cloud (i.e. below-cloud portion of the sawtooth leg and below-cloud level legs).

To explore the importance of the smaller droplets, Figure 2.6a shows an example of DSDs measured near the top of a cloud, near the bottom of the cloud, and below cloud during one sawtooth leg, as well as a nearby below-cloud level leg (depicted in the bottom panel). The associated liquid water flux distribution $D^3N(D)V(D)$ is shown in Figure 2.6b, and the reflectivity distribution $D^6N(D)$ in Figure 2.6c. Note as in the microphysical retrievals, here we use the terminal fall velocity model of Beard (1976) for V(D). Below cloud, small droplets evaporate much more quickly than larger droplets, and most of the contributions to the liquid water flux comes from larger droplets, such that the effect of small droplets on liquid water flux and reflectivity can be largely neglected. We hasten to add, however, this is not true for the total number concentration (Figure 2.6a); where small droplets remain more numerous (than droplets above 40 μm), and include many particles with sizes smaller than 5 μm, which one might consider haze-particles or hydrated-aerosols rather than cloud droplets. Within the cloud layer, small droplets make a large contribution to the liquid water flux, though they still only contribute slightly to the reflectivity. Droplets in the diameter range of 10-40 μm contribute 78% of the liquid water flux in the top half of the cloud, and still comprise about half of the water flux in the bottom half of the cloud. Contributions to the reflectivity from droplets in the range of 10-40 μm are smaller than those of larger droplets, but do make a non-trivial contribution.

In short, as Figure 2.6 and the differences in estimated Z-R in Figure 2.5a and Figure 2.5b highlight, the sedimentation of small droplets is (or can be) a significant component of the total liquid water flux in cloud and applying the Z-R relationship derived from only larger particles or from below-cloud measurements effectively ignores the contribution from small particles (and below-cloud Z-R equations should be applied with caution to in-cloud reflectivity measurements and should be expected to underestimate the total liquid water flux).

It is perhaps worth noting that even below cloud, the DSD is not a simple gamma function, as assumed in the radar ZV or radar-lidar retrievals. However, as is the case in Figure 2.6, there is often a clear mode associated with drops larger than 40 μm below-cloud and generally the liquid water flux and radar reflectivity (as well as the radar Doppler velocity and lidar backscatter–- not shown) are controlled by these precipitation-sized drops and the gamma distribution assumption does not cause a major problem. In effect, below cloud, the gamma function only needs to represent the larger droplets. For the radar-lidar retrieval, however, this assumption is a major problem in cloud or even close to cloud base, where the lidar backscatter is substantially impacted by the cloud droplets – and ultimately, this is why we only apply the radar-lidar retrieval below cloud.

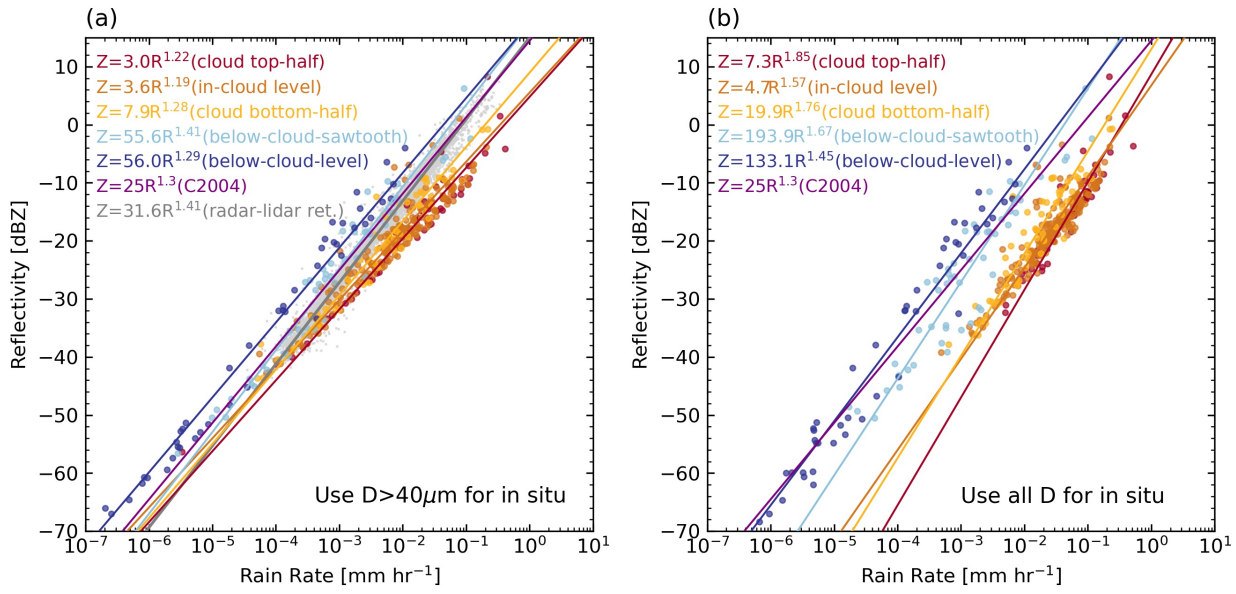

Figure 2.5 Z-R relationship derived using in situ data and retrievals. Diameter >40um cutoff for the in situ measurements is imposed in panel a, while panel b does not apply any cutoff, and considers all droplet sizes for in situ data.

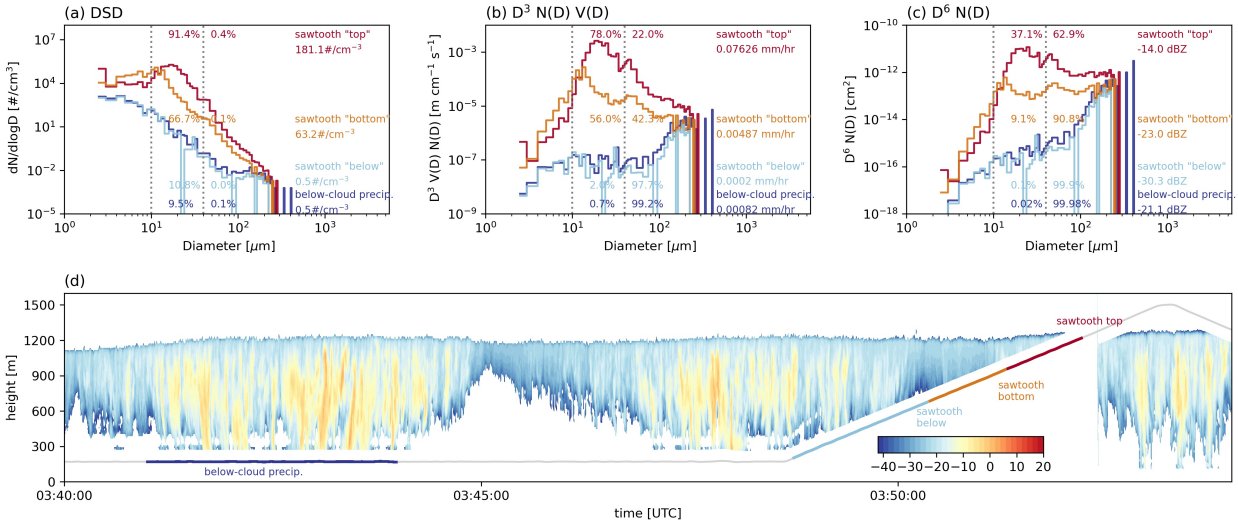

Figure 2.6 Example case to show the contributions of droplets in different size ranges with in situ measurements taken from different segments: (a) average droplet size distribution; (b) product of diameter cubed, droplet size distribution and terminal fall velocity;(c) product of diameter to the power of six and droplet size distribution; (d) reflectivity field and flight track for this example, the color-coded lines marked the locations of different segments showing in panel a-c. The vertical dashed line in panels a-c is the reference line for 10 μm and 40 μm. The percentages on panels a, b, and c show the contributions from different size ranges to droplet number concentration, to rain rate, and to reflectivity, respectively.

Table 2.2 Z-R relationships

Equation	Location	Remarks	Reference
$Z = (3.0 \pm 1.3)\, R^{(1.22 \pm 0.07)}$ [$Z = (7.3 \pm 6.7)\, R^{(1.85 \pm 0.19)}$]	the top half of the cloud layer from the sawtooth leg	Estimated using SOCRATES aircraft in situ measurements with and without the 40 μ m cutoff [without given in brackets]	This study
$Z = (3.6 \pm 0.9)\, R^{(1.19 \pm 0.04)}$ [$Z = (4.7 \pm 1.7)\, R^{(1.57 \pm 0.08)}$]	in-cloud level legs		
$Z = (7.9 \pm 2.3)\, R^{(1.28 \pm 0.04)}$ [$Z = (19.9 \pm 11.6)\, R^{(1.76 \pm 0.09)}$]	bottom half of the cloud layer from the sawtooth leg		
$Z = (55.6 \pm 24.6)\, R^{(1.41 \pm 0.05)}$ [$Z = (193.9 \pm 183.0)\, R^{(1.67 \pm 0.09)}$]	the below-cloud portion of the sawtooth leg		
$Z = (56.0 \pm 45.1)\, R^{(1.29 \pm 0.05)}$ [$Z = (133.1 \pm 250.0)\, R^{(1.45 \pm 0.1)}$]	below-cloud level legs.		
$Z = (31.6 \pm 1.4)\, R^{(1.41 \pm 0.007)}$	Cloud base	Estimated using SOCRATES W-band radar measured reflectivity and radar-lidar retrieved rain rate just below cloud base	
$Z = 25R^{1.3}$	Cloud base	Estimated for stratocumulus over Eastern Pacific	Comstock et al. (2004)
$Z = 12.92\, R^{1.47}$	Cloud base	Estimated using aircraft in situ DSD measurements for nocturnal stratocumulus clouds over California Coast	vanZanten et al. (2005)
$Z = 12.5\, R^{1.18}$	All in-cloud levels	Estimated using aircraft in situ DSD measurements for stratocumulus over the north-east Atlantic and in U.K. coastal waters	Wood (2005)

Note: here uncertainty is estimated using either bootstrapping (rows 1-5) or moving block bootstrapping (row 6) with the one-sigma uncertainty given after the plus-minus sign. For the Z-R relationship that is estimated using in situ measurements, the Z-R relationship estimated using only larger droplets, with a diameter greater than 40 μ m, is listed first, followed by the Z-R relationship estimated using all droplets included those droplets with a diameter smaller than 40 μ m. For the equations above, the reflectivity Z is in the unit of $mm^6 mm^{-3}$, and the rain rate is in the unit of mm hr^{-1}. For the equations in the past studies with the form of $R = cZ^d$ or have different units, we rearranged the equation and converted the units to keep the consistency and make it easier to compare. Unless noted, the default band for reflectivity is W-band.

2.4.2 ZV retrieval and radar-lidar retrieval

In this subsection, we examine both the ZV retrieval and radar-lidar retrieval using the zenith-pointing remote sensing data collected when the aircraft was flying level-legs below the cloud. We will begin with one case study, compare results from different retrieval methods, and then examine the sensitivity of ZV retrieval results to the assumed shape factor μ. The overall retrieval performance will be evaluated in Section 2.4.3.

Applying the ZV retrieval (described in Section 2.2.3.3) to the example presented in Figure 2.2, the parameters D_0 and N_{precip} can be derived from measured reflectivity Z, assumed shape factor μ, and derived terminal fall velocity. Figure 2.7a shows the reflectivity-weighted terminal fall velocity, v_t, derived following Orr and Kropfli (1999). Here we see generally larger v_t toward the bottom of the cloud, and in precipitation shafts (regions of relatively high reflectivity extending below cloud base). Figure 2.7b and 2.7c show the derived median equivolumetric diameter D_0, and precipitation concentration N_{precip}, assuming μ =0. Not surprisingly, Figure 2.7b shows that D_0 is larger where v_t is larger, and is about 100-200 μm below cloud base. Figure 2.7c shows N_{precip} below cloud base is in the order of 10^3~10^5 m^{-3}.

Applying the radar-lidar retrieval technique to the example presented in Figure 2.2, with three input variables (radar reflectivity Z, doppler spectral with σ_d, and backscatter coefficient β), we can also solve for shape factor μ, median equivolumetric diameter D_0, and precipitation number concentration N_{precip}, as shown in Figure 2.8. The shape factor μ describes the shape of the DSD (equation 2.9), where a larger μ implies a narrower distribution. As in O'Connor et al. (2005), we find large areas with broad DSDs (small μ). Narrow DSDs implied by large μ are typically found underneath the thicker portion of the clouds (and as we will see later have larger rain rates). The median equivolumetric diameter D_0 is mostly between 50-250 μm, with larger sizes occurring where μ is larger. Again, this is similar to what O'Connor et al. (2005) observed and appears to be quite typical for drizzling stratocumulus. Comparing the two retrieval methods, D_0 from ZV retrieval (Figure 2.7) tends to be more spatially homogeneous below cloud base than that from radar-lidar retrieval (Figure 2.8), and the D_0 from ZV retrieval tends to be smaller than that from radar-lidar retrieval in the precipitation shafts (where the assumption of a small value for the shape factor appears problematic, more on this below).

Once the parameters that determine the DSDs are derived, it is straightforward to calculate other precipitation properties such as rain rate. Figure 2.9b and c show the ZV retrieved the rain rate (assuming μ =0) and radar-lidar retrieval retrieved the rain rate. Overall, the two retrieval methods give similar results (at cloud base, the mean rain rate from the ZV retrieval is 0.008 mm hr^{-1}, and the mean rain rate from the radar-lidar retrieval is 0.007 mm hr^{-1}). With derived Z-R relationships from section 2.4.1, one can also derive rain rate by applying them to the radar reflectivity fields, as shown in Figure 2.9a, where we have applied three Z-R relationships: the *sawtooth-top* relationship to the top half of the cloud, the *sawtooth-bottom* relationship to the bottom half of the cloud, and the *sawtooth-below* relationship to the area below the cloud base. The discontinuity in the rain rate fields in Figure 2.9a is because three different Z-R relationships are applied to different regions. The difference in Z-R relationships (i.e. with or without D>40 μm cutoff) also results in differences in the derived rain rate (Appendix Figure A6), especially for the in-cloud portion. Overall, regardless of the retrieval approaches, it can also be seen that

higher rain rates tend to occur below the geometrically thicker portion of the clouds, and we will explore the scaling between rain rate and cloud depth further in Section 2.6.

In Figures 2.7 and Figure 2.9b, we assume $\mu = 0$ in the ZV retrieval, while the retrieved μ from radar-lidar retrieval clearly shows spatial variations (Figure 2.8a). How does the ZV-retrieved D_0, N_{precip}, and rain rate vary with assumed μ? Appendix Figure A7 shows that the derived D_0 increases with increasing μ values such that the mean D_0 just below cloud base is 102 μm when $\mu = 0$, and is 156 μm when $\mu = 10$. When using radar-lidar retrieved μ as input for ZV retrieval, the spatial variations in retrieved D_0 (Figure A7f) are similar to radar-lidar retrieved D_0 (Figure 2.8b). In contrast, as shown in Figure A8, the derived N_{precip} decreases significantly with increasing μ values, with mean N_{precip} at cloud base being about 1.3×10^5 m^{-3} when $\mu = 0$, and about 1.2×10^3 m^{-3} when $\mu = 10$. On the other hand, the derived rain rate (Figure A9) shows relatively little dependence on assumed μ, with the rain rate at cloud base decreasing slightly from about 0.008 mm hr^{-1} ($\mu = 0$) to about 0.007 mm hr^{-1} ($\mu = 10$). The small sensitivity in rain rate ultimately arises because the liquid water flux is to first order given by the velocity (which is input to the retrieval) times the liquid water content (which is strongly constrained by the reflectivity that is likewise input to the retrieval).

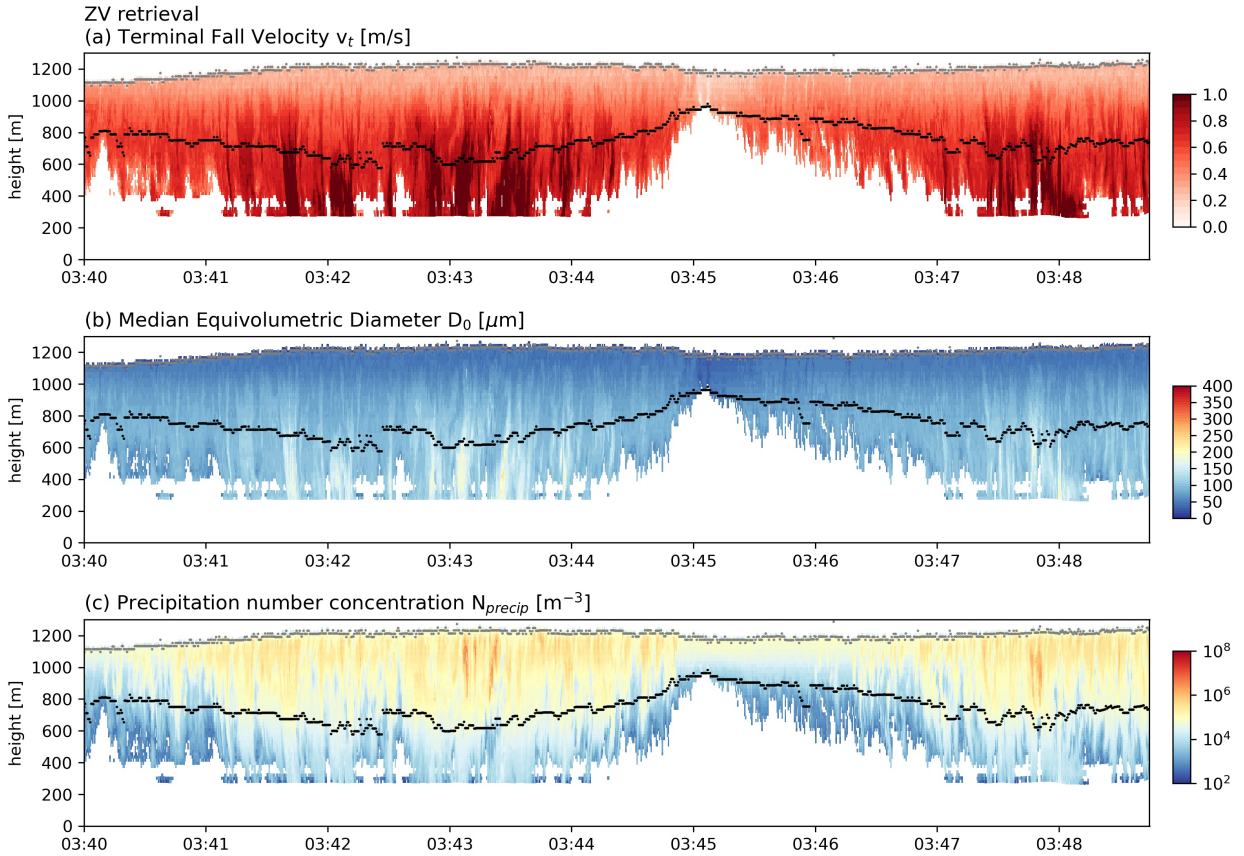

Figure 2.7 A time-height plot of the ZV method retrieved precipitation properties assuming a shape factor of zero for the example segment is shown in Figure 2.2: (a) reflectivity-weighted the terminal fall velocity v_t, (b) median equivolumetric diameter D_0, and (c) precipitation number concentration N_{precip}. The grey lines show the estimated cloud top, the black lines show the estimated cloud base.

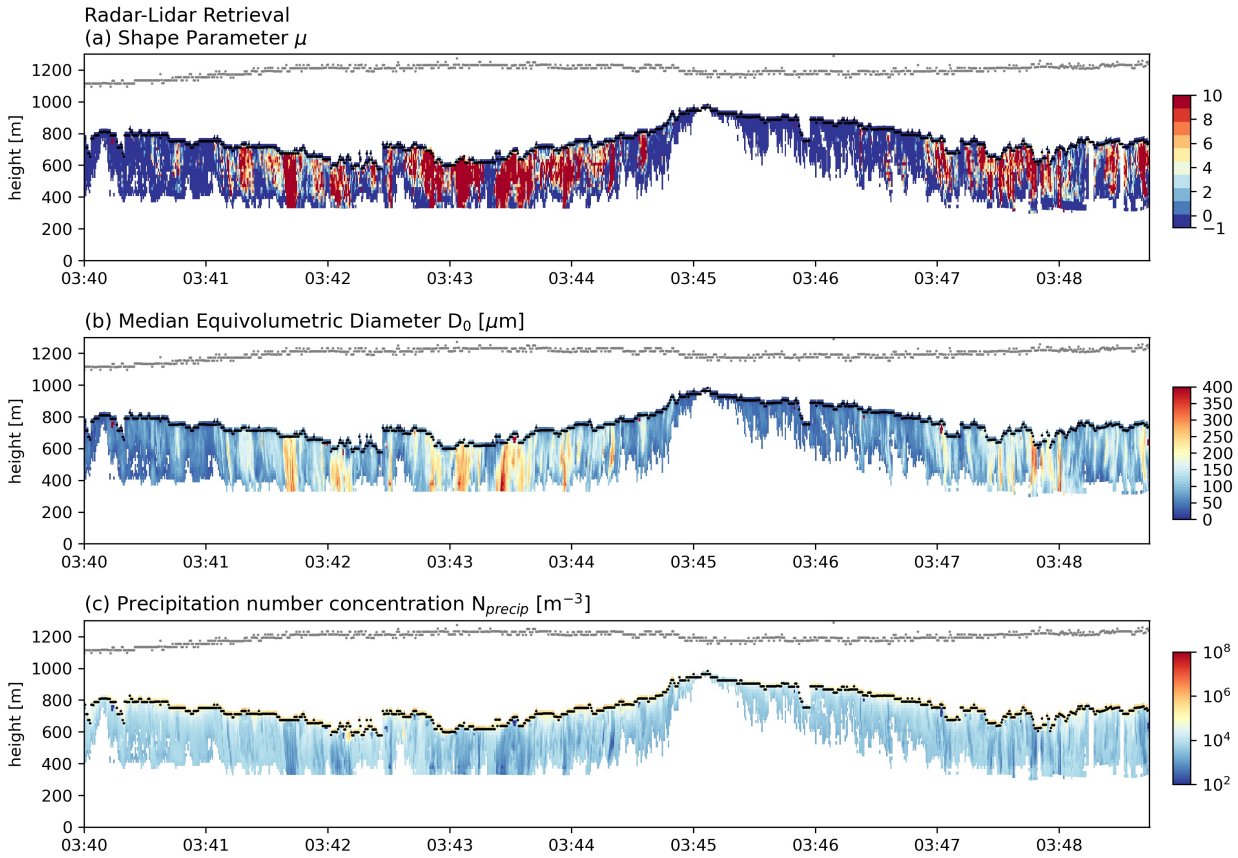

Figure 2.8 A time-height plot of radar-lidar retrieved precipitation properties for the example segment is shown in Figure 2.2. Radar-lidar retrieval method derived parameters for modified gamma distribution: (a) shape factor μ, (b) median equivolumetric diameter D_0, and (c) precipitation number concentration N_{precip}. The grey lines show the estimated cloud top, and the black lines show the estimated cloud base.

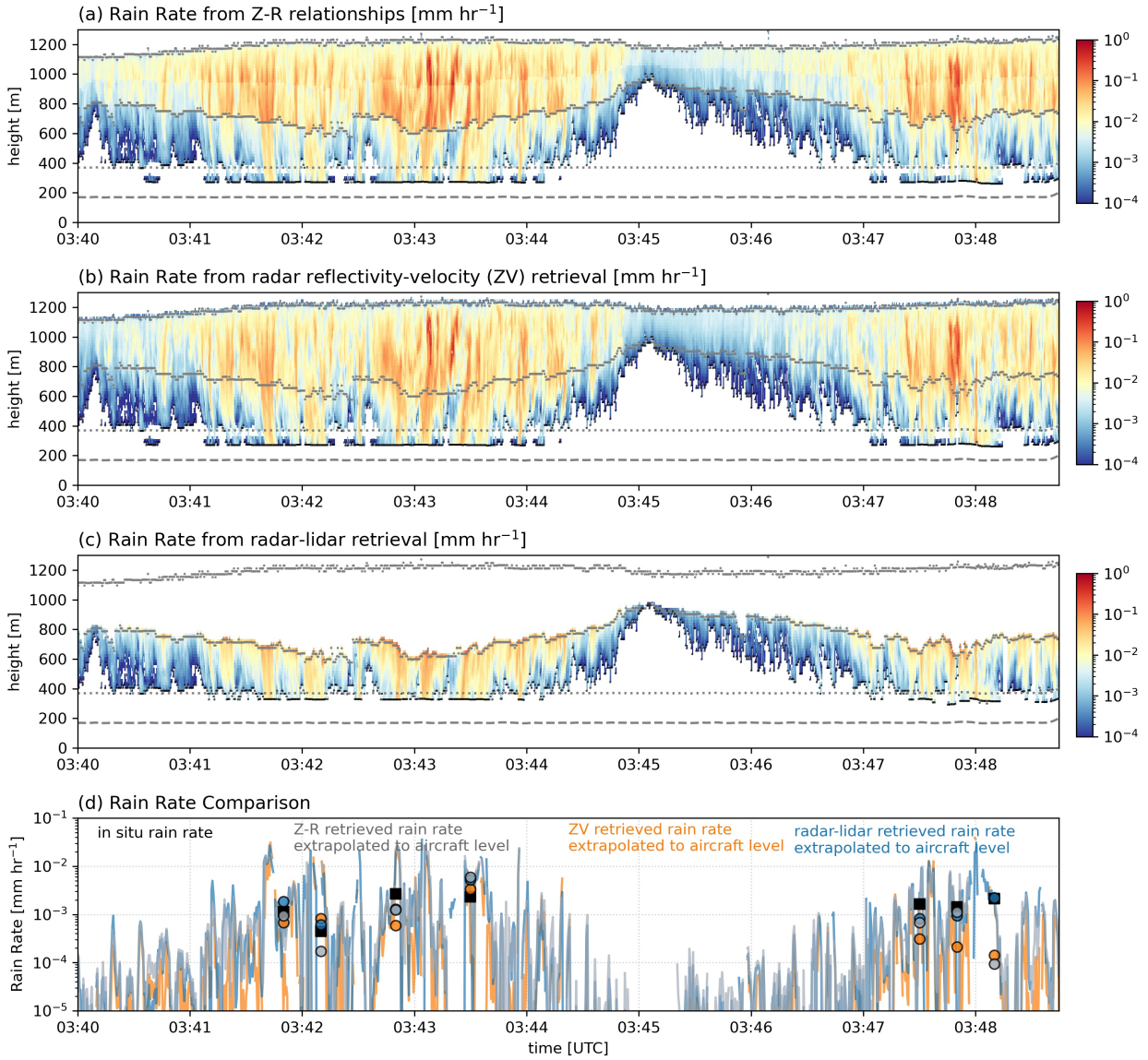

Figure 2.9 Retrieved rain rate for example case using (a) Z-R relationships (D > 40 μm), (b) ZV retrieval technique, (c) radar-lidar retrieval technique, and (d) their comparisons with in situ estimates. In panels a-c, the dashed grey line shows the location of the aircraft, while the dotted line is a reference line to show 200 meters above the aircraft's location. In panel d the retrieved rain rates were extrapolated to the aircraft level to compare with the in situ data. The grey line shows the rain rate retrieved with Z-R relationships, the orange line shows the rain rate retrieved with the ZV retrieval technique, and the blue line shows the rain rate retrieved with the radar-lidar retrieval technique. The black squares represent the rain rate estimated with in situ measurements, where rain rates are derived from averaged droplet size distribution (merged CDP and 2DS) over 20 seconds. Over that same time window, the median value of the retrieved rain rate time series was taken, denoted as grey dots (Z-R relationship), orange dots (ZV retrieval), and blue dots (radar-lidar retrieval).

2.4.3 Retrieval validation

How good are the rain rate retrievals? One would think a simple comparison between the retrieved rain rate with in situ measurements from the aircraft could answer this question. But there are a few challenges that need to be overcome.

The first challenge is that retrieved rain rates that are closest to the aircraft level marked as a dashed line around 200 m in Figure 2.9) are still at least 150 meters away, making it difficult to make a direct comparison. This is because there is a blanking interrupt, a brief period where one needs to wait for the outgoing pulse to exit the radar (or lidar) system and for the effect of strong scattering from nearby objects (clutter) to dissipate. To overcome this difficulty, we extrapolate the retrieved rain rate downwards to the aircraft level by fitting an exponential function to each radar column. The assumption is that the rain rate varies with distance below the cloud base exponentially due to evaporation (Wood, 2005; Comstock et al., 2004). Figure A10 in the supporting information shows an example of rain rate derived from the exponential fit, and demonstrates that the exponentially fitted rain rate shows reasonable agreement with the retrieved rain rate where such is retrieved. Figure 2.9d compares the extrapolated rain rate from the Z-R relationship (grey line), the extrapolated rain rate from ZV retrieval (orange line), and the extrapolated rain rate from radar-lidar retrieval (blue line). To further increase our confidence, we only compare the extrapolated rain rate from those periods where the original retrieved rain rate extends to within 200m of the aircraft (i.e. when the rain extends down to dotted reference line). Another challenge is the limited sampling volume of the in situ probes. To overcome this difficulty, we average the in situ DSD over a 20s period when calculating the rain rate, marked as black squares in Figure 2.9d. We also calculate median of the corresponding retrievals over the same 20s time window, marked by the grey, orange and blue dots. It can be seen that the retrieved rain rate shows reasonable agreement with in situ data for this case.

We repeated this analysis for the liquid-precipitation retrievals for all the SOCRATES flights and summarized the results in Figure 2.10. Overall, the Z-R, ZV, and radar-lidar retrievals compare well with the in situ, with Pearson correlation coefficient of 0.88. 0.88 and 0.89, respectively. Despite the simplicity of the approach, even the rain rate derived from Z-R relationship shows skill in determining the rain rate as compared to the in situ values. The fractional difference in mean rain rate (mean difference in 20s means/average of 20s means) between the Z-R retrieval and in situ data is −12.5%. We can estimate the uncertainty in the retrieved rain rate via error propagation. If we estimated the uncertainty in reflectivity as 1.5 dB for reflectivity (following O'Connor et al., 2005) and 10% for lidar backscatter (e.g., Schwartz et al., 2019), we estimate the uncertainty in the radar-lidar retrieved rain rate would be 18%. Similarly, with an uncertainty of 1.5 dB for reflectivity, and 10% uncertainty for terminal fall velocity (see Tansey et al., 2022), we estimate the uncertainty in the ZV retrieved rain rate to be 44%. As for the Z-R relationship, using the uncertainties below-cloud sawtooth leg relationship from Table 2.2, the estimated uncertainty in rain rate is 42%. Relative to the expected uncertainties due simply to uncertainties in the inputs, all three retrievals compare well with the in situ data.

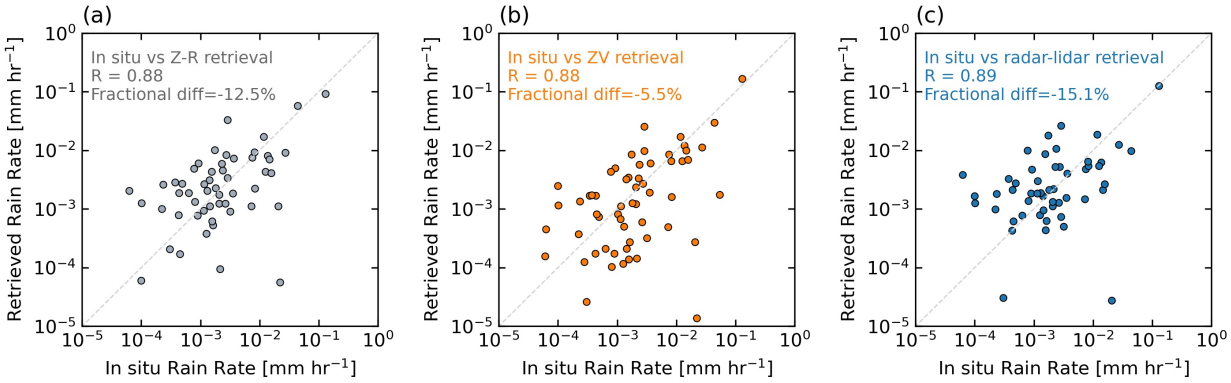

Figure 2.10 Comparison of in situ estimates with (a) Z-R retrieval, (b) ZV retrieval, and (c) radar-lidar retrieval for the entire campaign. The retrieved rain rates plotted here were extrapolated to the aircraft level (see Figure 2.9) to compare with the in situ data. The fractional difference is calculated as the difference between the retrieved and in situ mean values divided by the average of the means.

2.5 Vertical distribution of precipitation properties

In this section, we will apply the precipitation observations and retrievals to study the vertical distribution of precipitation properties.

Figure 2.11 shows a violin plot of in situ measured precipitation properties at different altitudes and retrieved precipitation properties below the lidar-inferred cloud base. For each dataset, the white dot represents the median value, while the black bar represents the interquartile range. Perhaps surprisingly rain rate decreases going downward from the top half of the cloud (i.e. the largest rain rates are in the upper portion of the cloud). Medians of rain rate at the cloud top half, cloud bottom half, and below the cloud are 0.022 mm hr^{-1}, 0.007 mm hr^{-1}, and 0.001 mm hr^{-1}. Similar to rain rate, there is also a decrease in precipitation number concentration (N_{precip}) and precipitation liquid water content (LWC_{precip}) moving downward from the top half of the cloud. In contrast, D_{precip} and σ_{precip} increase moving downward, that is bigger particles in the bottom half, and (just) below cloud. Overall, the retrieved precipitation properties (below the cloud base) compare well with the in situ estimates from the sawtooth below-cloud segments.

How do precipitation properties vary below cloud base? Figure 2.12 provides a more detailed view of the vertical distribution of precipitation properties below cloud base. Here, the column shows rain rate, N_{precip}, LWC_{precip}, D_{precip}, and σ_{precip}, respectively. The first two rows are histograms for radar-lidar and ZV retrievals, respectively. The last row is a box plot that summarizes both retrievals by binning the data vertically every 100 meters. Here, we only consider data in those radar columns where rain extends at least 400m below cloud base. Overall, both the rain rate and LWC_{precip} decrease exponentially with distance (as the change in the position of the distribution peak is roughly linear with distance on a log scale). Both retrievals have similar values and rates of decrease (panel k and panel m). The e-folding distance over which the rain rate decreases to 1/e (37%) of its initial value is about 260m for radar-lidar retrieval and 340 m for ZV retrieval. N_{precip} also decreases with distance, but we find the radar-lidar retrieval decreases more rapidly within 200m below the cloud base, and the ZV retrieval

shows higher N_{precip} than radar-lidar retrieval at different levels. This is consistent with (a result of) assuming a shape factor of zero in the ZV retrievals. The mean D_{precip} and σ_{precip} both increase with distance. Compared to radar-lidar retrieved D_{precip}, ZV retrieved D_{precip} is smaller overall (again consistent with the assumed shape factor), and has much less spread (variation) at any given altitude. Figure 2.11d shows that radar-lidar retrieved D_{precip} compares better with the in situ estimated D_{precip} from the below-cloud portion of the sawtooth legs than the ZV retrieved D_{precip}.

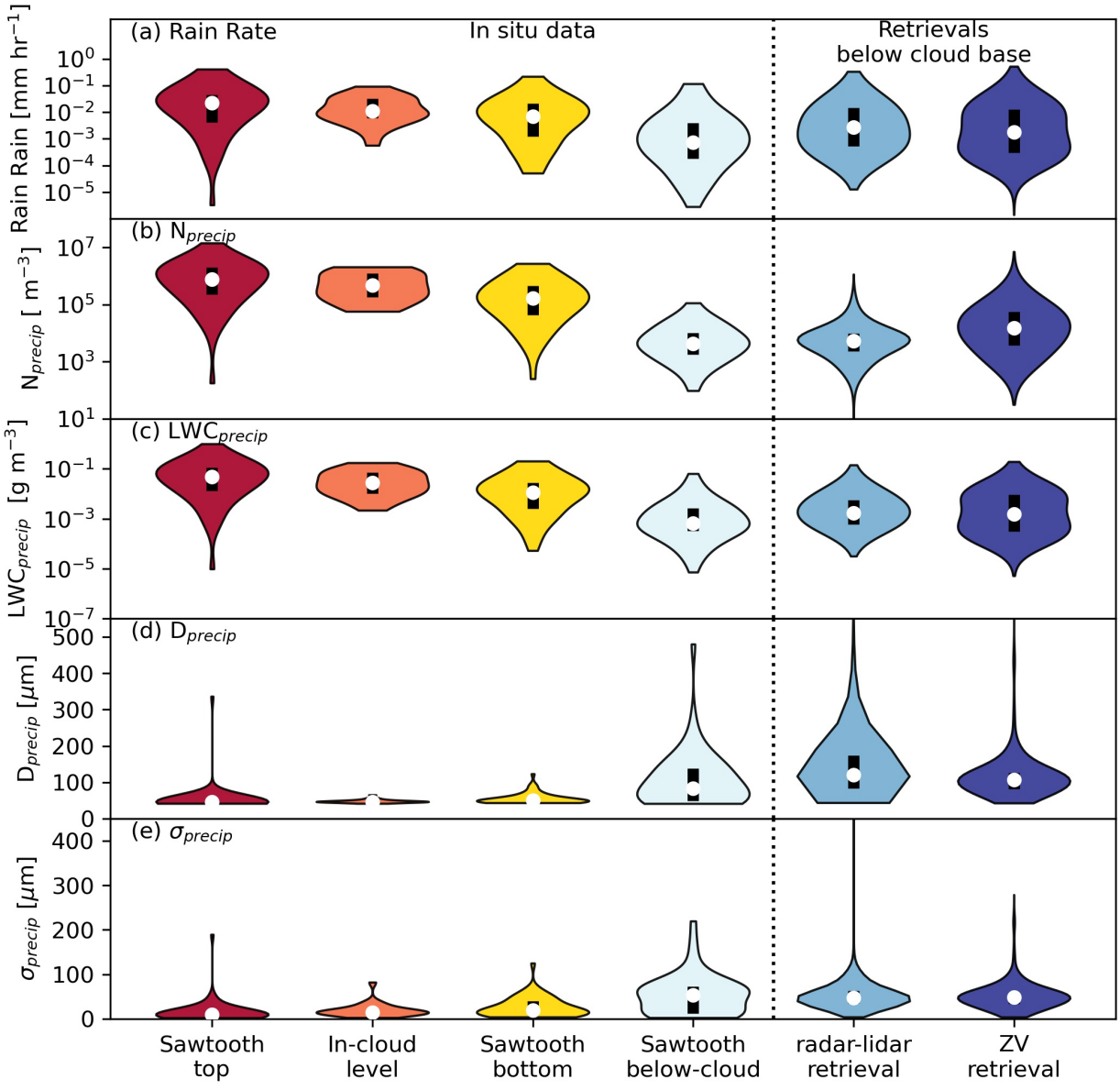

Figure 2.11 Violin plot for in situ measured precipitation properties at different altitudes and retrieved precipitation properties below cloud base: (a) rain rate (or precipitation liquid water flux), (b) precipitation number concentration N_{precip}, (c) precipitation liquid water content LWC_{precip}, (d) precipitation liquid water content weighted mean diameter D_{precip}, (e) precipitation liquid water content weighted width σ_{precip}. A violin plot can be regarded as a hybrid of a box

plot and a kernel density plot. For each dataset, the white dot represents the median value, while the black bar represents the interquartile range, and the outer shape is the kernel density estimation to show the distribution of the data. In situ measured precipitation properties are from these legs (as marked in Figure 2.1): the top half of the cloud layer from sawtooth legs (sawtooth top); the bottom half of the cloud layer from sawtooth legs (sawtooth bottom); the below-cloud portion of the sawtooth legs (sawtooth below-cloud); and in-cloud level legs.

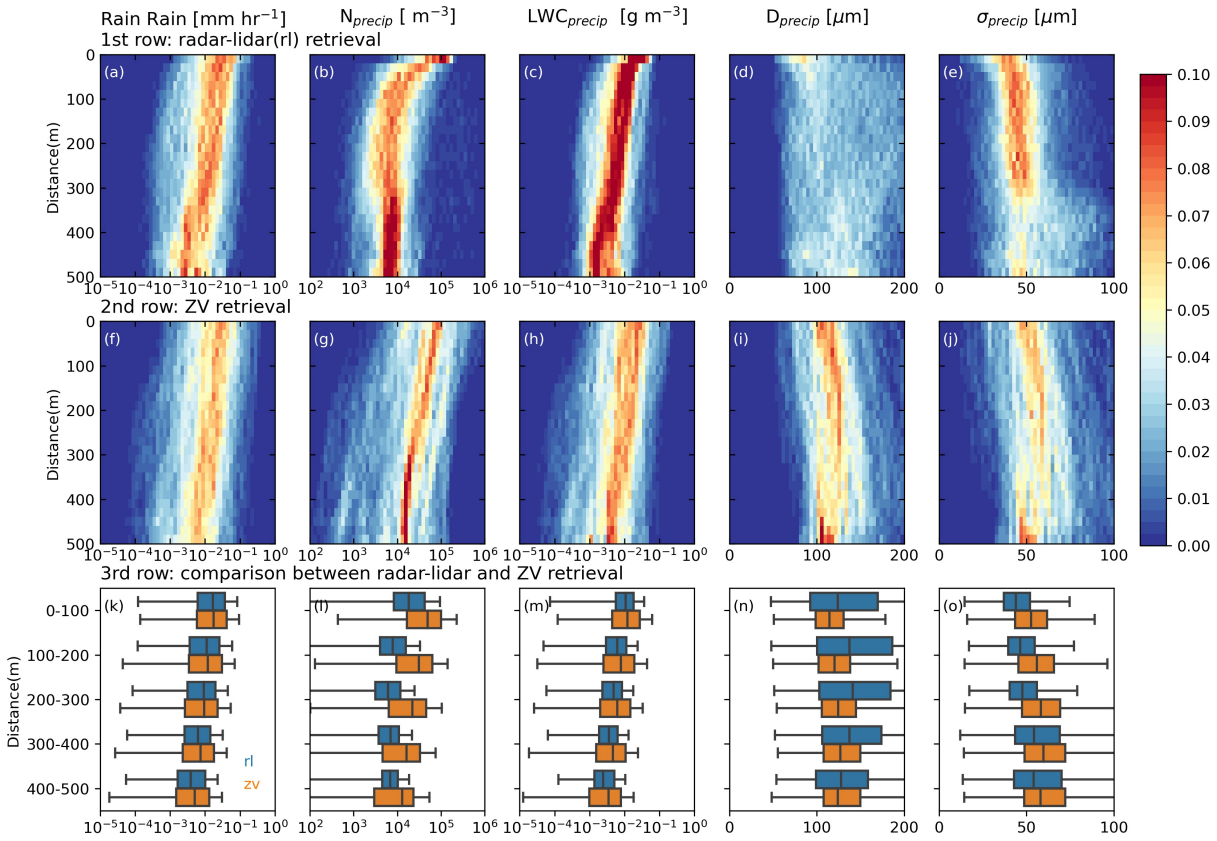

Figure 2.12 Vertical distributions of below-cloud-base liquid precipitation properties from retrievals (each column is rain rate, N_{precip}, LWC_{precip}. D_{precip}, σ_{precip} respectively). The first and second row is the histogram of retrieved precipitation properties below-cloud-base (data are normalized at each level), and y axis is the distance away from the cloud-base. The first row is the results from radar-lidar retrievals, the second row is the results from ZV retrievals. The last row is the box plot that summarizes the data in the first two rows by binning the data vertically every 100 meters, where blue boxes are from radar-lidar retrievals, and orange boxes are from ZV retrievals.

2.6 Rain rate dependence on cloud depth and aerosol concentration

In this section, we examine the degree to which precipitation can be diagnosed from cloud depth and cloud droplet or aerosol number concentration in the form (e.g. Comstock et al., 2004; Terai et al.,2012; Mann et al., 2014)

$$R_{CB} = k\, H^{\alpha}\, N^{\beta} \quad (2.11)$$

where N is usually the cloud droplet (N_d) or aerosol number concentrations (N_a), H is cloud depth or liquid water path, and R_{CB} is rain rate at cloud base. To our knowledge, such a relationship has not been examined over the SO, except by Mace and Avey (2017) who used satellite retrievals. To examine this relationship over the SO, we focus on the below-cloud level legs (as marked in Figure 2.1) where variables can be obtained simultaneously and use the radar-lidar retrieved rain rate for R_{CB}, use the difference between cloud top and cloud base for H, and the accumulation mode aerosol concentrations with diameters larger than 70 nm from the UHSAS for N_a. The UHSAS essentially measures the dry particle size, as the collected aerosol particles were subjected to drying using a de-icing system, which modulates the temperature and pressure of the sampled air to prevent the formation of ice in the inlet (Sanchez et al., 2021; McCoy et al. 2021). To ensure that aerosol measurements from UHSAS were not contaminated by clouds or precipitation, we applied screening to the UHSAS data using both CDP and 2DS probes, following the method described by McCoy et al. (2021). We discarded data when the CDP liquid water content exceeded 0.01 g m^{-3} or the 2DS measured particle concentration exceeded 0.001 cm^{-3}. Once these thresholds were exceeded, samples within the following 10 seconds were also removed as an extra precaution.

First, we broadly examine the rain rate dependence on either cloud depth or aerosol concentration, individually. Figure 2.13a shows a joint histogram of rain rate at cloud base and cloud depth. The histogram shows that rain rate (at cloud base) scales with cloud depth, such that thicker clouds are associated with higher rain rates. This is consistent with previous studies (e.g. vanZanten et al., 2005; Pawlowska and Brenguier, 2003; Geoffroy et al., 2008). And to demonstrate the rain rate dependence on aerosol concentration, Figure 2.13b shows the probability density function of rain rate partitioned for conditions with low aerosol concentrations (lower than the first quartile, marked as blue) and high aerosol concentrations (higher than the third quartile, marked as red). Figure 2.13b shows that overall higher aerosol concentrations are associated with lower rain rates, consistent with aerosol suppression of precipitation.

How does rain rate relate to both cloud depth and aerosol concentration? To derive the coefficients in equation 2.11, we divided cloud depth (H) up to 600m into 6 bins, and divided aerosol concentrations (N_a) into 4 bins, and calculated the median rain rate for each H and N_a pair. Then we performed a linear least square regression on the natural logarithms of data from these 24 bins (Figure 2.13c). The derived relationship is $R_{CB} = 1.41 \times 10^{-9}\, H^{3.1}\, N_a^{-0.8}$, with H in m, N_a in cm^{-3}, and R_{CB} in mm hr^{-1}. Using a bootstrap resampling technique, we estimate that the one-sigma uncertainty range for the exponent α (for H) ranges from 2.8 to 3.4, while the range for exponent β (for N_a) ranges from -1.0 to -0.7. The relationship we derive here is broadly similar to previous studies for stratocumulus in other regions. Specifically, the exponent α for cloud depth typically is about 3 (vanZanten et al., 2005; Pawlowska and Brenguier, 2003; Lu et al., 2009), and the exponent β for number concentration (cloud droplet concentration or cloud condensation nuclei) typically ranges between -1.75 to -0.66 (vanZanten et al 2005; Mann et al., 2014; Lu et al., 2009; Comstock et al., 2004). The exponent β of -0.8 for aerosol concentration we derived here is smaller than exponent β of -0.32 in Mace and Avey (2017, hereafter M17),

estimated using satellite-estimated cloud droplet number concentration, liquid water path, and rain rate for the SO. We will discuss this difference further in the next section.

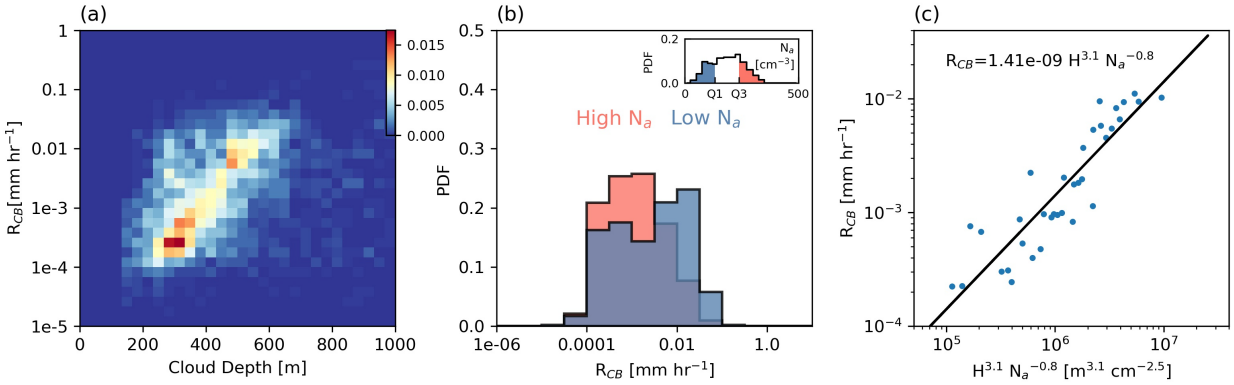

Figure 2.13 (a) Histogram of rain rate plotted as a function of cloud depth. (b) The probability density function of rain rate for conditions with low aerosol concentrations (lower than the first quartile, marked as blue) and high aerosol concentrations (higher than the third quartile, marked as red). (c) The rain rate at the cloud base is plotted as a function of the cloud depth, H, and aerosol concentration, N_a. Here H and N_a are the middle points for each cloud depth and aerosol concentration bin, while the rain rate at the cloud base is taken as the median value of rain rates in each cloud depth and aerosol concentration bin. The solid line shows the parametrization described in the main text.

2.7 Conclusions

In this study, we examine in-and-below-cloud precipitation properties for stratocumulus over the Southern Ocean (SO), using data collected from airborne W-band Cloud Radar (HCR), High Spectral Resolution Lidar (HSRL), and various in situ probes during the Southern Ocean Clouds Radiation Aerosol Transport Experimental Study (SOCRATES) in January-February 2018.

Overall, we find that about 60% of the stratocumulus were precipitating, and about 80% of the stratocumulus were cold-topped (with a cloud top temperature < 0°C) based on periods where the aircraft were flying below cloud and the radar and lidar pointing toward the zenith. We determine the precipitation phase using the lidar particle linear depolarization ratio PLDR and find that about 60% of the precipitation is liquid phase, and about 20% of the precipitation is ice phase, with the remaining 20% being ambiguous. While we can not rule out the possibility that any individual ambiguous case is pure liquid, most of the ambiguous phase cases are likely to have ice or mixed-phase precipitation present. Further, for cold-topped clouds, we find that when the reflectivity factor is less than about –10 dBZ, the precipitation is predominantly liquid, while for reflectivity factors greater than 0 dBZ, precipitation is predominantly ice. These results are similar to what was found by Mace and Protat (2018) based on CAPRICORN data during March-April 2016, as well as a recent study by Tansey et al. (2023) based on surface data collected at Macquarie Island (54.5 °S) between March and November 2016. The SOCRATES data, collected in the Southern Hemisphere Summer, in January and February 2018, suggests this relationship is likely characteristic of SO low clouds throughout the year, and suggests that the measured reflectivity factor might be used as a proxy to determine the precipitation phase for

cold-topped Southern Ocean stratocumulus with CloudSat (or other "radar only") retrievals where no other information is available to constrain the precipitation phase.

For liquid-phase precipitation, we performed retrievals for precipitation rain rate and other microphysical parameters based on radar and lidar, with the goal to test a hierarchy of retrieval methods, from the simplest Z-R relationship approach where only radar reflectivity (Z) is used to estimate the rain rate, to a reflectivity-velocity (ZV) retrieval where there are two observables (inputs to the retrieval), to a radar-lidar retrieval with three observables. Our evaluation shows that rain rates from the Z-R, ZV, and radar-lidar retrievals all compare well with the in situ rain rates, with Pearson correlation coefficient of 0.88. 0.88 and. 0.89, and fractional difference (difference between the retrieved and in situ mean value divided by the average of the means) of only –12.5%, –5.5%, and –15.1%, respectively. In addition to rain rate, ZV, and radar-lidar retrievals can retrieve other precipitation properties, such as precipitation number concentration, precipitation liquid water content, number concentration, size, and width. The overall statistics and distribution of these retrieved precipitation properties below the cloud base, also compare well with in situ estimates from the sawtooth below-cloud segments. This good performance gives us some confidence in using these retrieval techniques for SO stratocumulus, including in our recently published manuscript that examines coalescence scavenging in SO stratocumulus (Kang et al., 2022).

Despite the good retrieval performance overall, there are important caveats. When developing the power-law relationships between reflectivity (Z) and rain rate (R) following $Z = aR^b$ we found the b exponent varied little with altitude and had a value around 1.2 to 1.4. This is similar to values obtained in previous studies for stratocumulus in other regions (Comstock et al., 2004; vanZanten et al., 2005). The a coefficient, on the other hand, increases as one moves from the cloud layer to the surface. In general, one can derive a power-law relationship between Z and R based on the assumption of a modified gamma distribution (e.g., Rosenfeld and Ulbrich 2003), and doing so shows that one should expect the a coefficient to depend on the total droplet number concentration. Given the vertical variations in the precipitation droplet number concentration (see Figures 2.11 and 2.12), the vertical variation in the a coefficient is not surprising. But such also hints that the a coefficient may well vary with the accumulation mode aerosol concentration or other factors that control the cloud droplet number concentration. So Z-R relationships should be used with some caution in studies intending to establish relationships between rain rates and aerosols. We also find that the derived Z-R relationships are sensitive to whether ones exclude drops with diameters smaller than 40 μm when in cloud, because these drops make a non-trivial contribution to total liquid water flux, as perhaps first noted by Nicholls (1984). Our analysis suggests that below-cloud Z-R equations should be applied with caution to in-cloud reflectivity measurements, and should be expected to underestimate the total liquid water flux in cloud.

Comparing the ZV retrieval with radar-lidar retrieval shows that both retrievals capture the mean vertical structure of precipitation microphysics below cloud. Based on in situ data and retrievals, we found that rain rate, precipitation number concentration (N_{precip}), precipitation liquid water (LWC_{precip}) all decrease as one gets closer to the surface, while precipitation liquid water content weighted mean diameter (D_{precip}) and width(σ_{precip}) increases. The e-folding distance over which the rain rate decreases to 1/e (37%) of its initial value is about 260m for radar-lidar retrieval and 340 m for ZV retrieval. However, we find that both D_0 and N_{precip} from the ZV retrieval have

less spatial variability than that from the radar-lidar retrieval, and assuming a shape factor of $\mu = 0$, results in the ZV retrieved mean D_0 being a bit too small and N_{precip} being too large as compared to the radar-lidar retrieval. This is because the shape factor is not constant and in particular, because the shape factor in the stronger precipitation shafts below the thicker portion of the clouds should be larger than zero (because the precipitation DSD is narrower with a more well-defined peaked rather than a broad exponential-like distribution).

This study also explored rain rate dependence on cloud depth and aerosol concentration. Rain rate at cloud base (R_{CB}) increases with cloud depth (H) and decreases with aerosol concentration (N_a). Using a least-squares regression, we found R_{CB} varies with $H^{3.1}\, N_a^{-0.8}$, which is broadly consistent with estimates for stratocumulus in previous studies over other regions (vanZanten et al., 2005; Pawlowska & Brenguier, 2003; Lu et al., 2009; Mann et al., 2014; Lu et al., 2009; Comstock et al., 2004). However as noted in section 2.6, our results differ from the satellite-based estimates for the SO by Mace and Avey (2017), hereafter M17, who suggest an exponent of -0.32 for the aerosol concentration based on satellite retrievals. M17 also noted that their estimates differ from previous studies in other regions. There are a variety of potential reasons for the different results in our study and in M17. The first obvious reason is different data sources. Our study used in situ measured N_a and retrieved rain rate with airborne radar and lidar measurements, while M17 used N_d, liquid water path, and rain rate derived from MODIS and Cloudsat based on an optimal estimation algorithm. Another reason might be different cloud populations; where in our study about 80% of the clouds are cold-topped, M17 restricted their analysis to warm-topped clouds. Data collected during the Macquarie Island Cloud and Radiation Experiment (MICRE), suggest that warm-topped SO clouds are geometrically thinner and closer to the surface than cold-topped clouds (Tansey et al., 2023). As-is, we end this chapter here, leaving a regime-dependent analysis of precipitation susceptibility for a future study. As more data are collected, including in future campaigns such as the upcoming Clouds And Precipitation Experiment at Kennaook (CAPE-K) that will begin in March 2024, the aerosol sensitivity of low altitude SO clouds are certain to be the focus of future multi- or cross-experiments studies.

Chapter 3 Source-Sink Framework for Droplet Number Concentration in Southern Ocean Low Clouds

3.1 Introduction

Low-altitude stratiform clouds are ubiquitous over the Southern Ocean (SO) (Mace et al., 2009, 2010, 2020; Huang et al., 2016). These clouds are crucial to climate because they reflect shortwave radiation back to space, cooling the planet, locally reducing ocean heat uptake (Sallée et al., 2013; Schneider & Reusch, 2016), and profoundly affecting the global atmospheric circulation (Hwang and Frierson, 2013; Ceppi et al., 2013) and global cloud feedbacks (Gettelman et al., 2019; Zelinka et al., 2020). The fraction of sunlight reflected back to space (i.e. cloud albedo) depends strongly on the cloud microphysical properties (D. T. McCoy et al., 2014). In particular, the cloud droplet number concentration (N_d) is a primary determinant of cloud albedo (Twomey et al., 1977; Merikanto et al., 2010; Diamond et al., 2020), a key variable that links aerosol and cloud microphysical properties (Boucher et al., 1995; Lohmann & Feichter, 2005), and also influences cloud macrophysical properties such as cloud depth, cloud cover, thermal emissivity, and liquid water path (Grosvenor et al., 2017; Christensen et al., 2020; Garrett & Zhao, 2006; Zhao & Garrett, 2015). Thus, a deeper understanding of the key controls on N_d is essential for understanding the climate effect of SO low clouds.

In liquid phase clouds, N_d is largely controlled by the balance between available aerosols in the marine boundary layer (MBL) that serve as cloud condensation nuclei (CCN) and the loss of available CCN through the subsequent collision-coalescence of cloud droplets, which leads to precipitation and reduction of aerosol concentration. The removal of aerosols by their activation into cloud droplets and subsequent merger into precipitation-sized particles through collision-coalescence, hereafter coalescence scavenging, has long been recognized as a leading (if not the dominant) mechanism by which aerosols are removed from the BL (Feingold et al., 1996; Wood et al., 2012). This includes over the SO where aircraft observations have shown that aerosols that serve as CCN have lower concentrations in the BL under cloudy conditions than clear conditions (Hudson et al., 1998; Yum & Hudson, 2004).

Satellite observations show that SO low clouds have significant seasonal and latitudinal dependencies. Low clouds have higher mean N_d during the austral summer than winter, as well as higher mean N_d near Antarctica (south of 55° to 60° S) (D. T. McCoy et al., 2014; I. L. McCoy et al. 2020). Previous studies have shown that the seasonal and spatial patterns of SO N_d are strongly influenced by aerosol sources and coalescence scavenging. I. L. McCoy et al. (2020) hypothesized that the N_d minimum off the coast of Antarctica was due to enhanced coalescence scavenging associated with the SO storm track. Using a simplified budget model (Wood et al., 2012, hereafter W12), along with CloudSat-derived precipitation estimates, I. L. McCoy et al. (2020) found that coalescence scavenging could drive down mean N_d to about 30% of the value that would occur without coalescence scavenging.

However, differences in aerosol sources compete with precipitation sink patterns in explaining the latitudinal dependence. Sources contribute heavily to seasonal differences, with

ocean biology-sourced aerosols dominating CCN in the summertime and sea spray dominating in the winter (Ayers & Gras, 1991; Quinn et al., 2017). Observations and model studies (e.g., Korhonen et al., 2008) suggest that surface dimethyl sulfide (DMS) emissions associated with phytoplankton can be transported from the surface to the free troposphere (FT) where DMS oxidation products nucleate into new particles (Clarke et al., 1998; Weber et al., 2001). These particles subsequently return to the MBL through entrainment and subsidence associated with mid-latitude storm systems (Covert et al. 1996) and grow into CCN (Raes, 1995; Quinn et al., 2017; Sanchez et al., 2021). I. L. McCoy et al. (2021) suggest that these FT Aitken particles (diameters ≤ 0.1 μm), in addition to acting as the primary source of CCN, also buffer SO CCN and N_d against precipitation removal during biologically active time periods. Thus the latitudinal pattern may be driven in part by the large increases in the amount of phytoplankton and thus DMS production in the summertime seasonal ice zone around Antarctica (Curran & Jones, 2000) and increases in small aerosol particles south of the oceanic polar front during the SO summer (Humphries et al., 2016, 2021). Across the SO, strong correlations are observed between satellite retrieved N_d and sea surface chlorophyll-a concentrations (a proxy for phytoplankton biomass) (D. T. McCoy et al., 2015). Summertime MBL accumulation mode aerosols (include most CCN) observed during the recent Southern Ocean Clouds Radiation Aerosol Transport Experimental Study (SOCRATES; McFarquhar et al., 2021) were dominated by sulfur-based particles (~70% by number) which likely had a biogenic origin. Sea-spray particles also contributed to the total (~30% by number) but many of these particles (40%) were still influenced by ocean biology as their compositions were salt enriched by sulfur and depleted in chlorine through uptake and condensation of sulfur gases (Twohy et al., 2020).

There is little doubt that aerosols from biological sources play a large role in both the seasonal and latitudinal variations in SO low cloud N_d. However, coalescence scavenging may have a non-trivial influence in determining the pattern of N_d across the SO and its influence over the SO remains poorly understood. In this study, we examine this through a N_d budget model framework. We first test the ability of the W12 budget model to predict N_d for SO stratocumulus using SOCRATES observations. This model was developed in the context of observations gathered in subtropical stratocumulus and has been applied in other subtropical settings (Mohrmann et al., 2018; Zheng et al., 2018). While it was applied by I. L. McCoy et al. (2020) to the SO, it has not been tested in any detail at mid-to-high latitudes of either hemisphere. We find that the model (after being adjusted to better represent SO sea spray aerosols) can predict much of the observed N_d variability (section 3.3.1). This model skill is apparent in both regimes of liquid and mixed-phase precipitation (section 3.3.2), suggesting coalescence scavenging is a dominant sink for CCN. We then use the model to examine the relative importance of FT and surface sources of CCN and, to assess the importance of coalescence scavenging in controlling SO stratocumulus N_d (section 3.3.3).

3.2 Data and Methods

To quantitatively study the sources and sinks that control N_d, we apply a budget model, developed by W12, that considers the main sources and sinks of CCN and thus N_d:

$$\frac{\partial N}{\partial t} = \frac{\partial N}{\partial t}\Big|_{FT} + \frac{\partial N}{\partial t}\Big|_{SFC} + \frac{\partial N}{\partial t}\Big|_{New} + \frac{\partial N}{\partial t}\Big|_{PRECIP} + \frac{\partial N}{\partial t}\Big|_{DRY} + \frac{\partial N}{\partial t}\Big|_{ADV} \quad (3.1)$$

The terms on the right-hand side refer to the time tendency of CCN due to entrainment from the FT, primary production at the sea surface from sea-spray, new particle formation in MBL, precipitation sink, dry deposition, and advection, respectively. For simplicity, W12 neglected three terms as they are small on average in MBL. W12 estimated dry deposition, $\frac{\partial N}{\partial t}|_{DRY}$, to be less than $2cm^{-3}d^{-1}$and advection, $\frac{\partial N}{\partial t}|_{ADV}$, to be 10 $cm^{-3}d^{-1}$or less. As for the new particle formation, this term has been set to zero because previous observational studies (e.g., Covert et al., 1996; Bates et al., 1998) suggest that new particle formation in the MBL infrequently occurs and is unlikely to contribute significantly to the mean CCN concentration. Rather, new particle formation appears to occur primarily in the FT (e.g., Humphries et al., 2016; Sanchez et al., 2021) and act as the key source for CCN once they have been brought in the sub-cloud layer and grown to larger, near accumulation-mode sizes (e.g., Covert et al., 1996; Raes, 1995; Quinn et al., 2017). It is nonetheless possible that new particle formation or activation of smaller (Aitken sized) particles may be important over the SO when accumulation mode aerosols are low (I. L. McCoy et al. 2021). Further study is needed on this topic, but for the present study it is neglected. The remaining terms for the FT source, surface source, and precipitation sink were parameterized. W12 derived a steady-state (or equilibrium solution) as N_{eq} for cloud droplet number concentration by setting the time tendency of CCN to zero (i.e. left-hand side of equation 3.1) and substituting in the parameterized source and sink terms:

$$N_{eq} = \frac{(N_{FT} + \frac{F(\sigma)U_{10}^{2.8}}{Dz_i})}{(1 + \frac{hKP_{CB}}{Dz_i})} \tag{3.2}$$

where N_{FT} is the FT CCN concentration, z_i is the MBL depth, D is the large-scale lower tropospheric divergence, $F(\sigma)$ is a sea spray source function that depends on the supersaturation (Clarke et al., 2006), U_{10} is the wind speed at 10 m, h is cloud thickness, P_{CB} is the precipitation rate at the cloud base and K is a constant that depends on the collection efficiency (Wood, 2006). Note that here we have modified the power-law relationship in the surface source parametrization from $U_{10}^{3.41}$ (as in W12) to $U_{10}^{2.8}$. Recent studies (Revell et al., 2019; Hartery et al., 2020) show that the previous $U_{10}^{3.41}$ parametrization (Monahan & Muircheartaigh, 1980; Gong, 2003; Clarke et al., 2006) can overestimate the surface source by a factor of 2-4 for the SO, while $U_{10}^{2.8}$ is a better fit for high-wind environments. Hartery et al. (2020) validated the new $U_{10}^{2.8}$ parametrization by comparing the predicted sea spray aerosol concentration with aircraft measurements during SOCRATES. In section 3.3.3, we will compare the budget model results using these two different parameterizations.

In this study, we test the budget model by using SOCRATES observations to calculate N_{eq} and compare it with the observed N_d. The SOCRATES campaign took place during January-February 2018 during which the aircraft conducted 15 flights over the SO (McFarquhar et al., 2021). Specifically, we estimate the model inputs (e.g., N_{FT}, P_{CB}, U_{10}) from the aircraft measurements, as described below.

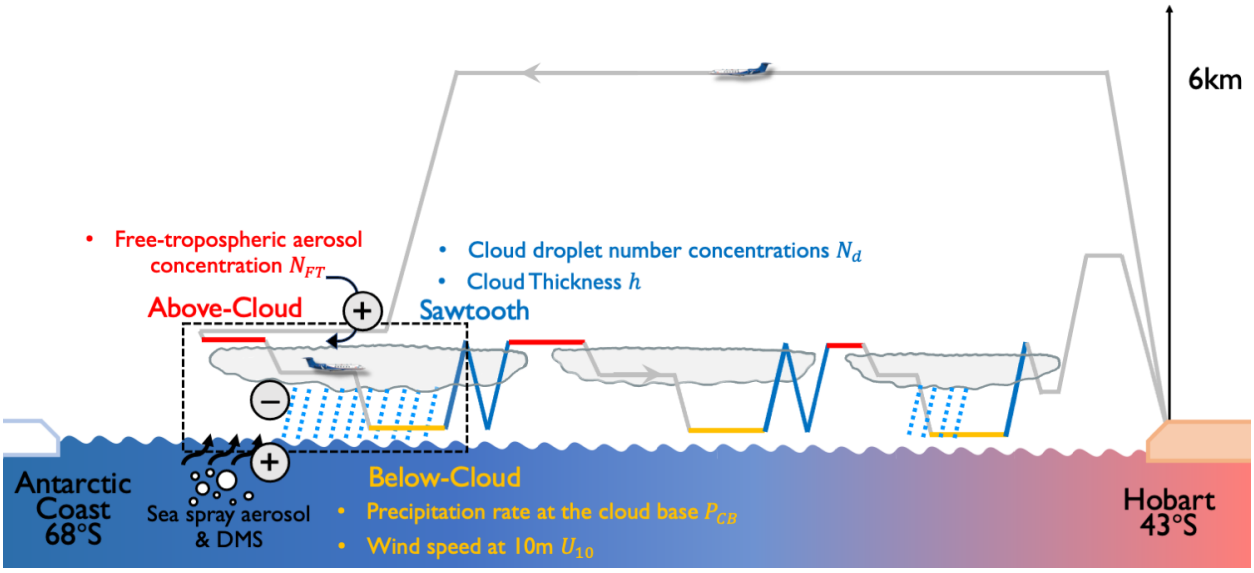

Figure 3.1 A schematic showing a typical flight module used by the GV aircraft during the SOCRATES campaign. Grey lines represent the flight track, with below-cloud legs given in yellow, above-cloud legs in red, and nearby sawtooth legs in blue. Circles with + and – signs denote the main sources and sinks in the budget model.

During SOCRATES, typically, the aircraft flew south at high altitude, descended to just above cloud top before descending through the cloud, and then turning back toward Hobart. During the return flight, cloud and aerosol properties were sampled *in situ* using a standard flight module (Figure 3.1 is a schematic showing a typical flight module). The flight modules consisted of fixed activities such as ramp ascents and descents (sometimes called sawtooths), as well as ~10 minute above-, in-, and below-cloud legs flown at a constant altitude. Our analysis is focused on the below-cloud legs where the cloud-radar and lidar were pointing upward and could be used to assess precipitation. Specifically, we calculated N_{eq} based on the mean rain rate for the below-cloud legs and other supporting observations from surrounding legs, as described below, and obtained an associated estimate for observed N_d from cloud droplet probe (CDP) measurements taken in the adjacent in-cloud ramps. The observed cloud are close to adiabatic with little systematic variation in the observed N_d with height (Kang et al. 2021).

For FT CCN concentration (N_{FT}), we use measurements from the Ultra-High-Sensitivity Aerosol Spectrometer (UHSAS; DMT, 2013) during the nearby above-cloud leg. The UHSAS measures the size distribution and concentration of aerosols with diameters between 60 and 1000 nm. We calculated the concentration of aerosols with diameters larger than 70 nm and discarded 60-70 nm diameter range due to instrument noise (Sanchez et al., 2021). As discussed in Sanchez et al. (2021), the UHSAS concentration above 70 nm diameter have a strong equivalence to the CCN concentration at 0.3 % supersaturation.

For the surface source term, we use aircraft-measured wind speed from the below-cloud leg and extrapolate it to 10 m assuming a logarithmic wind profile (Hsu et al., 1994). A value of

supersaturation σ = 0.3% is used, which yields a value for $F(\sigma)$ of 214 m^{-3} $(m\ s^{-1})^{-(b-1)}$ (where b is the wind speed exponent U_{10}^{b}) based on the parameterization of Clarke et al. (2006). We use 4 mm s^{-1} for the subsidence rate Dz_i, which is a typical value for low clouds in the subtropics and mid-latitudes, following I. L. McCoy et al. (2020).

For the precipitation sink term, the cloud thickness (h) is estimated from nearby sawtooth legs, where cloud top and cloud base are defined as the highest and lowest altitude with liquid water content (LWC) > 0.03 g m^{-3}, following Wood et al. (2011). The results of our analysis are not sensitive to reducing this LWC threshold to a lower value (e.g., 0.005 g m^{-3} as in Zhao et al., 2020). In a few cases, multilayer clouds were present and the top and bottom were chosen to span over the levels that were consistent with the radar and lidar boundaries observed during the below cloud leg. We set K = 2.25 m^2 kg^{-1}, which is a constant that depends on the collection efficiency of cloud droplets by drizzle drops (Wood, 2006). We estimate the liquid precipitation rate at the cloud base (P_{CB}) based on the radar-lidar technique of O'Connor et al. (2005). This retrieval is run during the below-cloud legs when both the airbone W-band radar and high spectral resolution lidar (HSRL) were pointing upward, and only when the precipitation is identified as liquid phase. The precipitation phase is determined using HSRL measured particle linear depolarization ratio (PLDR) averaged over all levels below the cloud base. This measurement is taken below cloud base rather than at cloud base to prevent multiple scattering from significantly impacting the PLDR. Photons that are single-scattered from spherical droplets generate no PLDR. We interpret values of PLDR < 0.02 in each lidar column to be indicative of liquid precipitation, and PLDR > 0.05 to be ice, with PLDR values in between being mixed or ambiguous. In section 3.3.2, we define each below-cloud leg as a "liquid case" if 10% or less of the lidar columns have a PLDR > 0.05 or as a "mixed-phase case" otherwise.

We assess the fractional contribution of coalescence scavenging to N_d by computing the ratio between N_{eq} calculated with and without the precipitation sink, which is simply:

$$\frac{N_{eq}(precip)}{N_{eq}(no\ precip)} = \frac{1}{(1 + \frac{hKP_{CB}}{Dz_i})} \tag{3.3}$$

3.3 Results and Discussion

3.3.1 Evaluating the N_d Budget Model Accuracy

To quantify the accuracy of the budget model, we test the model using *in situ* observations from SOCRATES flights obtained as described in section 3.2. Figure 3.2a shows a comparison of observed N_d and model predicted equilibrium values (N_{eq}) with all the source and sink terms and the adjusted wind speed parametrization as in equation 3.2. Each point represents a below-cloud leg sample that had sufficient supporting observations from surrounding legs for the model to be applied. (The aircraft-derived inputs for each sample are given in Appendix Table B1, with corresponding statistics also given in Appendix Table B2). Circular symbols are cases dominated by liquid precipitation while diamond-shaped symbols are mixed-phase cases (as determined from the lidar PLDR, see section 3.2). Implications of precipitation phase in the budget model results will be discussed in the next section.

Considering all cases together (Figure 3.2a), we find the budget model performs remarkably well with a correlation coefficient of 0.72. Bias is also quite low, where observed N_d is 101 cm^{-3} while predicted N_{eq} is 106 cm^{-3}. This level of performance with a low bias and a correlation coefficient ~0.7 is comparable to the performance of satellite retrievals for N_d (Kang et al., 2021). This confirms that the budget model, which has been previously applied over the sub-tropics (W12; Mohrmann et al., 2018; Zheng et al., 2018), can be used with confidence in the mid-latitudes once the wind speed parameterization in the surface term is appropriately adjusted. We will return to the topic of the wind speed and surface contribution to CCN in section 3.3.3.

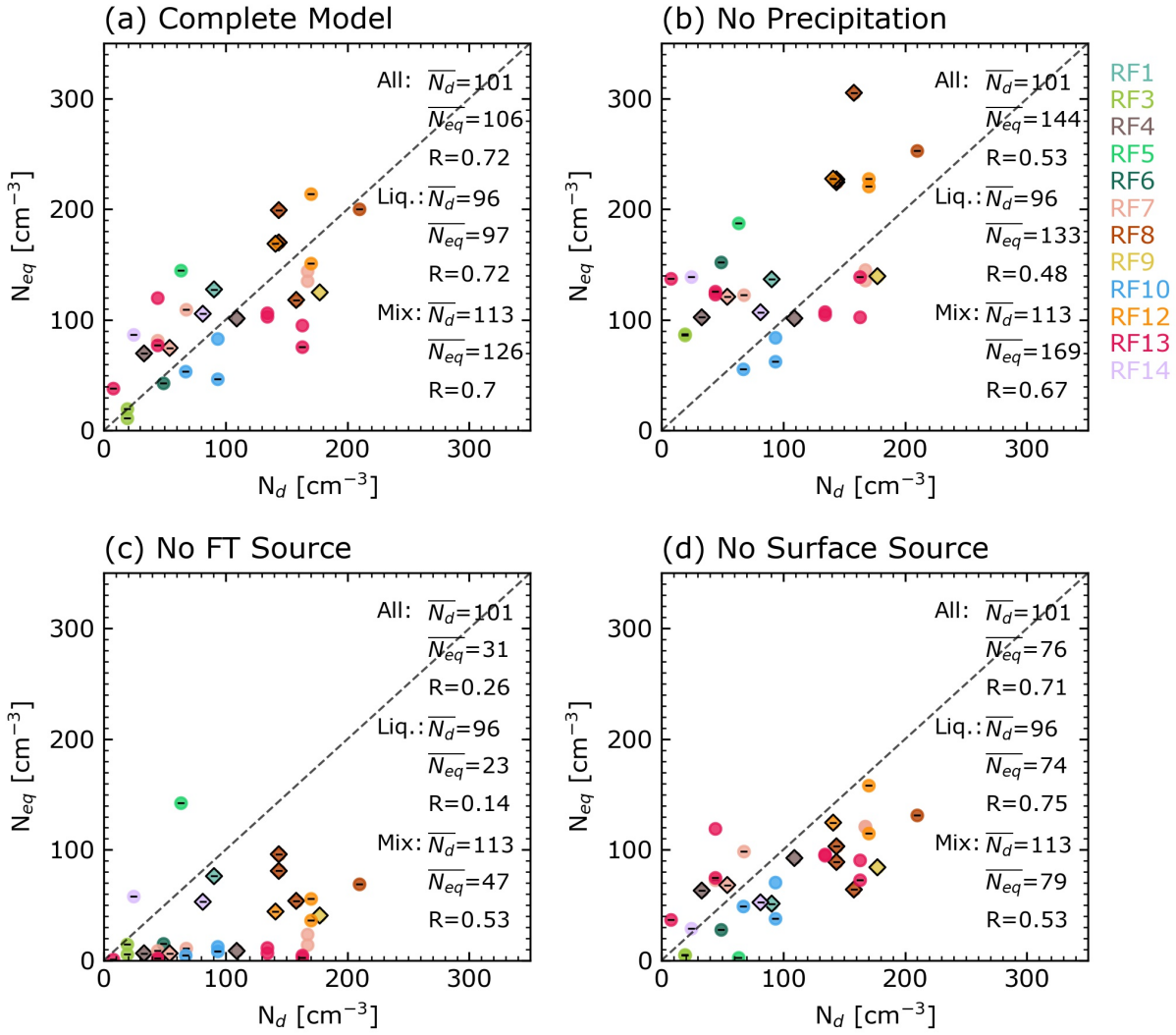

Figure 3.2 Comparison between observed N_d and computed N_{eq} using the budget model (equation 3.2) for SOCRATES flights: (a) with all the source and sink terms, (b) without the precipitation sink, (c) without the free tropospheric source, and (d) without the surface source. Different colors represent different flights. Circular points are cases associated with liquid precipitation. Black diamonds are the cases associated with mixed-phase precipitation, and, for

these cases, the mean retrieved rain rates from the liquid-columns is used for the ice-columns. Black hyphens marked the cases with mean rain rate > 0.001 mm h^{-1}.

3.3.2 Sensitivity of the Budget Model to Precipitation Phase

We hypothesize that CCN scavenging in SO clouds is dominated by liquid phase processes (i.e. coalescence scavenging). In general, ice precipitation that is driven by vapor deposition will not remove CCN from the atmosphere very efficiently (as one ice crystal may consume as little as one CCN particle if it grows exclusively by vapor deposition after a cloud droplet freezes) and it is only through riming, and to a lesser degree ice-aggregation, that ice precipitation might be expected to contribute significantly to CCN removal (Baltensperger et al., 1999; Garret et al., 2010). Rimed ice was frequently observed during SOCRATES and in past SO experiments, and secondary ice production through rime-splintering appears to be a significant factor in generating ice precipitation in SO clouds (Huang et al., 2017; McFarquhar et al., 2021; Wang et al., 2020). While rime-scavenging has long been recognized for its impact on the chemical composition of snow (Mitchell & Lamb 1989) and in recent years on its possible role in controlling black carbon in the Arctic (Hegg et al., 2011; Flanner et al., 2012; Qi et al., 2017; Xu et al., 2019), there has been little, if any, attention paid to the effect of riming on the overall CCN budget in mixed-phase clouds.

To test our hypothesis, Figure 3.2a compares N_{eq} to observed N_d separately for mixed-phase cases (diamonds) and liquid-phase cases (circles). For mixed-phase cases, we use the retrieved precipitation ONLY from lidar and radar columns with liquid precipitation. Specifically, we do not retrieve the precipitation rate during periods when lidar PLDR indicates ice is present, but rather we assume that the coalescence scavenging rate in the columns with ice precipitation is the same as in nearby liquid columns. In the context of the budget model we simply assign to the ice-columns the mean precipitation rate retrieved for the liquid-columns. We have not adjusted the budget model to include a rime-scavenging component. In general, we find that the mixed-phase cases behave similarly to the liquid cases (Figure 3.2a, Table B2). For liquid cases, we find a correlation coefficient of 0.72 and little bias (mean N_{eq} of 97 vs. mean N_d of 96 cm^{-3}), while for mixed-phase cases we find a correlation coefficient of 0.7 and slightly more bias (mean N_{eq} of 126 vs. mean N_d of 113 cm^{-3}). Our phase comparison results imply that CCN scavenging in SO clouds is likely dominated by liquid phase coalescence scavenging and the influence of mixed-phase processes on scavenging is small, at least in low-altitude SO cloud.

3.3.3 Quantifying the Relative Importance of Sources and Sinks

How important is coalescence scavenging in controlling N_d? We can easily answer this question in the context of the budget model. If the precipitation sink is removed from the model (Figure 3.2b), the predicted N_{eq} increases substantially, with the mean N_{eq} of liquid cases jumping from 97 cm^{-3} (Figure 3.2a) to 133 cm^{-3} (Figure 3.2b). Figure 3.2 shows the ratio between N_{eq} calculated with and without coalescence scavenging (equation 3.3) as a function of precipitation rate at cloud base. For precipitation rates below about 0.001 mm h^{-1} there is no appreciable reduction in N_{eq}. In Figure 3.2, cases with a precipitation rate greater than 0.001 mm h^{-1} are marked with black hyphens. The clear symbols (with no hyphen) remain clustered near but below the one-to-one line in Figure 3.2b, suggesting that source terms may be a bit too weak.

On the other hand, for cases with precipitation rates above 0.001 mm h^{-1}, there is a sharp reduction in N_{eq} such that when precipitation rates reach 0.1 mm h^{-1}, N_{eq} is reduced to about 10% of what it would have been without precipitation (Figure 3.3). This result demonstrates that light precipitation with rates < 0.1 mm h^{-1} significantly impacts CCN and N_d. The RF13 cases (pink points in Figure 3.2 and 3.3) provide an excellent demonstration of the importance of coalescence scavenging. Measurements during RF13 were collected across a Pocket of Open Cells (POC), that is a region of open-cell or broken stratocumulus surrounded by closed-cell or overcast stratocumulus (see Figure B1). POCs are commonly observed in sub-tropical stratocumulus but also occur in SO stratocumulus. Measurement campaigns such as VOCALS have highlighted the importance of precipitation for forming and maintaining these structures (Berner et al., 2011). Not surprisingly, we find that SO POCs are also associated with increased precipitation and lower N_d. During RF13, samples in the closed cellular clouds had large values of N_d (up to ~160 cm^{-3}) while the two samples in the open cellular cloud regions had much lower values of N_d (~8 cm^{-3} and ~44 cm^{-3}), despite having very similar aerosols in the FT and similar surface winds.

What is the relative importance of the FT and surface sources of CCN? Again, we can examine this question in the context of the budget model by neglecting the source terms in estimating N_{eq}. Comparing Figure 3.2c (no FT source) and Figure 3.2d (no surface source) suggests that entrainment of FT CCN is playing a larger role than surface sources in controlling N_d on average during SOCRATES. For liquid cases, when removing surface sources (Figure 3.2d) the mean predicted N_{eq} drops from 97 to 74 cm^{-3}, while removing FT sources (Figure 3.2c) reduces N_{eq} to 23 cm^{-3}. This broadly matches the dominance of sulfur-based accumulation mode aerosols over sea-spray aerosols in the MBL during SOCRATES (Twohy et al., 2021). Of course, the relative importance of the surface source varies with wind in Figure 3.2c, with those flights having higher wind speeds (e.g., RF05, RF08, RF12) having the largest N_{eq}. Regardless, our analysis confirms that the FT is a larger source of CCN than the surface over the SO in summer, an idea or hypothesis that has been advanced in previous studies based on surface measurements (Raes, 1995; Covert et al., 1996; Quinn et al., 2017). This differs, however, from the SO result in W12 where the budget model was originally introduced. W12 estimated the ratio of the CCN flux from the surface source to that from the FT and found that in the subtropics and tropics CCN was dominated by the FT source, but the mid-latitudes (including the SO), where winds are stronger, CCN was instead dominated by the surface source. The discrepancy between our analysis and W12 is due to the difference in the surface source parametrization. As noted in section 3.2, we have modified the power-law relationship in the surface source parametrization to one that is better suited to the SO. If we use the original budget model (W12) for SOCRATES cases, the predicted N_{eq} is overestimated (Figure B2), with the mean N_{eq} (223 cm^{-3}) of all cases more than twice of the observed mean N_d (101 cm^{-3}). This significant bias is caused by the high wind cases when using the original parameterization, as can be seen by examining the difference between N_{eq} and N_d as a function of wind speed (Figure B3). This highlights the importance of using a good parameterization for the surface source of CCN in the budget model and supports the $U_{10}^{2.8}$ relationship obtained by Revell et al. (2019) and Hartery et al. (2020) for the SO.

We also tested the performance of the budget model by using different input data for the surface wind speed and the precipitation rates. Specifically, we used ERA5 wind speed at 10 m ($U10_{ERA\text{-}5}$) as input, keeping all other inputs the same, and found the predicted N_{eq} still showed good agreement with observed N_d (Figure B4a). $U10_{ERA\text{-}5}$ is highly correlated with the U10 derived from aircraft measurements with a correlation coefficient of 0.96 and little bias (mean

$U10_{ERA\text{-}5}$ of 10.2 m s^{-1} vs. mean $U10_{airfract}$ of 9.5 m s^{-1}). To examine the sensitivity of the budget model to precipitation rate estimates, we instead used a cloud-base precipitation rate estimated from a radar reflectivity to rain rate (Z-R) relationship developed by Comstock et al. (2004). For liquid cases, the predicted N_{eq} shows good agreement with observed N_d (Figure B4b). We note that for liquid cases the Comstock Z-R relationship was developed for sub-tropical clouds but compares reasonably well with our radar-lidar retrieval-based rain rate estimate (Figure B5).

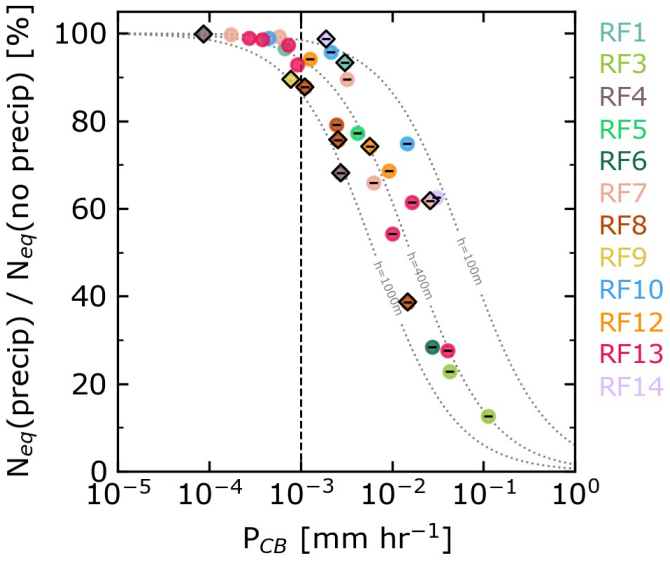

Figure 3.3 The ratio between calculated N_{eq} with and without the precipitation sink (equation 3.3) as a function of precipitation rate at cloud base. Different colors represent different flights. Black hyphens marked the cases with rain rate > 0.001 mm h^{-1} (which are to the right of the dashed reference line). Circular points are cases associated with liquid precipitation. Black diamonds are the cases associated with ice precipitation, and, for these cases, retrieved rain rates from liquid columns are used in the budget model. Grey dotted lines are the reference lines calculated using equation 3.3 assuming cloud depth h=100, 400, 1000 m. The average cloud depth is about 402±278 meters.

3.4 Conclusions

In this study, we present an evaluation of the simple source-and-sink budget model developed in W12 by testing its accuracy with aircraft-based observations during the SOCRATES. The aircraft observations are used to estimate inputs to the budget model: the FT CCN concentration, near-surface wind speed, and cloud-base precipitation rate. We find that the budget model, after the CCN source term is adjusted to better represent SO sea spray aerosols, predicts SO N_d with little bias and a correlation coefficient of about 0.7.

SOCRATES flights sampled in regimes where liquid-only and mixed-phase precipitation were present. We find that the budget model, when using only the liquid contribution to the precipitation rate (to estimate the coalescence scavenging rate), is able to predict N_d for both liquid and mixed-phase cases. This suggests that rime scavenging may not be very important to the SO CCN budget. However, it is important to recall that the SOCRATES data is a small sample of cases that are potentially biased towards cases with less riming. This is due to the experimental setup: sampling took place in the summer, with less ice presence (Danker et al., 2021), and the aircraft actively avoided stratocumulus with large amounts of supercooled liquid drizzle for safety. Thus, further investigation on the importance of rime scavenging seems warranted, especially over the SO during winter when there is more ice and (likely) less liquid water present, and CCN will generally be lower due to a reduction in contributions from biological sources.

The only sink of CCN included in the budget model is coalescence scavenging, which we find reduces the predicted N_d by as much as 90% depending on the precipitation rate (Figure 3.3). This highlights the importance of coalescence scavenging in controlling CCN and N_d. In particular, the results demonstrate that light precipitation with rates < 0.1 mm h^{-1} significantly impacts CCN number. Such light precipitation is commonplace in SO stratocumulus but these rates are not captured well in current CloudSat W-band radar retrievals (Tansey et al., 2022), making it difficult to derive scavenging rates with CloudSat. This further suggests the impact of coalescence scavenging could be larger than the previous estimates based on CloudSat retrievals (I. L. McCoy et al., 2020). In climate models, as well, light precipitation remains poorly (typically over) simulated (e.g., Stephens et al., 2010; Zhou et al., 2021), and is known to have a disproportionately large effect on the aerosols (Wang et al., 2021). How well climate models simulate coalescence scavenging over the SO is an open question, and continued and improved observations of aerosol, cloud and precipitation properties over the SO is needed.

Regarding aerosol sources, we find that overall entrainment of FT CCN plays a larger role than surface sources in controlling N_d during SOCRATES. It should be stressed that SO CCN concentrations are much higher in summer (when SOCRATES was held) associated with increased emissions from ocean biology compared to winter (e.g., Ayers & Gras, 1991). This mostly influences the FT CCN source in the budget model as particles are generated from biological emissions above cloud and brought into the BL where they act as the key CCN source (e.g., Raes, 1995). During SOCRATES, the surface contribution is non-negligible for cases associated with high wind speeds. This could reflect increased production of sea spray particles from wind-driven processes (e.g., Grythe et al., 2014), increased fluxes of biological gases that help to grow already present particles to CCN sizes (e.g., Bates et al., 1998), or even an

increased entrainment of FT Aitken particles to grow into CCN (e.g., Ayers et al., 1997). Budget model overestimation of N_d for these high-wind speed cases was reduced by modifying the surface source parametrization to a more appropriate SO representation. This, as in the global climate model study by Revell et al. (2019), highlights the importance of using a region appropriate parametrization for wind-speed driven surface CCN sources. If this budget model is to be applied widely, a more generalized parameterization may need to be implemented.

Lastly, while the source-sink framework shows skill in capturing observed SO N_d variability, there is still room for improvement. One likely source of remaining error is the parameterization of CCN entrainment into the BL. This is currently based on the large-scale divergence and was set to a fixed value. Variability in entrainment may be responsible for much of the remaining discrepancies between observed and predicted N_d. Likewise, new particle formation and the role of Aitken mode particles in buffering against precipitation removal of N_d and CCN (e.g., I. L. McCoy et al., 2021) is not included in the model. In our view, more detailed examinations of these factors, through large-eddy scale simulations of SOCRATES cases, should be undertaken.

Chapter 4 Untangle Bias in E3SMv2 Simulated Cloud Droplet Number and Aerosols over the Southern Ocean

4.1 Introduction

The Southern Ocean (SO) plays a crucial role in the climate system. The SO is one of the cloudiest places on Earth, with an annual mean cloud fraction of over 80% (Kay et al., 2012; Matus and L'Ecuyer, 2017) and notably ubiquitous low clouds (Grise and Medeiros; 2016; Mace et al., 2020). SO low clouds have an overall cooling effect on the Earth as they reflect sunlight back to space (Wang et al. 2020), and have a large impact on climate sensitivity via both cloud amount and cloud optical depths feedbacks (Zelinka et al., 2020). However, accurately representing SO clouds remains challenging for climate models (Bodas-Salcedo et al., 2014; Hyder et al., 2018; Schuddeboom and McDonald, 2021; Fiddes et al., 2022; Mallet et al. 2023). Moreover, it has been argued that aerosols over the SO, especially those during the austral summer are dominated by natural (nonanthropogenic) aerosols and this region provides a unique natural laboratory to study aerosol-cloud interactions (ACI) and arguably can serve as a modern surrogate for aerosol conditions in the pre-industrial era (Hamilton et al. 2014). Understanding aerosols in the preindustrial era will help us to constrain the radiative forcing from anthropogenic aerosols during the industrial era (Carslaw et al., 2013; Ghan et al., 2013; McCoy et al., 2020).

A key cloud microphysical property that links clouds and aerosols is cloud droplet number concentration (N_d) (Grosvenor et al., 2018). Cloud droplets form on aerosols that can activate and serve as cloud condensation nuclei (CCN). An increase in CCN can lead to an increase in N_d and cloud brightness for a given liquid water path, known as the Twomey effect (Twomey, 1977), resulting in an increase in radiative forcing from ACI (RFaci). Other cloud properties that are important to the cloud radiative effect, such as liquid water path and cloud amount (fraction) also respond to changes in aerosols. These changes are often collectively termed cloud adjustments (Bellouin et al., 2020; Rosenfeld et al., 2023), and the sum of cloud adjustment-induced radiative energy change and RFaci is called effective radiative forcing due to ACI (ERFaci). Previous studies have used the sensitivity of N_d to aerosols to constrain RFaci (e.g. Diamond et al. 2020; Gryspeerdt et al. 2023; Jia and Quaas, 2023; Varble et al., 2023). In particular, McCoy et al. (2020) presented a method to constrain RFaci using a hemispheric contrast of satellite retrieved N_d between the polluted Northern Hemisphere and preindustrial-like SO. However, current climate models appear to systematically underestimate N_d over SO in austral summer (McCoy et al., 2020; Zhou et al. 2021; Atlas et al., 2020; Tang et al., 2023), highlighting the need to understand this model deficiency.

What controls the variability of N_d? In liquid phase clouds, N_d is controlled by the availability of aerosols that can serve as CCN, as well as dynamical factors such as updraft velocities in cloud that affect the supersaturation (impacting on which particles water will condense), and microphysical processes such as collision-coalescence (the merger of cloud droplets) (Wood et al. 2012). Thus N_d variability is closely linked to sources and sinks regulating the CCN budget. The primary CCN sink is coalescence scavenging, where the collision-coalescence of cloud droplets

reduces the available CCN (Feingold et al., 1996; Wood et al., 2012). Kang et al. (2022) demonstrate that coalescence scavenging is a dominant sink for SO CCN and can decrease the predicted N_d by up to 90% depending on the precipitation rate. McCoy et al. (2020) suggest that coalescence scavenging over the SO storm track reduces N_d to 30% of the value it would have without this sink. Aerosols in the pristine summertime SO marine boundary layer (MBL) are primarily sourced from natural origins, including (1) primary sea spray aerosols, consisting largely of sea salt with varying amounts of organics, generated through sea spray and bubble bursting from the ocean surface, and (2) secondary sulfate and organic aerosols, formed from biogenic volatile sulfurous and organic compounds, such as dimethyl sulfide (DMS) (McCoy et al., 2015; Fossum et al., 2018; Revell et al., 2019; Humphries et al., 2023; Sanchez et al., 2021). Sea spray aerosols, which are strongly wind-driven, have a significant impact on SO accumulation and coarse mode aerosols, especially during austral winter (Humphries et al., 2023; Chubb et al., 2016). The overall seasonal cycle of the SO CCN is found to be closely linked to ocean biology-sourced secondary aerosols, with CCN peaking in the biologic-active austral summer and reaching a minimum in winter (Ayers and Gras, 1991; Korhonen et al., 2008; Humphries et al., 2023). In particular, DMS is an abundant natural source of sulfur (Chen et al., 2018), and is found to be closely related to cloud properties (e.g., Charlson et al., 1987; Ayers and Gras, 1991; Korhonen et al., 2008; Mahajan et al., 2015; Hopkins et al., 2023). DMS is produced from the enzymatic cleavage of the precursor dimethylsulfoniopropionate (DMSP), which is a metabolite produced by phytoplankton and bacteria (Hopkins et al., 2023; Teng et al., 2021). After being released from the ocean into the atmosphere, the typical lifetime of DMS is about 1-2 days, and it can be oxidized to form methane sulfonic acid (MSA) and sulfuric acid (H_2SO_4) (Chen et al., 2018; Fung et al., 2022). The oxidation products can further lead to new particle formation, resulting in ultrafine particles (Sihto et al., 2006; Lee et al., 2019; McCoy et al., 2021; Hopkins et al., 2023). Previous studies have shown that new particle formation is frequent in the free troposphere (Clarke, 1993; Clarke et al., 1998; Kerminen et al., 2018; McCoy et al., 2021). Ultrafine Aitken particles from the free troposphere (FT) can be transported into the MBL through subsidence and entrainment, where they further grow and act as CCN (Raes, 1995; Clarke et al., 1998; Korhonen et al., 2008; Kerminen et al., 2018; McCoy et al., 2021). The reservoir of FT Aitken aerosol may act to buffer N_d against precipitation depletion (McCoy et al., 2021; Wyant et al., 2022). Together, the interplay of sources and sinks determines the CCN and N_d variability (Wood et al., 2012).

In the climate models, many processes affect the CCN sources and sinks and predicted N_d. In particular, DMS emissions and chemistry processes are known to be a major source of uncertainty and an active area of research. DMS emissions (ocean-atmosphere flux) are typically estimated using two approaches: (1) a top-down approach that relies on the relationship between DMS and various controlling parameters to estimate seawater DMS, and atmospheric DMS concentration, based on air-sea exchange parameterization (e.g. Galí et al., 2018; Wang et al., 2020; McNabb and Toretell, 2023), (2) a bottom-up approach that mainly relies on the Global Surface Seawater DMS Database (GSSDD) and other ship measurements to compile a global DMS climatology using smoothing and interpolation (Kettle et al., 1999; Lana et al., 2011; Hulswar et al., 2022). Currently, DMS climatology from Lana et al. (2011) (hereafter L11) is widely used in atmospheric chemistry models and climate models (e.g. Chen et al., 2018; Revell et al., 2019). However, some studies have identified the shortcomings of the L11 climatology, such as employing interpolation techniques on the oceanic DMS dataset, which exhibits a right-

skewed distribution of DMS concentrations, as well as having low spatial resolution and biased sampling towards DMS-productive conditions (Galí et al., 2018; Hulswar et al., 2022). The sparse data sampling and high spatial variability in DMS over the SO also result in uncertainty in the estimated DMS emission (Galí et al., 2018; Webb et al., 2019; Bhatti et al., 2023). On top of uncertainty in DMS emissions, the oversimplified DMS oxidation processes in the models are another main source of uncertainty, and the inclusion of more complete sulfate chemistry processes can lead to improvements in simulated N_d and sulfur species (Revell et al., 2019; Chen et al., 2018; Fung et al., 2022; Hopkins et al., 2023; Bian et al., 2024). On the other hand, recent studies also show that the commonly used sea spray aerosol source function overestimates the wind speed dependency over the SO (Revell et al., 2019; Kang et al., 2022). Moreover, previous studies also suggest that the nucleation of new particles and the growth of Aitken particles might be associated with CCN bias (Spracklen et al., 2007; Williamson et al., 2019; Liu and Matsui, 2022). Climate models also struggle to accurately simulate SO precipitation (e.g. Stephens et al., 2010; Zhou et al., 2021; Mülmenstädt et al., 2021), which leads to further uncertainty in the scavenging of CCN.

In this study, a variety of observations were used to evaluate the U.S. Department of Energy (DOE) Energy Exascale Earth System Model version 2 (E3SMv2). E3SM is a contemporary model that includes a regionally refined model (RRM) configuration allowing for the simulation to run at up to 3 km grid spacing (Golaz et al., 2022). The simulations are provided by collaborators Po-Lun Ma and Meng Huang from the Pacific Northwest National Laboratory. The objective is to evaluate the model's performance in simulating N_d, aerosols, and sulfur species, as well as to identify potential avenues for model improvement through observation-informed analysis. This chapter is structured as follows. Section 4.2 describes the observational data, provides an overview of the E3SMv2 model, and outlines the simulation setup. Section 4.3 diagnoses the default E3SMv2's performance in simulating cloud droplet numbers and aerosols. Based on insights gained from Section 4.3, Section 4.4 introduces a series of simulations focused on updating DMS emission and chemistry, investigating their impacts on simulated cloud droplet number and aerosol concentrations. Section 4.5 focuses on the simulated sulfur species. Section 4.6 provides conclusions and discussion.

4.2 Data and Methods

This section describes the observational data and model used in the study. Section 4.2.1 describes the measurements of cloud droplet number concentrations, aerosols, and sulfur species over the Southern Ocean (SO) used in the analysis. Sections 4.2.2 and 4.2.3 briefly describe the E3SMv2 model and simulation setup, respectively.

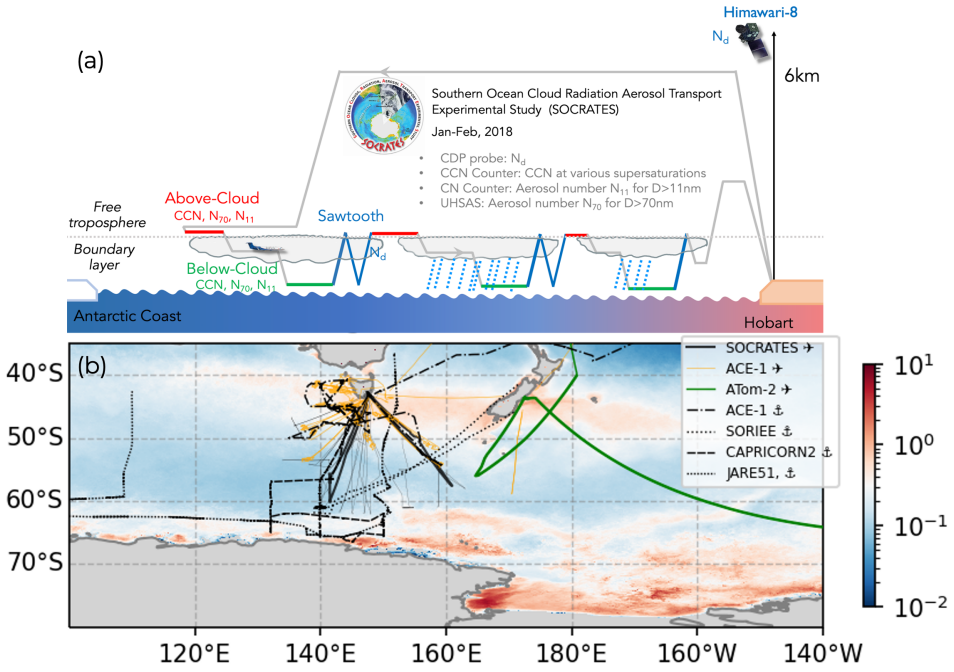

Figure 4.1 (a) A Schematic showing how SOCRATES aircraft measurements are used in the analysis, and (b) a map showing the tracks of all campaigns included in this study. The base map in panel b shows the Aqua MODIS near-surface chlorophyll-a concentration [mg m^{-3}] climatology during February 2003-2023.

4.2.1 Observational data

4.2.1.1 Cloud droplet number and aerosol measurements

For measurements of clouds, aerosols, and precipitation, this study mainly uses aircraft data from the Southern Ocean Cloud Radiation and Aerosol Transport Experimental Study (SOCRATES) (McFarquhar et al., 2021). The SOCRATES campaign occurred in Jan-Feb 2018. During the SOCRATES, the NSF/NCAR HIAPER Gulfstream V research aircraft collected data for clouds, aerosols, and precipitation during 15 flights, using in situ probes and remote sensors during a series of sampling modules, as illustrated in Figure 4.1a. Typically, during each flight, the aircraft took off from Hobart, Tasmania, flew south, descended to the low-cloud deck, and then turned around to fly back. The sampling modules usually consist of above-cloud level legs, below-cloud level legs, and sawtooth legs (where the aircraft ascended/descended through clouds).

This study relies primarily on measurements of cloud droplet number concentration (N_d) obtained during sawtooth legs from the Cloud Droplet Probe (CDP) (Lance et al., 2010). The CDP is an optical spectrometer that measures the size and concentration of cloud droplets by measuring the forward scattered light from droplets as they pass through a lidar beam. The CDP measures the frequency of occurrence of droplets with diameters ranging from 2–50 μm, and these data are used to construct cloud Droplet Size Distributions (DSDs), with units being

number (of droplets) per volume per particle-size (typically #/cm^3/μm). The cloud layer is defined as the region where liquid water content exceeds a threshold of 0.03 g m^{-3} following Wood et al. (2011) and Kang et al. (2021).

This study uses aerosol and CCN concentrations from above-cloud level legs, and below-cloud level legs to evaluate simulations in the free troposphere and boundary layer, respectively. The aerosol and CCN measurements primarily come from four sources: (1) Ultra-high Sensitivity Aerosol Spectrometer (UHSAS, Droplet Measurement Technologies); (2) Condensation Particle Counter (CPC, model TSI-3760A); (3) Cloud Condensation Nuclei Counter measurements (Roberts and Nenes, 2005); and (4) single-particle elemental composition measurements (Twohy et al., 2021). The UHSAS measures the aerosol number concentration and size distribution for particles with diameters ranging from 60-1000 nm (0.06-1.0 μm). This study uses the aerosol number concentration for particles larger than 70 nm (N_{70}) and disregards the data for the 60-70 nm size range due to instrument noise (Sanchez et al., 2021). N_{70} mainly comprises accumulation mode aerosols. The CPC measures the ambient aerosol number concentration with diameters larger than 11 nm (N_{11}), which thus also includes Aitken particles (McCoy et al., 2021). CCN measurements are taken from miniature continuous-flow stream-wise thermal gradient chambers (Roberts and Nenes, 2005), with one chamber operating at constant supersaturation (0.43%) mode and another scanning through supersaturations of 0.06% to 0.87% to produce a CCN spectra every 5 minutes. In addition to aerosol and CCN concentration measurements, this analysis is also supplemented by single-particle elemental composition data (Twohy et al., 2021), which provides the percentage of aerosol number by aerosol particle type (e.g. Sulfur-based, Sea-spray, dust, etc.), determined using Scanning Transmission Electron Microscopy Energy Dispersive X-ray Spectroscopy (STEM/EDS).

For the rain rate, this study uses liquid precipitation retrievals derived from below-cloud level legs where the radar is pointing in the zenith direction based on SOCRATES data with radar reflectivity-velocity retrieval method (Z-V retrieval). More details on the retrieval process and validation can be found in Chapter 2.

In addition to aircraft data, this study uses Himawari-8 satellite-retrieved cloud properties to facilitate the model evaluation. Himawari-8 is a geostationary weather satellite (Bessho et al., 2016). Based on Himawari-8 observations, the NASA SatCORPS group performed cloud properties retrievals for cloud optical depth and effective radius (Smith and Minnis, 2018). By assuming that the cloud layer is adiabatic-like with liquid water content increasing linearly with height within the cloud, one can derive N_d using the retrieved effective radius and optical depth (Grosvenor et al., 2018). More details regarding the calculation of satellite-derived N_d and its evaluation against SOCRATES aircraft data can be found in Kang et al. (2021).

4.2.1.2 Sulfur species measurements

In addition to cloud droplet number and aerosol concentrations, this study also evaluates the E3SMv2 with measured sulfur species including DMS, SO_2, and sulfate aerosols. However, since the SOCRATES campaigns lacked detailed sulfur species measurements, this study thus relies on data from other campaigns over the SO from November to March with a focus on austral summer (December, January, February). The goal of the comparison is to gain insights on

the overall performance of E3SMv2 in austral summer. This study will focus on three sulfur species: DMS, SO_2, and sulfate aerosols based on airborne and shipborne measurements, with the tracks of different campaigns shown in Figure 4.1. Table 4.1-4.3 list the campaigns below and summarize the key information (e.g. time, location, instruments) for DMS, SO_2, and sulfate aerosols, respectively.

This study uses atmospheric DMS measurements from four different campaigns: (1) Atmospheric Tomography Mission 2 (ATom-2); (2) Southern Ocean Iron RElease Experiment (SOIREE); (3) Japanese Antarctic Research 51 (JARE 51); (4) The Southern Hemisphere Marine Aerosol Characterization Experiment (ACE-1). This study also uses SO_2 measurements from ATom-2 and ACE-1, and uses sulfate measurements from ATom-2 and Clouds Aerosols Precipitation Radiation and atmospheric Composition Over the SoutheRN ocean 2 (CAPRICORN2). All the data analyzed in this study was collected from November to March, and only CAPRICORN2 coincided with the SOCRATES timeline.

Table 4.1 DMS measurements over the Southern Ocean used in this study

Field Experiment	Time	Spatial Coverage	Instruments	Reference
Atmospheric Tomography Mission 2 (Atom-2)	Jan-Feb 2017	85°N to 85°S over the Pacific and Atlantic Oceans	the University of California, Irvine Whole Air Sampler (WAS) and the NCAR Trace Organic Gas Analyzer (TOGA) on the NASA DC-8 aircraft	Thompson et al. (2022); Bian et al. (2024)
Southern Ocean Iron RElease Experiment (SOIREE)	February 1999	61°S–41°S	A new automated preconcentration system that takes air samples on the vessel Astrolab	Boyd and Law (2001)
Japanese Antarctic Research 51 (JARE 51)	Dec 2009-Mar 2010	36°N-70°S, 155°E- 23W	Proton transfer reaction-mass spectrometer (PTR-MS) on board the icebreaker Shirase	Koga et al. (2014)
Aerosol Characterization Experiment (ACE-1)	Nov-Dec 1995	55°S–40°S	Gas chromatography/mass spectrometry (GC/MS) with isotopically labeled DMS and SO2 being used as internal standards on board C-130 aircraft	Bates et al. (1998)

Table 4.2 SO_2 measurements over the Southern Ocean used in this study

Field Experiment	Time	Spatial Coverage	Instruments	Reference
Atmospheric Tomography Mission 2 (ATom-2)	Jan-Feb 2017	85°N to 85°S over the Pacific and Atlantic Oceans	the California Institute of Technology Chemical Ionization Mass Spectrometer (CIMS);	Thompson et al. (2022); Bian et al. (2024)

			NOAA Laser Induced Fluorescence (LIF) on the NASA DC-8 aircraft	
Aerosol Characterization Experiment (ACE-1)	Nov-Dec 1995	55°S–40°S	Gas chromatography/mass spectrometry (GC/MS) with isotopically labeled DMS and SO2 being used as internal standards on board C-130 aircraft	Bates et al. (1998)

Table 4.3 Sulfate measurements over the Southern Ocean used in this study

Field Experiment	Time	Spatial Coverage	Instruments	Reference
Atmospheric Tomography Mission 2 (Atom-2)	Jan-Feb 2017	85°N to 85°S over the Pacific and Atlantic Oceans	the University of Colorado Aerodyne high-resolution time-of-flight aerosol mass spectrometer (AMS)	Thompson et al. (2022); Bian et al. (2024)
Clouds Aerosols Precipitation Radiation and atmospheric Composition Over the SoutheRN ocean 2 (CAPRICORN2)	Jan-Feb 2018	40°S-70°S, 130°E-150°E	Time-of-Flight Aerosol Chemical Speciation Monitor (Aerodyne ToF-ACSM, Billerica, MA, USA) on the Australian Research Vessel (RV) Investigator.	McFarquhar et al. (2021); Humphries et al. (2021)

4.2.2 E3SMv2 model description

The Energy Exascale Earth System Model (E3SM) is a state-of-the-art Earth system model. The atmospheric component of E3SMv1 was initially forked from the development Community Atmosphere Model (CAM) model v5.3 with a spectral element dynamical core and physics (Rasch et al., 2019; Xie et al., 2018). Since then, the model has undergone substantial evolution, and the updates from E3SMv1 to E3SMv2 are detailed in Golaz et al. (2022). This subsection only gives a brief overview of E3SMv2, with a focus on the model configurations, and cloud and aerosol processes.

The E3SMv2 has different configurations. The low-resolution configuration uses quasi-uniform 1° horizontal grids and 72 vertical layers (referred to as ne30). The regionally refined model (RRM) configuration (referred to as ne1024) allows for high-resolution simulations (with grid spacing near 3km) over large regions, while keeping the remaining globe at a lower resolution (Tang et al., 2023; Leung et al., 2013). In this study, the E3SMV2 RRM configuration is used with 3 km grid spacing.

The cloud processes in E3SMv2 are documented in Rasch et al. (2019), Xie et al. (2018), and Golaz et al. (2022). The microphysics of stratiform clouds in E3SMv2 use the two-moment MG2 scheme (Gettelman & Morrison, 2015). The Cloud Layers Unified by Binormals (CLUBB) scheme (Golaz et al., 2002; Larson, 2022) handles subgrid turbulent transport and cloud

macrophysics. Deep convection is treated by the Zhang–McFarlane (ZM) deep convection scheme (Zhang and McFarlane, 1995).

In this study, the modal aerosol module with four lognormal size modes (MAM4) is used for E3SMv2's aerosol treatment (Liu et al., 2012, 2016; Wang et al., 2020). MAM4 covers key species including sulfate (SU), sea salt (SS), marine organic aerosol (MOM), secondary organic aerosol (SOA), dust (DU), black carbon (BC), and primary organic matter (POM). The treatment of the physical properties of each species is summarized in Table 1 of Burrows et al. (2022). The four modes consist of Aitken, accumulation, and coarse modes for soluble species, and a primary carbon mode for BC and POM (see Figure 2 in Wang et al. 2020 for a schematic). Each mode presumes aerosols to be internally mixed and each mode is described by a number concentration. MAM4 represents new particle formation through binary H_2SO_4-H_2O homogeneous nucleation (Vehkamäki et al., 2002) and boundary layer nucleation (Sihto et al., 2006). The aerosol activation is treated with the Abdul-Razzak and Ghan (2000) activation scheme. As for the aerosol sinks, the dry deposition is treated based on Zhang et al. (2001), while the wet removal of aerosols considers both in-cloud and below-cloud scavenging (Wang et al., 2020).

4.2.3 Simulation setup and model-observation comparison

This study conducted E3SMv2 3km RRM simulations for February 16-22, 2018, coinciding with the SOCRATES research flights 12 and 13 (RF12 and RF13). During RF12 and RF13, aircraft sampled stratocumulus. Notably, the clouds sampled in RF13 were predominantly liquid, showcasing an intriguing contrast between open and closed cells (Kang et al. 2022). The model had a 1-year spin-up time at 1-degree resolution before the simulation period. During the simulation period, the model was nudged towards MERRA2 reanalysis with a relaxation timescale of 6 hours. The model writes hourly output.

During the evaluation, this study is particularly interested in N_d, CCN as well as aerosol concentration (Section 4.3 and Section 4.4). To compare with aircraft-measured N_d, this study uses the model state variable for droplet number concentration at the top of the cloud layer. To compare with aircraft-measured aerosol concentration for particles with a diameter greater than 70nm (N_{70}) and particles with a diameter greater than 11nm (N_{11}), similar variables were computed by the model.

To compare the model to SOCRATES aircraft data, this study aligns the aircraft observation with the model output in time and space. For each aircraft segment used in the evaluation, the model output is identified within a ±30-minute window of the aircraft's observation time. Using the aircraft's coordinates, the corresponding location is found in the model output. For the measurements in the free troposphere and boundary layer, this study also uses the aircraft's pressure level to find the closest pressure level in the model. Then the model output fields is sampled, such as N_d, within a 1°×1° box to compare with the observation. It is worth noting that the collocation process aims to target the same air mass and stratocumulus fields broadly, rather than achieving for exact alignment in space and time between the aircraft and observation. Achieving the latter would necessitate in-line sampling and model output along the flight track (e.g. Zhou et al. 2021). This feature in E3SMv2 is currently under development. In the evaluation of sulfur species (Section 4.5), this study mainly focuses on comparing the latitudinal and

vertical variations between observations and simulations, as most of the observations do not coincide with SOCRATES in time or space.

4.3 Diagnosing the E3SMv2 default run

How well does E3SMv2 simulate cloud droplet number and aerosol concentration over the Southern Ocean (SO)? This question will be addressed by using SOCRATES observation to diagnose the performance of E3SMv2 during February 16-22, 2018, covering research flights 12 and 13 (RF12 and RF13). Figure 2 compares the probability density function for cloud droplet number and aerosols for the collocated samples between the E3SM model output and the aircraft observations, showing a consistent underestimation in the model.

Figure 4.2a shows that the median value of the E3SM simulated N_d is 58 cm^{-3}, which is significantly lower than the corresponding observed median N_d of 112 cm^{-3} by about a factor of 2. The underestimation in simulated N_d is not just the case when compared to the aircraft data, but also true when compared to the Himawari-8 satellite-derived N_d (Figure 4.3). The underestimation of N_d here in E3SMv2 RRM 3km run aligns with the diagnosis results of 1 degree E3SMv2 in Tang et al. (2023), implying a bias source independent of model resolution. The underestimation of N_d is not a unique problem for E3SM, as previous studies show that climate models systematically underestimate N_d over SO in the austral summer (McCoy et al., 2020; Zhou et al. 2021; Atlas et al., 2020).

The underestimation of the N_d is consistent with the underestimation of the CCN and aerosols in both the boundary layer (Figure 4.2 b,c,d) and free troposphere (Figure 4.2 e,f,g). In the boundary layer, E3SMv2 simulated CCN at 0.3% supersaturation ($CCN_{0.3}$) and N_{70} show an underestimation of about 40% compared to the observed values, while the simulated N_{11} is underestimated by about 28%. Compared to the boundary layer, the underestimation in the free troposphere is much more substantial, with simulated $CCN_{0.3}$, N_{70}, and N_{11} lower than the observed values by about 70%.

Why does the model underestimate N_d and aerosol concentrations? This question can be reasoned from a source-sink framework: either the model has insufficient sources or/and overly strong sinks. The model consistently underestimates aerosols and CCN in both the boundary layer and free troposphere, suggesting the model is likely to have insufficient aerosol sources. The aerosol sink in the MAM4 is dominated by wet removal (Liu et al., 2016), including in-cloud and below-cloud scavenging (Wang et al., 2020). Figure 4.4 attempted to assess the below-cloud scavenging by partitioning the N_{70} based on rain rate (column maximum) for the below-cloud observations from RF13 and for the model in the selected region (depicted in Figure 4.3b). The observed N_{70} shows two distinctive modes of PDF (median of 43 vs 202 cm^{-3}) associated with precipitating clouds (rain rate > 0.01 mm hr^{-1}) and non-precipitating clouds (rain rate < 0.001 mm hr^{-1}), while the difference in the E3SMv2 is less pronounced (median of 123 vs 141 cm^{-3}), suggesting the model might have insufficient wet deposition for this case study. Using ARM Eastern North Atlantic (ENA) site observations, Christensen et al. (2023) also pointed out that the E3SMv1 has insufficient CCN concentration loss by precipitation. More discussion on the sink will be presented in Section 4.6, but for now this study will focus on the aerosol sources.

Since the model's underestimation of N_d and aerosols is likely due to insufficient aerosol sources, the next step is to identify the major contributing aerosols. What is the main composition of aerosols for RF12 and RF13? According to the SOCRATES single particle composition data from RF12 and RF13, Twohy et al. (2021) find that sea spray aerosol dominates larger aerosol particles with a dry diameter of about 500nm (0.5um). However, for smaller aerosol particles (with a dry diameter of 100~500nm), about 79% ~ 83% of particles are sulfur-based in the boundary layer, and 98.6% of particles are sulfur-based in the free troposphere. The dominance of sulfur-based particles is not only limited to these two flights but is also the case for the other SOCRATES flights. Sulfate aerosols over the remote SO are formed mainly through the oxidation of DMS, leading to new particle formation (e.g., Chen et al., 2018; Fung et al., 2022; McCoy et al., 2021; Hopkins et al., 2023). Given the importance of sulfur chemistry over the SO in the summer, the representation of sulfur chemistry would be key to reasonably simulating aerosols and N_d.

Figure 4.5 shows a schematic illustrating the E3SMv2's treatment of relevant processes. In particular, the current treatment of DMS-related processes in the E3SMv2 is rather simple (Emmons et al., 2010). The remaining section describes the default DMS emission and chemistry and following section introduces model updates build upon default E3SMv2 in a series of experiments.

In the default E3SMv2, the DMS emission is prescribed as a monthly sea-air flux climatology(Wang et al., 2018). Figure 4.6a shows the E3SM default DMS flux in February. Figures 4.6b and c also show the DMS flux in February from two other climatologies derived based on the bottom-up approach: Lana et al. (2011) (hereafter L11) and Hulswar et al. (2022) (hereafter H22). It is clear that the default DMS emission prescribed in E3SMv2 shows a different pattern compared to L11 and H22, and features lower DMS emission over SO high latitudes.

DMS-related chemical reactions represented in the default E3SMv2 are listed below:

$$DMS + OH \rightarrow SO_2 \text{ (R1)}$$

$$DMS + OH \rightarrow 0.5SO_2 + 0.5HO_2 \text{ (R2)}$$

$$DMS + NO_3 \rightarrow SO_2 + HNO_3 \text{ (R3)}$$

$$SO_2 + OH \rightarrow H_2SO_4 \text{ (R4)}$$

The abstraction pathway includes the DMS + OH reaction (R1) and the DMS + NO_3 reaction (R3), while the addition pathway involves the DMS + OH reaction (R2). Note that R2 does not conserve sulfur. SO_2 can be further oxidized by OH to form sulfuric acid (R4). E3SMv2 uses the reaction rates from Emmons et al. (2010) for these reactions. In the default E3SMv2, oxidants like OH and NO_3 are prescribed and derived from a 2-degree CAM-MOZART simulation conducted over a decade ago (Lamarque et al., 2010). Sulfate can be formed by SO_2 aqueous oxidation (Tie et al, 2001) and H_2SO_4 (gas) uptake (Seinfeld and Pandis, 1998).

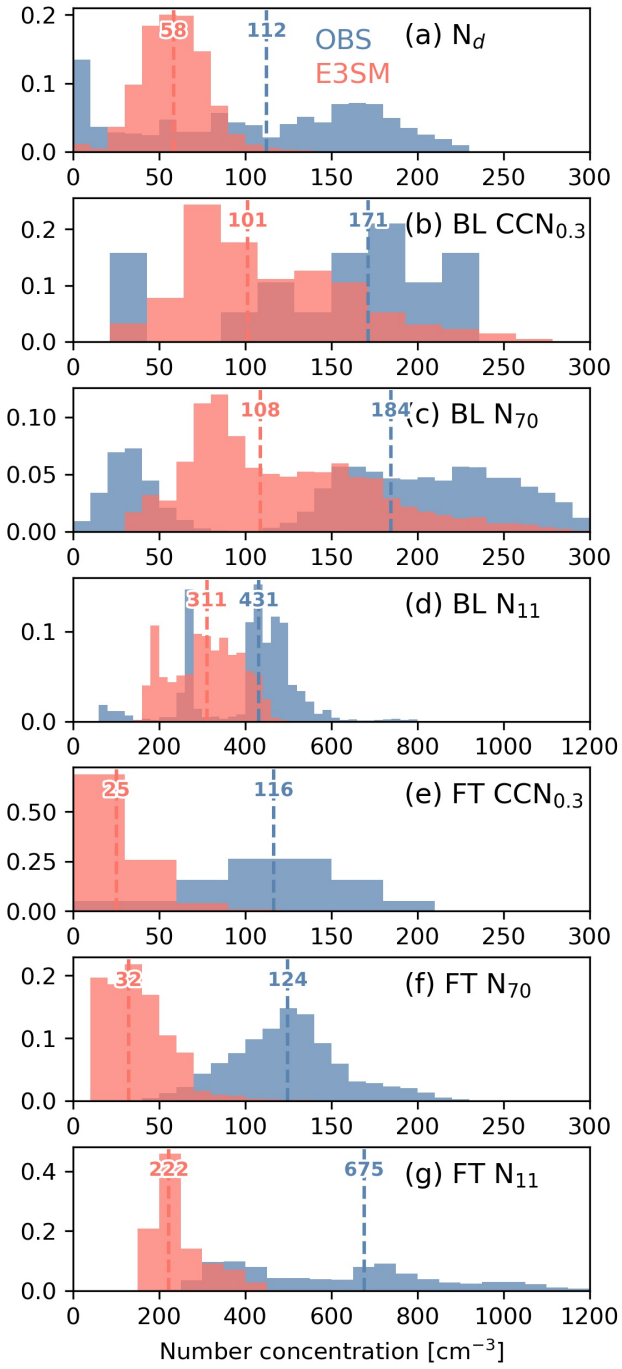

Figure 4.2 The comparison of the probability density function for the E3SMv2 (red) Regionally Refined Mesh, RRM, and SOCRATES aircraft observation (blue) for collocated samples during February 16-22, 2018: (a) cloud droplet number concentration (N_d), (b-d) boundary layer CCN at 0.3% supersaturation ($CCN_{0.3}$), aerosol number concentration for particles larger than 70nm(N_{70}), and aerosol number concentration with diameters larger than 11 nm (N_{11}), (e-g) free troposphere $CCN_{0.3}$, N_{70}, and N_{11}. The dashed vertical lines represent the median values.

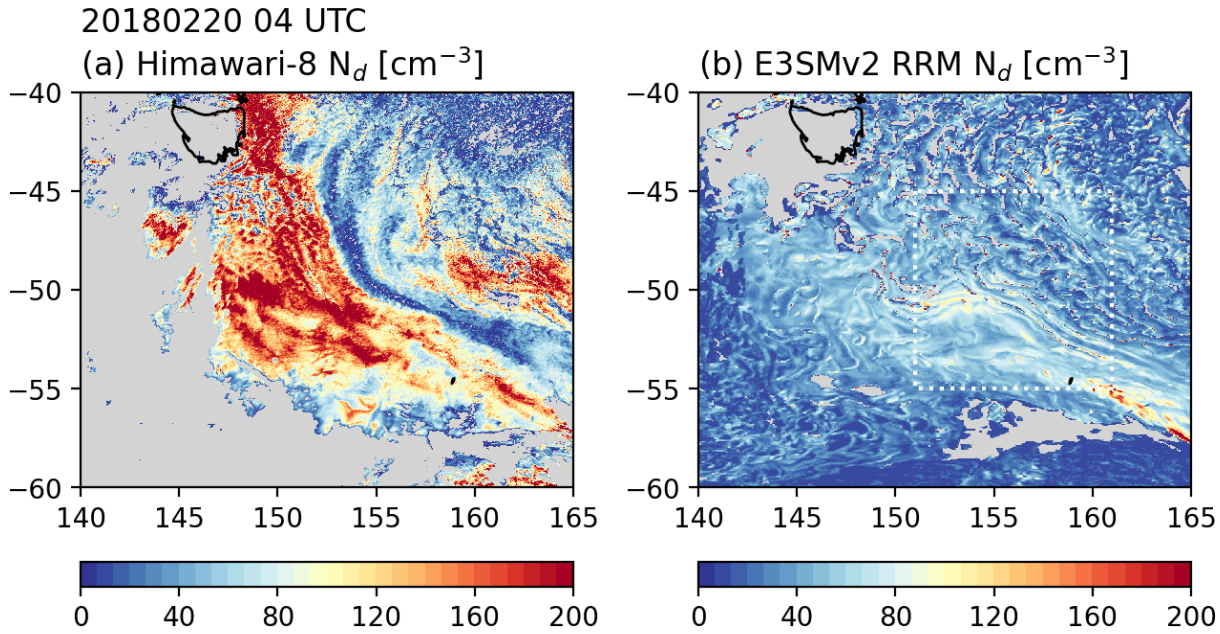

Figure 4.3 (a) Satellite retrieved N_d from Himawari-8, and (b) E3SM 3km RRM simulated N_d on Feb 20, 2018 at 04 UTC. The dashed line in the panel b shows selected region used in Figure 4.4.

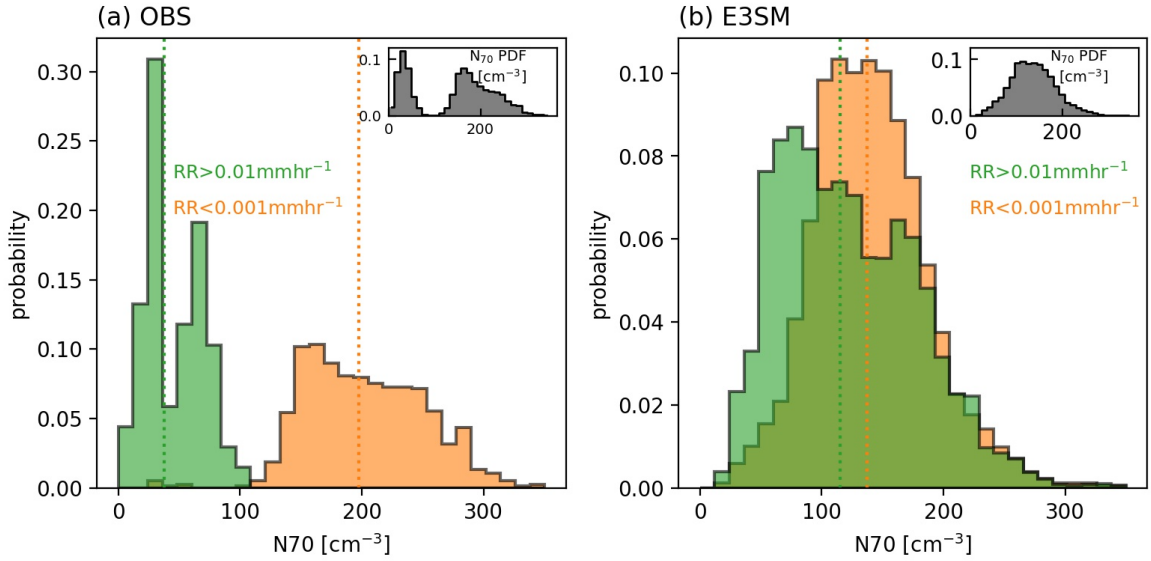

Figure 4.4 The comparison of the probability density function(PDF) N_{70} portioned based on rain rate for (a) observations from below-cloud measurements during RF13 and (b) for the E3SM in the selected region (depicted in Figure 4.3). Orange shows the PDF of N_{70} associated with non-precipitating clouds (rain rate or RR < 0.001 mm hr^{-1}), while green shows the PDF of N_{70} associated with precipitating clouds (rain rate or RR > 0.01 mm hr^{-1}). The embedded figures in panels a and b show the PDF of N_{70} without the portioning.

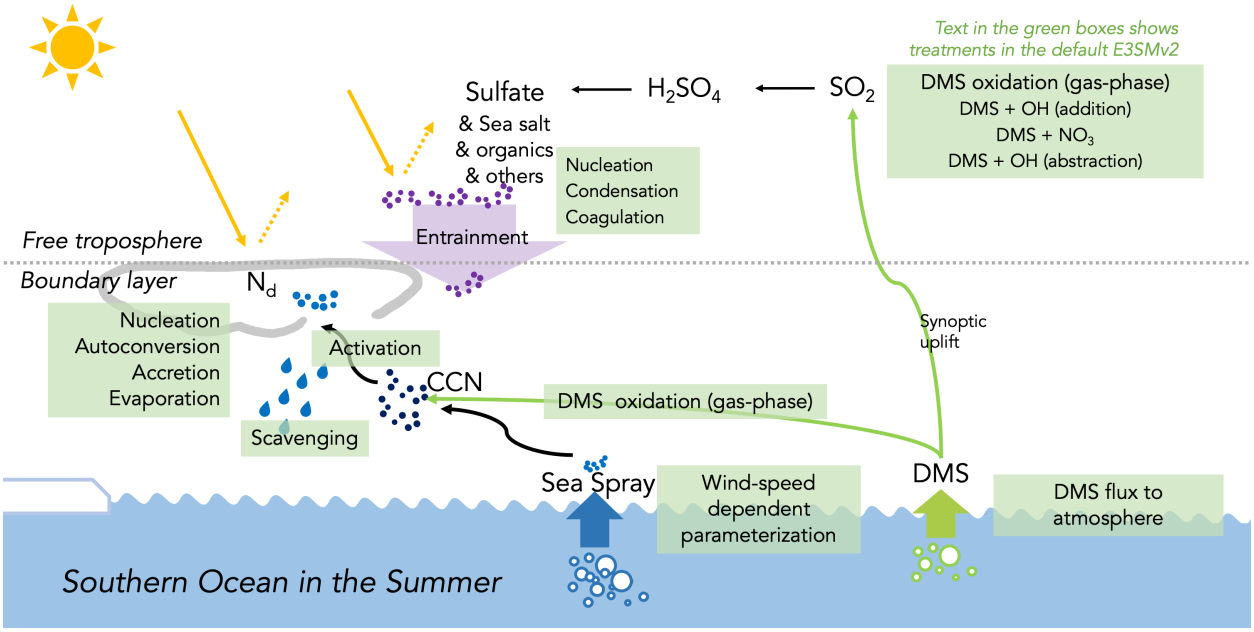

Figure 4.5 Schematic for the E3SMv2's treatment of relevant processes

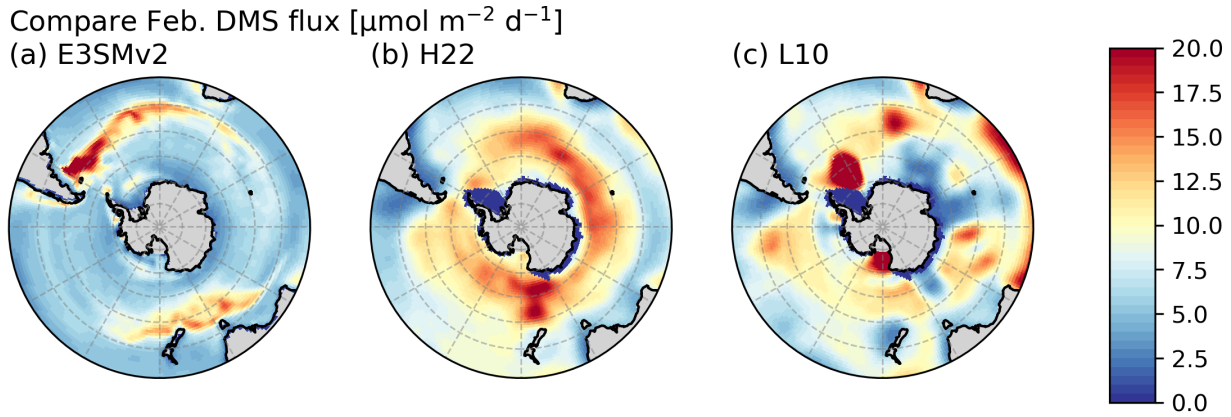

Figure 4.6 DMS flux climatology in February: (a) current DMS flux prescribed in E3SMv2; (b) Hulswar et al. (2022) climatology (H22) ;(c) Lana et al. (2011) climatology (L11). The units of DMS flux is µmol m^{-2} d^{-1}.

4.4 Impact of DMS emission and chemistry update on simulated cloud droplet number and aerosols

To untangle the E3SMv2's bias in simulating N_d and Aerosols over SO, a series of simulations are designed (as shown in Table 4.4): (1) the first group of simulations focuses on updating the DMS emission and chemistry in the default E3SMv2, and (2) the second group of simulations are sensitivity studies built on the insights from the first group of runs.

In the first group of simulations, seven runs introduce incremental changes on the previous run, with details listed in Table 4.4. Here is a brief overview of the experiments. Based on the baseline run (run_B), run_0 removed the minimum N_d limiter in the model and also fixed a bug in aqueous phase chemistry for sulfate production in the liquid clouds. In the next simulation (run_1), the default DMS emission flux (Figure 4.6a) was further replaced with H22 DMS emission flux (Figure 4.6b). The following simulations ($run_{2\text{-}5}$) mainly focused on: (a) updating the reaction rates using the rates from Burkholder et al. (2015) following Chen et al. (2018), instead of rates from Emmons et al. (2010); (b) updating the oxidants file using the new CAM-Chem results; (c) adding DMS + O3 gas phase chemistry:

$$DMS + O_3 \rightarrow SO_2 \text{ (R5)}$$

As noted in Section 4.3, the current DMS + OH addition reaction (R2) does not conserve sulfur. An additional test is performed in run_6 by updating R2 to conserve sulfur as:

$$DMS + OH \rightarrow 0.75SO_2 + 0.25H_2SO_4 \text{ (R2-test)}$$

The reaction (R2-test) is similar to the reaction in standard GEOS-Chem: DMS + OH → $0.75SO_2$ + 0.25MSA (Chen et al. 2018). However, E3SMv2 currently does not treat MSA. To compensate for the absence of MSA, H_2SO_4 was used instead to test the model sensitivity. After each run, a similar analysis is repeated as the baseline run of default E3SMv2 and with results summarized in Figure 4.7.

Figure 4.7 presents the violin plots for aircraft observed and E3SMv2 RRM simulated cloud droplet number (N_d), cloud condensation nuclei at 0.3% supersaturation ($CCN_{0.3}$), aerosol concentration with D>70nm (N_{70}), and aerosol concentration with D>11nm (N_{11}) in runs for collocated samples. Note that panels b, c, and d depict results for $CCN_{0.3}$, N_{70}, and N_{11} in both the boundary layer (green) and the free troposphere(orange).

Overall, Figure 4.7a shows that updating DMS emission and chemistry results in a closer alignment between observed N_d (median of 112 cm^{-3}) and the simulated N_d, which increases from a median of 58cm^{-3} in run_B to 77cm^{-3} in run_5, and to 91cm^{-3} in run_6. Figure 4.7 b-d shows a closer agreement in the boundary layer (green) between the simulated and $CCN_{0.3}$, N_{70}, and N_{11} up to run 5. The overall values and changes of $CCN_{0.3}$ and N_{70} are quite similar, mostly because of a strong equivalence of CCN concentration at 0.3% supersaturation and the UHSAS concentration above 70 nm diameter, as discussed in Sanchez et al. (2021). Interestingly, in the free troposphere (orange), simulated $CCN_{0.3}$, $N_{70,}$ and N_{11} display a persistent low bias compared to the observation through run 5. The relative underestimation of $CCN_{0.3}$ and N_{70} is greater than that of N_{11} (which is N_{70} with additional Aitken particles) in the free troposphere, suggesting that the model might have insufficient growth of Aitken particles.

Examining some of the differences in the sensitivity test:

From run_5 to run_6, the reaction (R2) is replaced with (R2-test) for the DMS+OH addition reaction to conserve sulfur. The most significant change can be seen in the N_{11} in both the free troposphere and boundary layer. The enhanced SO_2 and H_2SO_4 produced in reaction (R2-test)

leads to enhanced nucleation, resulting in an unrealistically high N_{11}. In particular, the current boundary layer nucleation treatment in the MAM4 scheme is based on Sihto et al. (2006), where the boundary layer nucleation rate is a simple empirical fit: $J = A [H_2SO_4]$, where $[H_2SO_4]$ is the sulphuric acid concentration, and A is a first-order rate coefficient of 10^{-6} s^{-1} as in Wang and Penner (2009). The newly formed particles are added to the Aitken mode in MAM4 (rather than having a separate nucleation mode). An additional sensitivity test was conducted in the run_7 by turning off the nucleation in the boundary layer, with boundary layer height computed based on Holtslag and Boville (1993). As expected, there is a reduction in the boundary layer N_{11} compared to run_6. This test highlights that it is not only the gas phase chemistry that affects the evaluation using N_{11} (and indeed other observables used here). Accordingly, while additional development of gas phase chemistry is needed in E3SM (if aerosol and ACI are going to be modeled correctly over the SO) but treatment of aerosol processes related to nucleation and coagulation also likely needs to be examined further.

From run 0 to run 1, the default DMS emission flux (Figure 4.6a) is replaced with H22 DMS emission (Figure 4.6b), which leads to an increase in N_d, CCN, N70 as well as N_{11}. What if the model uses L11 emission (Figure 4.6c) instead? An additional sensitivity test run_8 was done based on run_6, by using L11 instead of H22 as DMS emission, while keeping other settings the same. Overall, there is not much difference between the two runs (run_6 vs run_8). Emphasizing that while emissions do need to be improved, more attention needs to be given to the model's chemistry processes.

Table 4.4 Model runs

Group	Simulations	Details
Baseline	run_B	Default E3SMv2
Updating DMS chemistry and emission	run_0	Default E3SMv2 but (a) without the minimum Nd limiter and (b) a bug fixed in aqueous phase chemistry for sulfate production in the liquid clouds
	run_1	Based on run_0, update the DMS emission with the H22
	run_2	Based on run1, update the DMS+OH (addition) reaction rate
	run_3	Based on run2, update the oxidant file with the new CAM-Chem results
	run_4	Based on run3, update DMS + NO3 reaction rate
	run_5	Based on run4, add DMS + O3 mechanism
	run_6	Based on run5, update DMS + OH addition reaction
Sensitivity tests	run_7	Based on run6, turn off PBL nucleation
	run_8	Based on run6, use L11 DMS emission

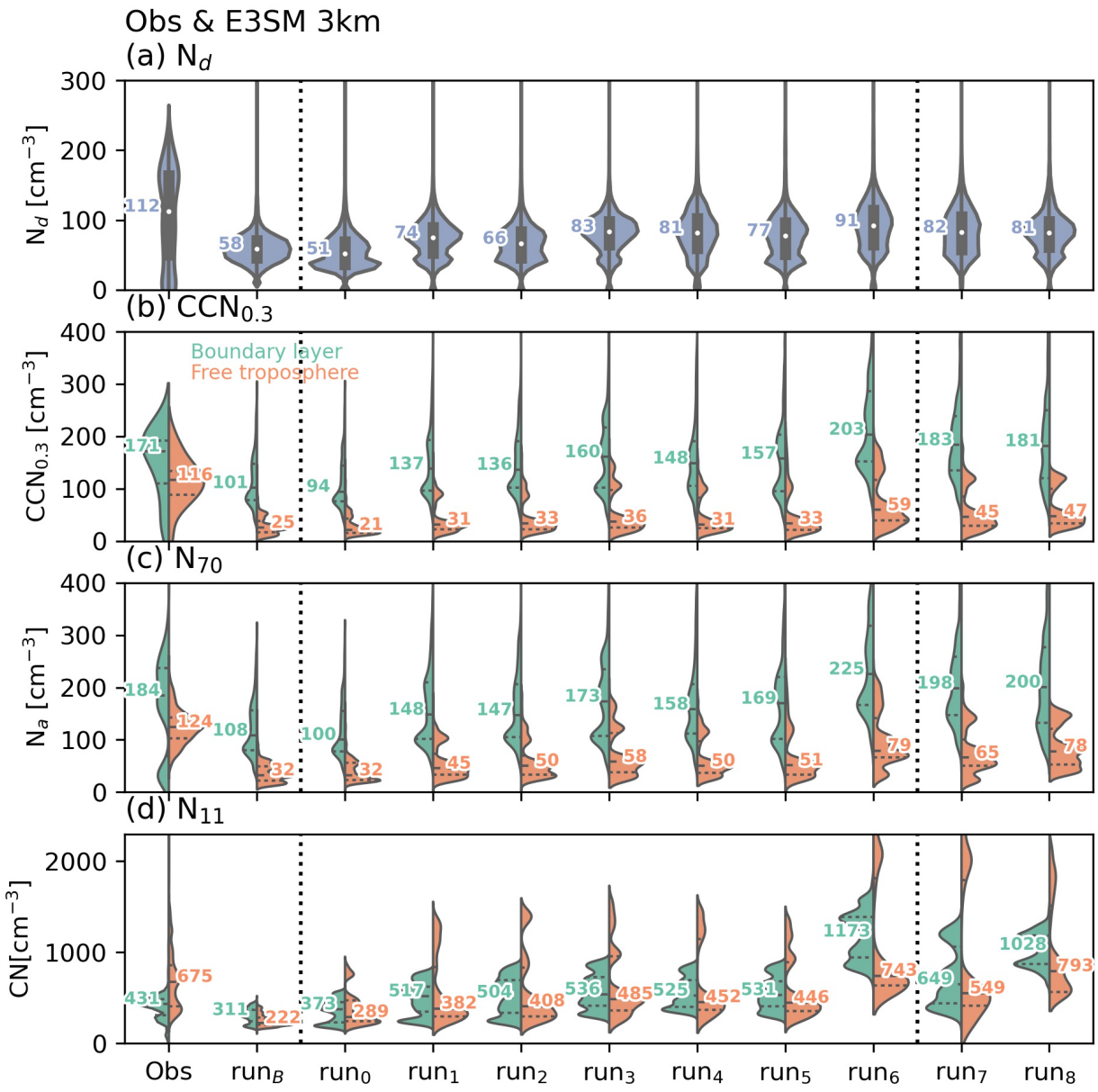

Figure 4.7 Violin plots for aircraft observed and E3SMv2 simulated (a) cloud droplet number concentration (N_d), (b) CCN at 0.3% supersaturation($CCN_{0.3}$), (c) aerosol number concentration for particles larger than 70nm(N_{70}), and (d) aerosol number concentration with diameters larger than 11 nm (N_{11}). Panels b,c, and d depict results in both the boundary layer (green) and the free troposphere(orange). The values alongside the violins are the median values.

4.5 Evaluate the simulated sulfur species

This section will explore the impacts of DMS emission and chemistry updates on the sulfur species (DMS, SO_2, and sulfate), and compare the simulation with observations. Since SOCRATES lacks detailed sulfur species measurements, this study will rely on several other

campaigns over the SO as listed in Section 4.2.1 and depicted in Figure 4.1b. Note that most of the data are not from the same time as SOCRATES, except for CAPRICORN2. The goal of the comparison is to gain some insights into the overall performance of E3SMv2 in the austral summer.

Figure 4.8a displays the comparison between observed and simulated DMS plotted as a 2D map, as well as plotted against latitude (Figure 4.8b) and pressure (Figure 4.8c). Figure 4.8a represents the simulated DMS at surface level in run_6, after implementing updates in DMS emission and chemistry. Generally, the simulated DMS has lower values north of 55°S than south of 55°S. When comparing the simulated DMS with ship-measured DMS (colored dots) from the ACE-1, SORIEE, and JARE51 campaigns, there is overall agreement north of 55°S, but an overestimation in simulated DMS south of 55°S. This overestimation is also apparent in Figure 4.8b when DMS is plotted as a function of latitude. If L11 DMS emission (green) was used instead, the overestimation would be less pronounced compared to the run with H22 DMS emission (orange), but the high bias still exists. This suggests that the discrepancy is likely because the model lacks DMS oxidation processes important at higher latitudes, such as BrO (Chen et al., 2018). Nonetheless, a closer agreement with the observations can also be seen in the simulated DMS vertical profile when comparing run_6 and run_8 with the default E3SMv2 run_B (Figure 4.8c). This suggests that the model updates improved not only the simulated N_d and aerosols (as shown in Section 4.4) but also the simulated DMS. The overall reduction of DMS vertically is consistent with the vertical profiles of SO_2 in Figure 4.9c, where the updates lead to higher SO_2 in run_6 and run_8 compared to run_B.

However, one might draw different conclusions on how far the model still is from the observations, depending on which observations to compare against, because the observed DMS values from the ACE-1 campaign and ATom-2 campaign differ significantly. ATom-2 observed DMS < 50 pptv over the SO and much lower than that from the ACE-1 campaign. On the other hand, the observed SO_2 values (Figure 4.9b) from ATom-2 are higher than the values from ACE-1, and the simulated SO_2 in run_6 and run_8 falls in the 25th and 75th percentile from ATom-2. It is possible that due to the high spatial variability of DMS, ATom-2 sampled airmass with lower DMS concentrations compared to ACE-1. And as shown in Figure 4.8b, it is not uncommon to have ship-observed DMS values greater than 100 pptv.

In addition to DMS and SO_2, the simulated sulfate mass concentration is also compared with the observed sulfate mass concentration. To make the comparison consistent, it is important to consider the size range of the simulated and observed sulfate mass concentrations. Two sulfate observation datasets are used to compare with the model (Table 4.3): (1) CAPRICORN2's sulfate mass concentration data collected by the Time-of-Flight Aerosol Chemical Speciation Monitor (Aerodyne ToF-ACSM, Billerica, MA, USA); (2) Atom-2's sulfate mass concentration data collected by the University of Colorado Aerodyne high-resolution time-of-flight aerosol mass spectrometer (AMS). Both instruments provide the sulfate mass concentration for particles with a diameter less than 1μm (1000 nm), and the particle transmission drops off below 100 nm (Fröhlich et al., 2013; Liu et al., 2007). To compare with the observation, this study uses the sulfate mass in the accumulation mode D in 80nm-1μm.

Figure 4.10 compares the simulated and observed sulfate mass concentrations, revealing a consistent overestimation in the model across all simulations. When compared to CAPRICORN2 measurements during the simulation period (Figure 4.10b), the default run_B simulated sulfate mass concentrations that are over three times larger than the observations, despite underestimations in N_d and aerosol number concentrations (Figure 4.7). Updates to DMS emission and chemistry have led to further overestimations in sulfate mass concentrations (Figure 4.10b and Figure 4.10c). Like other species, these results need to be interpreted in the source-sink framework. Is the overestimation in the simulated sulfate mass concentration due to the source being too strong, the sink being too weak, or both? In the MAM aerosol scheme used by E3SM, the main sources of sulfate are aqueous-phase SO_2 oxidation and H_2SO_4 condensation on pre-existing aerosols, while the main sink is wet removal. The overestimation of sulfate mass concentration is a common problem in many regional and global models (e.g. Gao et al., 2022). Past studies have shown that updating the wet removal scheme can greatly reduce the overestimations in the simulated sulfate mass concentrations (Gao et al., 2022; Ge et al., 2022). As shown in Figure 4.4, N_{70} portioned by the rain rate suggested the model might have insufficient below-cloud scavenging and further work is needed to examine the wet removal of aerosols in the model.

With the data presented, this study concludes that updating the DMS emission and chemistry has improved the alignment between the simulated and observed DMS. Further model development is still needed, particularly to address the overestimation of DMS at high latitudes, which might also help to further improve the simulated cloud droplet number and aerosol concentrations. Moreover, further work is needed to address the overestimation of sulfate mass concentration in the model.

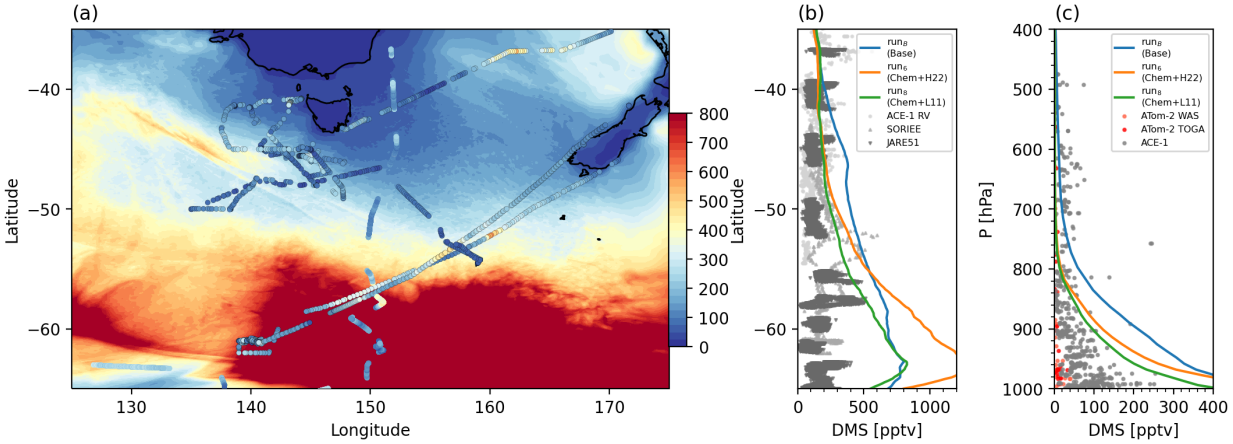

Figure 4.8 Comparison between observed and simulated DMS plotted as (a) DMS field (run_6) at the surface level, (b) surface level DMS as a function of latitude (run_B, run_6, run_8), and (c) DMS as a function of pressure (run_B, run_6, run_8). In panel (a), the colored dots are the ship-measured DMS from ACE-1, SORIEE, and JARE51 campaigns. The ship-observed DMS values are also plotted in panel b. In panel c, the aircraft-observed DMS values are also plotted: ATom-2 campaign's measurements using WAS in light pink or TOGA in red; ACE-1 campaign's measurements in grey. The tracks for each campaign are presented in Figure 4.1 and summarized in Section 4.2.

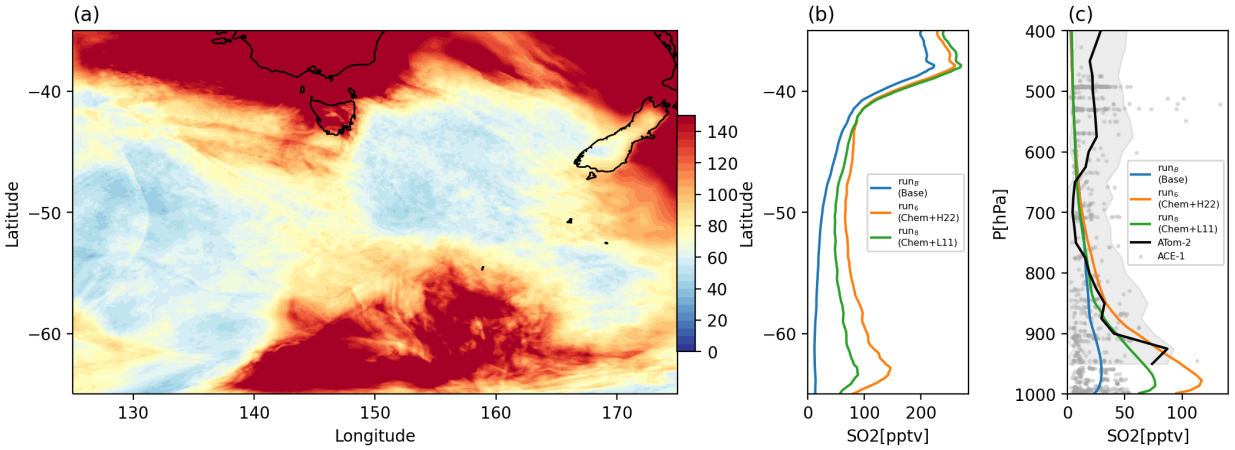

Figure 4.9 Comparison between observed and simulated SO_2 plotted as (a) SO_2 field (run_6) at the surface level, (b) surface level SO_2 as a function of latitude (run_B, run_6, run_8), and (c) SO_2 as a function of pressure (run_B, run_6, run_8). In panel c, the aircraft-observed SO_2 values are also plotted: ATom-2 campaign's measurements in the area south of 40°S and west of 140°W are binned vertically with average values shown in black, with the 25th-75th percentile shown as grey shading; ACE-1 campaign's measurements are shown in grey. The tracks for each campaign are presented in Figure 4.1 and summarized in Section 4.2.

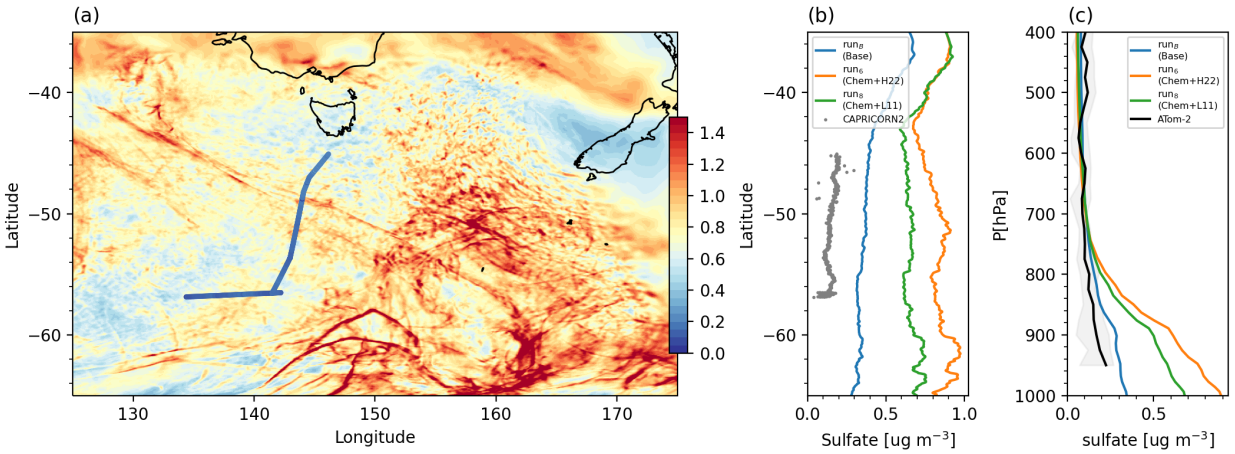

Figure 4.10 Comparison between observed and simulated sulfate mass concentration plotted as (a) sulfate field (run_6) at the surface level, (b) surface level sulfate as a function of latitude (run_B, run_6, run_8), sulfate (c) sulfate as a function of pressure (run_B, run_6, run_8). In panel (a), the colored dots are the ship-measured sulfate mass concentration from CAPRICORN2 for the simulation period. The CAPRICORN2's sulfate observations are also plotted in panel b. In panel c, the aircraft-measured sulfate mass concentration from ATom-2 is also plotted. ATom-2 campaign's measurements in the area south of 40°S and west of 140°W are binned vertically with median values shown in black, with the 25th-75th percentile shown as grey shading. The tracks for each campaign are presented in Figure 4.1 and summarized in Section 4.2.

4.6 Conclusions and Discussion

In this study, a variety of observations were used to evaluate E3SMv2 in simulating N_d, aerosols, and sulfur species through observation-informed analysis. This study conducted 3km-resolution RRM simulations for February 16-22, 2018, coinciding with the SOCRATES research flights 12 and 13 (RF12 and RF13).

This analysis shows that the default E3SMv2 underestimates the cloud droplet number (N_d) by a factor of 2 compared to SOCRATES aircraft observations. This underestimation of N_d over SO in the austral summer is not just a unique issue for E3SMv2, but is a common issue for other climate models (McCoy et al., 2020; 2021; Zhou et al. 2021; Atlas et al., 2020). Further analysis indicates that the E3SMv2 model consistently underpredicts the cloud condensation nuclei (CCN) and aerosol concentrations for particles larger than 70nm (N_{70}) and 11nm(N_{11}) in both the boundary layer and the free troposphere, implying an insufficient aerosol source in the model. By updating the DMS emission and chemistry in the default E3SMv2 through a series of experiments, the results show that these updates improved the model's agreement with the observed N_d and boundary layer aerosols. Moreover, the updates led to a decrease in DMS, an increase in SO_2 vertically, and improved the model's overall agreement between the simulated and observed DMS vertical profiles.

However, the comparison of observed and simulated DMS, SO_2, and sulfate underscores the need for further model development to enhance DMS-related processes in the E3SM. For instance, the model overestimates DMS in high latitudes, possibly due to missing oxidation pathways. Currently, the model lacks aqueous phase reactions, and species such as MSA, BrO, and HPMTF, which have been found crucial for DMS chemistry (Revell et al., 2019; Chen et al., 2018; Fung et al., 2022). Additionally, model development is needed to implement a coupling of DMS fluxes with winds and the sea-water concentration, rather than using a prescribed DMS flux climatology. Again, improvements in DMS emission and chemistry are not just needed for E3SM, but also for other climate models. A recent evaluation study by Bian et al. (2024) shows that five AeroCom-III models (including E3SM), struggle to accurately simulate sulfur-containing species (DMS, SO_2, MSA, sulfate), with differences among model results that can exceed an order of magnitude. This is crucial not only for simulating the sulfur cycle, but also for the clouds, and radiative forcing (McCoy et al., 2020; Carslaw et al., 2013).

In addition to DMS chemistry, this analysis suggests that future work is needed to address aerosol biases in the free troposphere. Despite improvements in boundary layer aerosol concentration, low biases in free troposphere aerosols persist compared to the observation, which is likely due to insufficient growth of Aitken particles, a bias noted in other studies (Spracklen et al., 2007; Williamson et al., 2019; Liu and Matsui, 2022). Furthermore, this study suggests that the model's below-cloud scavenging is likely too weak compared to the observation and is unable to capture the two distinctive modes of N_{70} distribution associated with precipitating and non-precipitating clouds shown in the observation. This result is broadly similar to the finding of Christensen et al. (2023) which show E3SMv1 has insufficient CCN concentration loss by precipitation based on ARM Eastern North Atlantic site observations. The overestimation in simulated sulfate mass concentration could also be related to insufficient wet deposition, as suggested by previous studies (e.g., Ge et al. 2022). Given the disproportionate control of aerosol

burden by light rain (Wang et al., 2021) and the prevalence of light rain over the SO (Siems et al., 2022; Tansey et al., 2022; Kang et al., 2024), further assessment of the models' wet removal processes is needed.

Regarding observations, to further our understanding of sulfate chemistry over the SO and facilitate model diagnosis and development, more measurements of sulfur species and oxidants would be desirable, preferably alongside observations of aerosols, clouds, and precipitation. One of the challenges encountered in this study is data scarcity over the SO, especially the sulfur species measurements (DMS, SO_2, sulfate). The different results shown by the observations add a further layer of complexity during the model diagnosis. For example, the results show that one would draw different conclusions on how far the model still is from the observations, depending on which observations to compare against, since DMS values over the SO from the ATom-2 campaign are generally lower than that from the ACE-1 campaign and other shipborne campaigns. In general, DMS observations are usually taken as the ground truth to evaluate the model performance in simulating DMS emission and chemistry (e.g., Fung et al., 2022; Bian et al., 2024; Zhao et al., 2024) and given the large variability of the DMS over the SO (e.g., Webb et al., 2019), more DMS measurements seem key for the model diagnosis. Other measurements would be helpful including aerosol composition for aerosol speciation, and aerosol size distribution data for particles with sizes in 10-1000 nm to constrain the Aitken particle size distribution. With more field campaigns taking place and planned over the SO (e.g. Mallet et al., 2023), there are also great opportunities to address the model biases and improve model representation.

Chapter 5 Summary

The overarching objective of this dissertation is to characterize precipitation from the Southern Ocean (SO) summertime stratocumulus using aircraft observations collected during the Southern Ocean Clouds Radiation Aerosol Transport Experimental Study (SOCRATES), and study sources and sinks of SO cloud droplet number and aerosol concentrations using both a simple source-sink budget model and high-resolution Energy Exascale Earth System Model (E3SM) simulations.

In Chapter 2, data from airborne radar, lidar, and in situ probes were used to characterize precipitation properties. For the cold-topped clouds (cloud-top-temperature < 0°C), the phase of precipitation with reflectivity > 0 dBZ is predominantly ice, while reflectivity < –10 dBZ is predominantly liquid. Liquid-phase precipitation properties are retrieved where radar and lidar are zenith-pointing. Power-law relationships between reflectivity (Z) and rain rate (R) are developed, and the derived Z-R relationships show vertical dependence and sensitivity to the presence of droplets with diameters between 10-40 μm. Using derived Z-R relationships, a reflectivity-velocity (ZV) retrieval method, and a radar-lidar retrieval method, rain rate and other precipitation properties were derived. The retrieved rain rate from all three methods shows good agreement with in-situ aircraft estimates, with rain rates typically being quite light (<0.1 mm hr^{-1}). The derived data were further used to study the vertical distribution of precipitation properties. The rain rate, precipitation number concentration, and precipitation liquid water all decrease as one gets closer to the surface, while precipitation size and distribution width increases. The relationships were examined for cloud base rain rate (R_{CB}), cloud depth (H) and aerosol concentration (N_a) for particles with a diameter greater than 70nm, and shows that R_{CB} is proportional to $H^{3.1}\ N_a^{-0.8}$.

In Chapter 3, a simple source-and-sink budget model was constrained by aircraft observations and was used to test model behavior and examine the relative influence of processes that determine cloud droplet number (N_d) in SO stratocumulus clouds. The sources include free tropospheric aerosol source and sea spray source, while the only sink is coalescence scavenging. Despite of simplicity, the model predicts N_d with little bias and a correlation coefficient of ~0.7 compared with observations, demonstrating the source-sink framework shows skill in capturing observed SO N_d variability. Coalescence scavenging is found to be an important sink of cloud condensation nuclei for precipitating stratocumulus and reduces the predicted N_d by as much as 90% depending on the precipitation rate. The free tropospheric aerosol source controls N_d more strongly than the surface aerosol source during the austral summer.

In Chapter 4, a range of diverse datasets were used to evaluate and untangle the bias in E3SMv2 simulated clouds, aerosols, and sulfur species. The default E3SMv2 underestimates N_d by a factor of 2 when compared with observations with 3km-resolution simulations. Updating the DMS emission and chemistry leads to a better agreement between the model and the observations in N_d and boundary layer aerosols, but large biases persist in the free troposphere aerosols (especially those accumulation mode aerosols that are likely to serve as CCN). Biases in

the free troposphere aerosols are likely attributable to insufficient particle growth, and in simulated sulfur species, due to incomplete DMS chemistry, highlighting the need for further efforts to improve the model treatment of relevant processes.

Bibliography

Abdul-Razzak, H., & Ghan, S. J. (2000). A parameterization of aerosol activation: 2. Multiple aerosol types. Journal of Geophysical Research: Atmospheres, 105(D5), 6837–6844. https://doi.org/10.1029/1999JD901161

Atlas, R. L., Bretherton, C. S., Blossey, P. N., Gettelman, A., Bardeen, C., Lin, P., & Ming, Y. (2020). How Well Do Large-Eddy Simulations and Global Climate Models Represent Observed Boundary Layer Structures and Low Clouds Over the Summertime Southern Ocean? Journal of Advances in Modeling Earth Systems, 12(11), e2020MS002205. https://doi.org/10.1029/2020MS002205

Ayers, G. P., & Gras, J. L. (1991). Seasonal relationship between cloud condensation nuclei and aerosol methanesulphonate in marine air. Nature, 353(6347), 834–835. https://doi.org/10.1038/353834a0

Ayres, G. P., Cainey, J. M., Gillett, R. W., & Ivey, J. P. (1997). Atmospheric sulphur and cloud condensation nuclei in marine air in the Southern Hemisphere. *Philosophical Transactions of the Royal Society B: Biological Sciences*, *352*(1350), 203–211. https://doi.org/10.1098/rstb.1997.0015

Baltensperger, U., Schwikowski, M., Jost, D. T., Nyeki, S., Gäggeler, H. W., & Poulida, O. (1998). Scavenging of atmospheric constituents in mixed phase clouds at the high-alpine site jungfraujoch part I: Basic concept and aerosol scavenging by clouds. *Atmospheric Environment*, *32*(23), 3975–3983. https://doi.org/10.1016/S1352-2310(98)00051-X

Bates, T. S., Huebert, B. J., Gras, J. L., Griffiths, F. B., & Durkee, P. A. (1998). International Global Atmospheric Chemistry (IGAC) Project's First Aerosol Characterization Experiment (ACE 1): Overview. Journal of Geophysical Research: Atmospheres, 103(D13), 16297–16318. https://doi.org/10.1029/97JD03741

Bates, T. S., Kapustin, V. N., Quinn, P. K., Covert, D. S., Coffman, D. J., Mari, C., et al. (1998). Processes controlling the distribution of aerosol particles in the lower marine boundary layer during the First Aerosol Characterization Experiment (ACE 1). *Journal of Geophysical Research: Atmospheres*, *103*(D13), 16369–16383. https://doi.org/10.1029/97JD03720

Beard, K. V. (1976). Terminal Velocity and Shape of Cloud and Precipitation Drops Aloft. Journal of the Atmospheric Sciences, 33(5), 851–864. https://doi.org/10.1175/1520-0469(1976)033<0851:TVASOC>2.0.CO;2

Bellouin, N., Quaas, J., Gryspeerdt, E., Kinne, S., Stier, P., Watson-Parris, D., et al. (2020). Bounding Global Aerosol Radiative Forcing of Climate Change. Reviews of Geophysics, 58(1), e2019RG000660. https://doi.org/10.1029/2019RG000660

Berner, A. H., Bretherton, C. S., & Wood, R. (2011). Large-eddy simulation of mesoscale dynamics and entrainment around a pocket of open cells observed in VOCALS-REx RF06. *Atmospheric Chemistry and Physics*, *11*(20), 10525–10540. https://doi.org/10.5194/acp-11-10525-2011

Bessho, K., Date, K., Hayashi, M., Ikeda, A., Imai, T., Inoue, H., et al. (2016). An Introduction to Himawari-8/9— Japan's New-Generation Geostationary Meteorological Satellites. Journal of the Meteorological Society of Japan. Ser. II, 94(2), 151–183. https://doi.org/10.2151/jmsj.2016-009

Bhatti, Y., Revell, L., Schuddeboom, A., McDonald, A., Archibald, A., Williams, J., et al. (2023). The sensitivity of Southern Ocean atmospheric dimethyl sulfide to modelled sources and emissions. EGUsphere, 1–32. https://doi.org/10.5194/egusphere-2023-868

Bian, H., Chin, M., Colarco, P. R., Apel, E. C., Blake, D. R., Froyd, K., et al. (2024). Observationally constrained analysis of sulfur cycle in the marine atmosphere with NASA ATom measurements and AeroCom model simulations. Atmospheric Chemistry and Physics, 24(3), 1717–1741. https://doi.org/10.5194/acp-24-1717-2024

Bjordal, J., Storelvmo, T., Alterskjær, K., & Carlsen, T. (2020). Equilibrium climate sensitivity above 5 °C plausible due to state-dependent cloud feedback. Nature Geoscience, 13(11), 718–721. https://doi.org/10.1038/s41561-020-00649-1

Bodas-Salcedo, A., Hill, P. G., Furtado, K., Williams, K. D., Field, P. R., Manners, J. C., et al. (2016). Large Contribution of Supercooled Liquid Clouds to the Solar Radiation Budget of the Southern Ocean. Journal of Climate, 29(11), 4213–4228. https://doi.org/10.1175/JCLI-D-15-0564.1

Bodas-Salcedo, A., Williams, K. D., Ringer, M. A., Beau, I., Cole, J. N. S., Dufresne, J.-L., et al. (2014). Origins of the Solar Radiation Biases over the Southern Ocean in CFMIP2 Models. Journal of Climate, 27(1), 41–56. https://doi.org/10.1175/JCLI-D-13-00169.1

Bohren, C. F., & Huffman, D. R. (1983). Absorption and scattering of light by small particles. Weinheim: Wiley : Wiley Online Library.

Boucher, O., & Lohmann, U. (1995). The sulfate-CCN-cloud albedo effect. *Tellus B: Chemical and Physical Meteorology*, *47*(3), 281–300. https://doi.org/10.3402/tellusb.v47i3.16048

Boyd, P. W., & Law, C. S. (2001). The Southern Ocean Iron RElease Experiment (SOIREE)—introduction and summary. Deep Sea Research Part II: Topical Studies in Oceanography, 48(11), 2425–2438. https://doi.org/10.1016/S0967-0645(01)00002-9

Burkholder. (2015). JPL Publication 15-10: Chemical Kinetics and Photochemical Data for Use in Atmospheric Studies.

Burrows, S. M., Easter, R. C., Liu, X., Ma, P.-L., Wang, H., Elliott, S. M., et al. (2022). OCEANFILMS (Organic Compounds from Ecosystems to Aerosols: Natural Films and Interfaces via Langmuir Molecular Surfactants) sea spray organic aerosol emissions – implementation in a global climate model and impacts on clouds. Atmospheric Chemistry and Physics, 22(8), 5223–5251. https://doi.org/10.5194/acp-22-5223-2022

Carslaw, K. S., Lee, L. A., Reddington, C. L., Pringle, K. J., Rap, A., Forster, P. M., et al. (2013). Large contribution of natural aerosols to uncertainty in indirect forcing. Nature, 503(7474), 67–71. https://doi.org/10.1038/nature12674

Ceppi, P., Hwang, Y.-T., Liu, X., Frierson, D. M. W., & Hartmann, D. L. (2013). The relationship between the ITCZ and the Southern Hemispheric eddy-driven jet. *Journal of Geophysical Research: Atmospheres*, *118*(11), 5136–5146. https://doi.org/10.1002/jgrd.50461

Cesana, G. V., Khadir, T., Chepfer, H., & Chiriaco, M. (2022). Southern Ocean Solar Reflection Biases in CMIP6 Models Linked to Cloud Phase and Vertical Structure Representations. Geophysical Research Letters, 49(22), e2022GL099777. https://doi.org/10.1029/2022GL099777

Chen, Q., Sherwen, T., Evans, M., & Alexander, B. (2018). DMS oxidation and sulfur aerosol formation in the marine troposphere: a focus on reactive halogen and multiphase chemistry. Atmospheric Chemistry and Physics, 18(18), 13617–13637. https://doi.org/10.5194/acp-18-13617-2018

Christensen, M. W., Jones, W. K., & Stier, P. (2020). Aerosols enhance cloud lifetime and brightness along the stratus-to-cumulus transition. *Proceedings of the National Academy of Sciences*, *117*(30), 17591–17598. https://doi.org/10.1073/pnas.1921231117

Chubb, T., Huang, Y., Jensen, J., Campos, T., Siems, S., & Manton, M. (2016). Observations of high droplet number concentrations in Southern Ocean boundary layer clouds. Atmospheric Chemistry and Physics, 16(2), 971–987. https://doi.org/10.5194/acp-16-971-2016

Clarke, A. D., Varner, J. L., Eisele, F., Mauldin, R. L., Tanner, D., & Litchy, M. (1998). Particle production in the remote marine atmosphere: Cloud outflow and subsidence during ACE 1. *Journal of Geophysical Research: Atmospheres*, *103*(D13), 16397–16409. https://doi.org/10.1029/97JD02987

Clarke, Antony D. (1993). Atmospheric nuclei in the Pacific midtroposphere: Their nature, concentration, and evolution. Journal of Geophysical Research: Atmospheres, 98(D11), 20633–20647. https://doi.org/10.1029/93JD00797

Clarke, Antony D., Owens, S. R., & Zhou, J. (2006). An ultrafine sea-salt flux from breaking waves: Implications for cloud condensation nuclei in the remote marine atmosphere. *Journal of Geophysical Research: Atmospheres*, *111*(D6). https://doi.org/10.1029/2005JD006565

Comstock, K. K., Wood, R., Yuter, S. E., & Bretherton, C. S. (2004). Reflectivity and rain rate in and below drizzling stratocumulus. *Quarterly Journal of the Royal Meteorological Society*, *130*(603), 2891–2918. https://doi.org/10.1256/qj.03.187

Covert, D. S., Kapustin, V. N., Bates, T. S., & Quinn, P. K. (1996). Physical properties of marine boundary layer aerosol particles of the mid-Pacific in relation to sources and meteorological transport. *Journal of Geophysical Research: Atmospheres*, *101*(D3), 6919–6930. https://doi.org/10.1029/95JD03068

Curran, M. A. J., & Jones, G. B. (2000). Dimethyl sulfide in the Southern Ocean: Seasonality and flux. *Journal of Geophysical Research: Atmospheres*, *105*(D16), 20451–20459. https://doi.org/10.1029/2000JD900176

D'Alessandro, J. J., McFarquhar, G. M., Wu, W., Stith, J. L., Jensen, J. B., & Rauber, R. M. (2021). Characterizing the Occurrence and Spatial Heterogeneity of Liquid, Ice, and Mixed Phase Low-Level Clouds Over the Southern Ocean Using in Situ Observations Acquired During SOCRATES. Journal of Geophysical Research: Atmospheres, 126(11), e2020JD034482. https://doi.org/10.1029/2020JD034482

D'Alessandro, J., Schima, J., & McFarquhar, G. (2022). SOCRATES Cloud Phase Product. Version 1.0 (Version 1.0) [Dataset]. UCAR/NCAR - Earth Observing Laboratory. https://doi.org/10.26023/S6WS-G5QE-H113

Danker, J., Sourdeval, O., McCoy, I. L., Wood, R., & Possner, A. (2021). Exploring Relations between Cloud Morphology, Cloud Phase, and Cloud Radiative Properties in Southern Ocean Stratocumulus Clouds. *Atmospheric Chemistry and Physics Discussions*, 1–26. https://doi.org/10.5194/acp-2021-926

Diamond, M. S., Director, H. M., Eastman, R., Possner, A., & Wood, R. (2020). Substantial Cloud Brightening From Shipping in Subtropical Low Clouds. *AGU Advances*, *1*(1), e2019AV000111. https://doi.org/10.1029/2019AV000111

DMT: Ultra High Sensitivity Aerosol Spectrometer (UHSAS) Operator Manual, Boulder, CO, 2013.

Eastman, R., Lebsock, M., & Wood, R. (2019). Warm Rain Rates from AMSR-E 89-GHz Brightness Temperatures Trained Using CloudSat Rain-Rate Observations. Journal of Atmospheric and Oceanic Technology, 36(6), 1033–1051. https://doi.org/10.1175/JTECH-D-18-0185.1

Ellis, S. M., Tsai, P., Burghart, C., Romatschke, U., Dixon, M., Vivekanandan, J., et al. (2019). Use of the Earth's Surface as a Reference to Correct Airborne Nadir-Looking Radar Radial Velocity Measurements for Platform Motion. Journal of Atmospheric and Oceanic Technology, 36(7), 1343–1360. https://doi.org/10.1175/JTECH-D-19-0019.1

Ellis, T. D., L'Ecuyer, T., Haynes, J. M., & Stephens, G. L. (2009). How often does it rain over the global oceans? The perspective from CloudSat. Geophysical Research Letters, 36(3). https://doi.org/10.1029/2008GL036728

Eloranta, E. E. (2005). High Spectral Resolution Lidar. In C. Weitkamp (Ed.), Lidar: Range-Resolved Optical Remote Sensing of the Atmosphere (pp. 143–163). New York, NY: Springer. https://doi.org/10.1007/0-387-25101-4_5

Emmons, L. K., Schwantes, R. H., Orlando, J. J., Tyndall, G., Kinnison, D., Lamarque, J.-F., et al. (2020). The Chemistry Mechanism in the Community Earth System Model Version 2 (CESM2). Journal of Advances in Modeling Earth Systems, 12(4), e2019MS001882. https://doi.org/10.1029/2019MS001882

Faber, S., French, J. R., & Jackson, R. (2018). Laboratory and in-flight evaluation of measurement uncertainties from a commercial Cloud Droplet Probe (CDP). Atmospheric Measurement Techniques, 11(6), 3645–3659. https://doi.org/10.5194/amt-11-3645-2018

Feingold, G., Kreidenweis, S. M., Stevens, B., & Cotton, W. R. (1996). Numerical simulations of stratocumulus processing of cloud condensation nuclei through collision-coalescence. Journal of Geophysical Research: Atmospheres, 101(D16), 21391–21402. https://doi.org/10.1029/96JD01552

Fiddes, S. L., Protat, A., Mallet, M. D., Alexander, S. P., & Woodhouse, M. T. (2022). Southern Ocean cloud and shortwave radiation biases in a nudged climate model simulation: does the model ever get it right? Atmospheric Chemistry and Physics, 22(22), 14603–14630. https://doi.org/10.5194/acp-22-14603-2022

Flanner, M. G., Liu, X., Zhou, C., Penner, J. E., & Jiao, C. (2012). Enhanced solar energy absorption by internally-mixed black carbon in snow grains. *Atmospheric Chemistry and Physics*, *12*(10), 4699–4721. https://doi.org/10.5194/acp-12-4699-2012

Fossum, K. N., Ovadnevaite, J., Ceburnis, D., Dall'Osto, M., Marullo, S., Bellacicco, M., et al. (2018). Summertime Primary and Secondary Contributions to Southern Ocean Cloud Condensation Nuclei. Scientific Reports, 8(1), 13844. https://doi.org/10.1038/s41598-018-32047-4

Frisch, A. S., Fairall, C. W., & Snider, J. B. (1995). Measurement of Stratus Cloud and Drizzle Parameters in ASTEX with a Kα-Band Doppler Radar and a Microwave Radiometer. Journal of the Atmospheric Sciences, 52(16), 2788–2799. https://doi.org/10.1175/1520-0469(1995)052<2788:MOSCAD>2.0.CO;2

Fröhlich, R., Cubison, M. J., Slowik, J. G., Bukowiecki, N., Prévôt, A. S. H., Baltensperger, U., et al. (2013). The ToF-ACSM: a portable aerosol chemical speciation monitor with TOFMS detection. Atmospheric Measurement Techniques, 6(11), 3225–3241. https://doi.org/10.5194/amt-6-3225-2013

Frölicher, T. L., Sarmiento, J. L., Paynter, D. J., Dunne, J. P., Krasting, J. P., & Winton, M. (2015). Dominance of the Southern Ocean in Anthropogenic Carbon and Heat Uptake in CMIP5 Models. Journal of Climate, 28(2), 862–886. https://doi.org/10.1175/JCLI-D-14-00117.1

Fung, K. M., Heald, C. L., Kroll, J. H., Wang, S., Jo, D. S., Gettelman, A., et al. (2022). Exploring dimethyl sulfide (DMS) oxidation and implications for global aerosol radiative forcing.

Atmospheric Chemistry and Physics, 22(2), 1549–1573. https://doi.org/10.5194/acp-22-1549-2022

Galí, M., Levasseur, M., Devred, E., Simó, R., & Babin, M. (2018). Sea-surface dimethylsulfide (DMS) concentration from satellite data at global and regional scales. Biogeosciences, 15(11), 3497–3519. https://doi.org/10.5194/bg-15-3497-2018

Gao, C. Y., Heald, C. L., Katich, J. M., Luo, G., & Yu, F. (2022). Remote Aerosol Simulated During the Atmospheric Tomography (ATom) Campaign and Implications for Aerosol Lifetime. Journal of Geophysical Research: Atmospheres, 127(22), e2022JD036524. https://doi.org/10.1029/2022JD036524

Garrett, T. J., & Zhao, C. (2006). Increased Arctic cloud longwave emissivity associated with pollution from mid-latitudes. *Nature*, *440*(7085), 787–789. https://doi.org/10.1038/nature04636

Garrett, T., Zhao, C., & Novelli, P. (2010). Assessing the relative contributions of transport efficiency and scavenging to seasonal variability in Arctic aerosol. *Tellus B: Chemical and Physical Meteorology*, *62*(3), 190–196. https://doi.org/10.1111/j.1600-0889.2010.00453.x

Ge, W., Liu, J., Xiang, S., Zhou, Y., Zhou, J., Hu, X., et al. (2022). Improvement and Uncertainties of Global Simulation of Sulfate Concentration and Radiative Forcing in CESM2. Journal of Geophysical Research: Atmospheres, 127(20), e2022JD037623. https://doi.org/10.1029/2022JD037623

Geoffroy, O., Brenguier, J.-L., & Sandu, I. (2008). Relationship between drizzle rate, liquid water path and droplet concentration at the scale of a stratocumulus cloud system. Atmospheric Chemistry and Physics, 8(16), 4641–4654. https://doi.org/10.5194/acp-8-4641-2008

Gettelman, A., & Morrison, H. (2015). Advanced Two-Moment Bulk Microphysics for Global Models. Part I: Off-Line Tests and Comparison with Other Schemes. Journal of Climate, 28(3), 1268–1287. https://doi.org/10.1175/JCLI-D-14-00102.1

Gettelman, A., Hannay, C., Bacmeister, J. T., Neale, R. B., Pendergrass, A. G., Danabasoglu, G., et al. (2019). High Climate Sensitivity in the Community Earth System Model Version 2 (CESM2). *Geophysical Research Letters*, *46*(14), 8329–8337. https://doi.org/10.1029/2019GL083978

Ghan, S. J., Smith, S. J., Wang, M., Zhang, K., Pringle, K., Carslaw, K., et al. (2013). A simple model of global aerosol indirect effects. Journal of Geophysical Research: Atmospheres, 118(12), 6688–6707. https://doi.org/10.1002/jgrd.50567

Ghate, V. P., & Cadeddu, M. P. (2019). Drizzle and turbulence below closed cellular marine stratocumulus clouds. Journal of Geophysical Research-Atmospheres, 124(11), 2018JD030141. https://doi.org/10.1029/2018JD030141

Golaz, J.-C., Larson, V. E., & Cotton, W. R. (2002). A PDF-Based Model for Boundary Layer Clouds. Part I: Method and Model Description. Journal of the Atmospheric Sciences, 59(24), 3540–3551. https://doi.org/10.1175/1520-0469(2002)059<3540:APBMFB>2.0.CO;2

Golaz, J., Van Roekel, L. P., Zheng, X., Roberts, A. F., Wolfe, J. D., Lin, W., et al. (2022). The DOE E3SM Model Version 2: Overview of the Physical Model and Initial Model Evaluation.

Journal of Advances in Modeling Earth Systems, 14(12), e2022MS003156. https://doi.org/10.1029/2022MS003156

Gong, S. L. (2003). A parameterization of sea-salt aerosol source function for sub- and super-micron particles. *Global Biogeochemical Cycles*, *17*(4). https://doi.org/10.1029/2003GB002079

Grecu, M., Olson, W. S., Munchak, S. J., Ringerud, S., Liao, L., Haddad, Z., et al. (2016). The GPM Combined Algorithm. Journal of Atmospheric and Oceanic Technology, 33(10), 2225–2245. https://doi.org/10.1175/JTECH-D-16-0019.1

Grise, K. M., & Medeiros, B. (2016). Understanding the Varied Influence of Midlatitude Jet Position on Clouds and Cloud Radiative Effects in Observations and Global Climate Models. Journal of Climate, 29(24), 9005–9025. https://doi.org/10.1175/JCLI-D-16-0295.1

Grosvenor, D. P., Field, P. R., Hill, A. A., & Shipway, B. J. (2017). The relative importance of macrophysical and cloud albedo changes for aerosol-induced radiative effects in closed-cell stratocumulus: insight from the modelling of a case study. *Atmospheric Chemistry and Physics*, *17*(8), 5155–5183. https://doi.org/10.5194/acp-17-5155-2017

Grosvenor, D. P., Sourdeval, O., Zuidema, P., Ackerman, A., Alexandrov, M. D., Bennartz, R., et al. (2018). Remote Sensing of Droplet Number Concentration in Warm Clouds: A Review of the Current State of Knowledge and Perspectives. Reviews of Geophysics, 56(2), 409–453. https://doi.org/10.1029/2017RG000593

Gryspeerdt, E., Povey, A. C., Grainger, R. G., Hasekamp, O., Hsu, N. C., Mulcahy, J. P., et al. (2023). Uncertainty in aerosol–cloud radiative forcing is driven by clean conditions. Atmospheric Chemistry and Physics, 23(7), 4115–4122. https://doi.org/10.5194/acp-23-4115-2023

Grythe, H., Ström, J., Krejci, R., Quinn, P., & Stohl, A. (2014). A review of sea-spray aerosol source functions using a large global set of sea salt aerosol concentration measurements. *Atmospheric Chemistry and Physics*, *14*(3), 1277–1297. https://doi.org/10.5194/acp-14-1277-2014

Hamilton, D. S., Lee, L. A., Pringle, K. J., Reddington, C. L., Spracklen, D. V., & Carslaw, K. S. (2014). Occurrence of pristine aerosol environments on a polluted planet. Proceedings of the National Academy of Sciences, 111(52), 18466–18471. https://doi.org/10.1073/pnas.1415440111

Hartery, S., Toohey, D., Revell, L., Sellegri, K., Kuma, P., Harvey, M., & McDonald, A. J. (2020). Constraining the Surface Flux of Sea Spray Particles From the Southern Ocean. *Journal of Geophysical Research: Atmospheres*, *125*(4), e2019JD032026. https://doi.org/10.1029/2019JD032026

Haynes, J. M., L'Ecuyer, T. S., Stephens, G. L., Miller, S. D., Mitrescu, C., Wood, N. B., & Tanelli, S. (2009). Rainfall retrieval over the ocean with spaceborne W-band radar. Journal of Geophysical Research: Atmospheres, 114(D8). https://doi.org/10.1029/2008JD009973

Hegg, D. A., Clarke, A. D., Doherty, S. J., & Ström4, J. (2011). Measurements of black carbon aerosol washout ratio on Svalbard. *Tellus B: Chemical and Physical Meteorology*, *63*(5), 891–900. https://doi.org/10.1111/j.1600-0889.2011.00577.x

Holtslag, A. a. M., & Boville, B. A. (1993). Local Versus Nonlocal Boundary-Layer Diffusion in a Global Climate Model. Journal of Climate, 6(10), 1825–1842. https://doi.org/10.1175/1520-0442(1993)006<1825:LVNBLD>2.0.CO;2

Hopkins, F. E., Archer, S. D., Bell, T. G., Suntharalingam, P., & Todd, J. D. (2023). The biogeochemistry of marine dimethylsulfide. Nature Reviews Earth & Environment, 4(6), 361–376. https://doi.org/10.1038/s43017-023-00428-7

Hsu, S. A., Meindl, E. A., & Gilhousen, D. B. (1994). Determining the Power-Law Wind-Profile Exponent under Near-Neutral Stability Conditions at Sea. *Journal of Applied Meteorology and Climatology*, *33*(6), 757–765. https://doi.org/10.1175/1520-0450(1994)033<0757:DTPLWP>2.0.CO;2

Huang, Y., Chubb, T., Baumgardner, D., deHoog, M., Siems, S. T., & Manton, M. J. (2017). Evidence for secondary ice production in Southern Ocean open cellular convection. *Quarterly Journal of the Royal Meteorological Society*, *143*(704), 1685–1703. https://doi.org/10.1002/qj.3041

Huang, Y., Siems, S. T., Manton, M. J., Rosenfeld, D., Marchand, R., McFarquhar, G. M., & Protat, A. (2016). What is the Role of Sea Surface Temperature in Modulating Cloud and Precipitation Properties over the Southern Ocean? *Journal of Climate*, *29*(20), 7453–7476. https://doi.org/10.1175/JCLI-D-15-0768.1

Hudson, J. G., Xie, Y., & Yum, S. S. (1998). Vertical distributions of cloud condensation nuclei spectra over the summertime Southern Ocean. *Journal of Geophysical Research: Atmospheres*, *103*(D13), 16609–16624. https://doi.org/10.1029/97JD03438

Hulswar, S., Simó, R., Galí, M., Bell, T. G., Lana, A., Inamdar, S., et al. (2022). Third revision of the global surface seawater dimethyl sulfide climatology (DMS-Rev3). Earth System Science Data, 14(7), 2963–2987. https://doi.org/10.5194/essd-14-2963-2022

Humphries, R. S., Keywood, M. D., Ward, J. P., Harnwell, J., Alexander, S. P., Klekociuk, A. R., et al. (2023). Measurement report: Understanding the seasonal cycle of Southern Ocean aerosols. Atmospheric Chemistry and Physics, 23(6), 3749–3777. https://doi.org/10.5194/acp-23-3749-2023

Humphries, R. S., Klekociuk, A. R., Schofield, R., Keywood, M., Ward, J., & Wilson, S. R. (2016). Unexpectedly high ultrafine aerosol concentrations above East Antarctic sea ice. *Atmospheric Chemistry and Physics*, *16*(4), 2185–2206. https://doi.org/10.5194/acp-16-2185-2016

Humphries, Ruhi S., Keywood, M. D., Gribben, S., McRobert, I. M., Ward, J. P., Selleck, P., et al. (2021). Southern Ocean latitudinal gradients of cloud condensation nuclei. *Atmospheric Chemistry and Physics*, *21*(16), 12757–12782. https://doi.org/10.5194/acp-21-12757-2021

Hwang, Y.-T., & Frierson, D. M. W. (2013). Link between the double-Intertropical Convergence Zone problem and cloud biases over the Southern Ocean. *Proceedings of the National Academy of Sciences*, *110*(13), 4935–4940. https://doi.org/10.1073/pnas.1213302110

Hyder, P., Edwards, J. M., Allan, R. P., Hewitt, H. T., Bracegirdle, T. J., Gregory, J. M., et al. (2018). Critical Southern Ocean climate model biases traced to atmospheric model cloud errors. Nature Communications, 9(1), 3625. https://doi.org/10.1038/s41467-018-05634-2

Illingworth, A. J., & Blackman, T. M. (2002). The Need to Represent Raindrop Size Spectra as Normalized Gamma Distributions for the Interpretation of Polarization Radar Observations. Journal of Applied Meteorology, 41(3), 286–297. https://doi.org/10.1175/1520-0450(2002)041<0286:TNTRRS>2.0.CO;2

Jia, H., & Quaas, J. (2023). Nonlinearity of the cloud response postpones climate penalty of mitigating air pollution in polluted regions. Nature Climate Change, 13(9), 943–950. https://doi.org/10.1038/s41558-023-01775-5

Kang, L., Marchand, R. T., Wood, R., & McCoy, I. L. (2022). Coalescence Scavenging Drives Droplet Number Concentration in Southern Ocean Low Clouds. Geophysical Research Letters, 49(7), e2022GL097819. https://doi.org/10.1029/2022GL097819

Kang, L., Marchand, R., & Smith, W. (2021). Evaluation of MODIS and Himawari-8 Low Clouds Retrievals Over the Southern Ocean With In Situ Measurements From the SOCRATES Campaign. *Earth and Space Science*, *8*(3), e2020EA001397. https://doi.org/10.1029/2020EA001397

Kang, L., Marchand, R. T., & Wood, R. (2024). Stratocumulus Precipitation Properties Over the Southern Ocean Observed From Aircraft During the SOCRATES Campaign. *Journal of Geophysical Research: Atmospheres*, *129*(6), e2023JD039831. https://doi.org/10.1029/2023JD039831

Kay, J. E., Hillman, B. R., Klein, S. A., Zhang, Y., Medeiros, B., Pincus, R., et al. (2012). Exposing Global Cloud Biases in the Community Atmosphere Model (CAM) Using Satellite Observations and Their Corresponding Instrument Simulators. Journal of Climate, 25(15), 5190–5207. https://doi.org/10.1175/JCLI-D-11-00469.1

Kerminen, V.-M., Chen, X., Vakkari, V., Petäjä, T., Kulmala, M., & Bianchi, F. (2018). Atmospheric new particle formation and growth: review of field observations. Environmental Research Letters, 13(10), 103003. https://doi.org/10.1088/1748-9326/aadf3c

Kettle, A. J., Andreae, M. O., Amouroux, D., Andreae, T. W., Bates, T. S., Berresheim, H., et al. (1999). A global database of sea surface dimethylsulfide (DMS) measurements and a procedure

to predict sea surface DMS as a function of latitude, longitude, and month. Global Biogeochemical Cycles, 13(2), 399–444. https://doi.org/10.1029/1999GB900004

Khatiwala, S., Primeau, F., & Hall, T. (2009). Reconstruction of the history of anthropogenic CO2 concentrations in the ocean. Nature, 462(7271), 346–349. https://doi.org/10.1038/nature08526

Klepp, C., Michel, S., Protat, A., Burdanowitz, J., Albern, N., Kähnert, M., et al. (2018). OceanRAIN, a new in-situ shipboard global ocean surface-reference dataset of all water cycle components. Scientific Data, 5(1), 180122. https://doi.org/10.1038/sdata.2018.122

Koga, S., Nomura, D., & Wada, M. (2014). Variation of dimethylsulfide mixing ratio over the Southern Ocean from 36°S to 70°S. Polar Science, 8(3), 306–313. https://doi.org/10.1016/j.polar.2014.04.002

Korhonen, H., Carslaw, K. S., Spracklen, D. V., Mann, G. W., & Woodhouse, M. T. (2008). Influence of oceanic dimethyl sulfide emissions on cloud condensation nuclei concentrations and seasonality over the remote Southern Hemisphere oceans: A global model study. Journal of Geophysical Research: Atmospheres, 113(D15). https://doi.org/10.1029/2007JD009718

Lamarque, J.-F., Bond, T. C., Eyring, V., Granier, C., Heil, A., Klimont, Z., et al. (2010). Historical (1850–2000) gridded anthropogenic and biomass burning emissions of reactive gases and aerosols: methodology and application. Atmospheric Chemistry and Physics, 10(15), 7017–7039. https://doi.org/10.5194/acp-10-7017-2010

Lana, A., Bell, T. G., Simó, R., Vallina, S. M., Ballabrera-Poy, J., Kettle, A. J., et al. (2011). An updated climatology of surface dimethlysulfide concentrations and emission fluxes in the global ocean. Global Biogeochemical Cycles, 25(1). https://doi.org/10.1029/2010GB003850

Lance, S., Brock, C. A., Rogers, D., & Gordon, J. A. (2010). Water droplet calibration of the Cloud Droplet Probe (CDP) and in-flight performance in liquid, ice and mixed-phase clouds during ARCPAC. Atmospheric Measurement Techniques, 3(6), 1683–1706. https://doi.org/10.5194/amt-3-1683-2010

Larson, V. E. (2022, March 26). CLUBB-SILHS: A parameterization of subgrid variability in the atmosphere. arXiv. https://doi.org/10.48550/arXiv.1711.03675

Lee, L. A., Reddington, C. L., & Carslaw, K. S. (2016). On the relationship between aerosol model uncertainty and radiative forcing uncertainty. Proceedings of the National Academy of Sciences, 113(21), 5820–5827. https://doi.org/10.1073/pnas.1507050113

Lee, S.-H., Gordon, H., Yu, H., Lehtipalo, K., Haley, R., Li, Y., & Zhang, R. (2019). New Particle Formation in the Atmosphere: From Molecular Clusters to Global Climate. Journal of Geophysical Research: Atmospheres, 124(13), 7098–7146. https://doi.org/10.1029/2018JD029356

Leung, L. R., Ringler, T., Collins, W. D., Taylor, M., & Ashfaq, M. (2013). A Hierarchical Evaluation of Regional Climate Simulations. Eos, Transactions American Geophysical Union, 94(34), 297–298. https://doi.org/10.1002/2013EO340001

Liu, M., & Matsui, H. (2022). Secondary Organic Aerosol Formation Regulates Cloud Condensation Nuclei in the Global Remote Troposphere. Geophysical Research Letters, 49(18), e2022GL100543. https://doi.org/10.1029/2022GL100543

Liu, P. S. K., Deng, R., Smith, K. A., Williams, L. R., Jayne, J. T., Canagaratna, M. R., et al. (2007). Transmission Efficiency of an Aerodynamic Focusing Lens System: Comparison of Model Calculations and Laboratory Measurements for the Aerodyne Aerosol Mass Spectrometer. Aerosol Science and Technology, 41(8), 721–733. https://doi.org/10.1080/02786820701422278

Liu, X., Easter, R. C., Ghan, S. J., Zaveri, R., Rasch, P., Shi, X., et al. (2012). Toward a minimal representation of aerosols in climate models: description and evaluation in the Community Atmosphere Model CAM5. Geoscientific Model Development, 5(3), 709–739. https://doi.org/10.5194/gmd-5-709-2012

Liu, X., Ma, P.-L., Wang, H., Tilmes, S., Singh, B., Easter, R. C., et al. (2016). Description and evaluation of a new four-mode version of the Modal Aerosol Module (MAM4) within version 5.3 of the Community Atmosphere Model. Geoscientific Model Development, 9(2), 505–522. https://doi.org/10.5194/gmd-9-505-2016

Lohmann, U., & Feichter, J. (2005). Global indirect aerosol effects: a review. *Atmospheric Chemistry and Physics*, *5*(3), 715–737. https://doi.org/10.5194/acp-5-715-2005

Lu, M.-L., Sorooshian, A., Jonsson, H. H., Feingold, G., Flagan, R. C., & Seinfeld, J. H. (2009). Marine stratocumulus aerosol-cloud relationships in the MASE-II experiment: Precipitation susceptibility in eastern Pacific marine stratocumulus. Journal of Geophysical Research: Atmospheres, 114(D24). https://doi.org/10.1029/2009JD012774

Mace, G. G. (2010). Cloud properties and radiative forcing over the maritime storm tracks of the Southern Ocean and North Atlantic derived from A-Train. *Journal of Geophysical Research: Atmospheres*, *115*(D10). https://doi.org/10.1029/2009JD012517

Mace, G. G., & Avey, S. (2017). Seasonal variability of warm boundary layer cloud and precipitation properties in the Southern Ocean as diagnosed from A-Train data. Journal of Geophysical Research: Atmospheres, 122(2), 1015–1032. https://doi.org/10.1002/2016JD025348

Mace, G. G., & Protat, A. (2018). Clouds over the Southern Ocean as Observed from the R/V Investigator during CAPRICORN. Part I: Cloud Occurrence and Phase Partitioning. Journal of Applied Meteorology and Climatology, 57(8), 1783–1803. https://doi.org/10.1175/JAMC-D-17-0194.1

Mace, G. G., Benson, S., & Hu, Y. (2020). On the Frequency of Occurrence of the Ice Phase in Supercooled Southern Ocean Low Clouds Derived From CALIPSO and CloudSat. Geophysical Research Letters, 47(14), e2020GL087554. https://doi.org/10.1029/2020GL087554

Mace, G. G., Heymsfield, A. J., & Poellot, M. R. (2002). On retrieving the microphysical properties of cirrus clouds using the moments of the millimeter-wavelength Doppler spectrum. Journal of Geophysical Research: Atmospheres, 107(D24), AAC 22-1-AAC 22-26. https://doi.org/10.1029/2001JD001308

Mace, G. G., Zhang, Q., Vaughan, M., Marchand, R., Stephens, G., Trepte, C., & Winker, D. (2009). A description of hydrometeor layer occurrence statistics derived from the first year of merged Cloudsat and CALIPSO data. *Journal of Geophysical Research: Atmospheres*, *114*(D8). https://doi.org/10.1029/2007JD009755

Mahajan, A. S., Fadnavis, S., Thomas, M. A., Pozzoli, L., Gupta, S., Royer, S.-J., et al. (2015). Quantifying the impacts of an updated global dimethyl sulfide climatology on cloud microphysics and aerosol radiative forcing. Journal of Geophysical Research: Atmospheres, 120(6), 2524–2536. https://doi.org/10.1002/2014JD022687

Mallet, M. D., Humphries, R. S., Fiddes, S. L., Alexander, S. P., Altieri, K., Angot, H., et al. (2023). Untangling the influence of Antarctic and Southern Ocean life on clouds. Elementa: Science of the Anthropocene, 11(1), 00130. https://doi.org/10.1525/elementa.2022.00130

Mann, J. A. L., Christine Chiu, J., Hogan, R. J., O'Connor, E. J., L'Ecuyer, T. S., Stein, T. H. M., & Jefferson, A. (2014). Aerosol impacts on drizzle properties in warm clouds from ARM Mobile Facility maritime and continental deployments. Journal of Geophysical Research: Atmospheres, 119(7), 4136–4148. https://doi.org/10.1002/2013JD021339

Marchand, R. T., Ackerman, T. P., & Moroney, C. (2007). An assessment of Multiangle Imaging Spectroradiometer (MISR) stereo-derived cloud top heights and cloud top winds using ground-based radar, lidar, and microwave radiometers. Journal of Geophysical Research: Atmospheres, 112(D6). https://doi.org/10.1029/2006JD007091

Marchand, R., Mace, G. G., Ackerman, T., & Stephens, G. (2008). Hydrometeor Detection Using Cloudsat—An Earth-Orbiting 94-GHz Cloud Radar. Journal of Atmospheric and Oceanic Technology, 25(4), 519–533. https://doi.org/10.1175/2007JTECHA1006.1

Matus, A. V., & L'Ecuyer, T. S. (2017). The role of cloud phase in Earth's radiation budget. Journal of Geophysical Research: Atmospheres, 122(5), 2559–2578. https://doi.org/10.1002/2016JD025951

McCoy, D. T., Burrows, S. M., Wood, R., Grosvenor, D. P., Elliott, S. M., Ma, P.-L., et al. (2015). Natural aerosols explain seasonal and spatial patterns of Southern Ocean cloud albedo. Science Advances. https://doi.org/10.1126/sciadv.1500157

McCoy, D. T., Hartmann, D. L., & Grosvenor, D. P. (2014). Observed Southern Ocean Cloud Properties and Shortwave Reflection. Part I: Calculation of SW Flux from Observed Cloud Properties. *Journal of Climate*, *27*(23), 8836–8857. https://doi.org/10.1175/JCLI-D-14-00287.1

McCoy, I. L., Bretherton, C. S., Wood, R., Twohy, C. H., Gettelman, A., Bardeen, C. G., & Toohey, D. W. (2021). Influences of Recent Particle Formation on Southern Ocean Aerosol Variability and Low Cloud Properties. Journal of Geophysical Research: Atmospheres, 126(8), e2020JD033529. https://doi.org/10.1029/2020JD033529

McCoy, I. L., McCoy, D. T., Wood, R., Regayre, L., Watson-Parris, D., Grosvenor, D. P., et al. (2020). The hemispheric contrast in cloud microphysical properties constrains aerosol forcing. Proceedings of the National Academy of Sciences, 117(32), 18998–19006. https://doi.org/10.1073/pnas.1922502117

McFarquhar, G. M., Bretherton, C. S., Marchand, R., Protat, A., DeMott, P. J., Alexander, S. P., et al. (2021). Observations of Clouds, Aerosols, Precipitation, and Surface Radiation over the

Southern Ocean: An Overview of CAPRICORN, MARCUS, MICRE, and SOCRATES. Bulletin of the American Meteorological Society, 102(4), E894–E928. https://doi.org/10.1175/BAMS-D-20-0132.1

McFarquhar, G. M., Finlon, J. A., Stechman, D. M., Wu, W., Jackson, R. C., & Freer, M. (2018). University of Illinois/Oklahoma optical Array probe (OAP) processing software. [Software]. Zenodo. https://doi.org/10.5281/zenodo.1285969

McNabb, B. J., & Tortell, P. D. (2023). Oceanographic controls on Southern Ocean dimethyl sulfide distributions revealed by machine learning algorithms. Limnology and Oceanography, 68(3), 616–630. https://doi.org/10.1002/lno.12298

Merikanto, J., Spracklen, D. V., Pringle, K. J., & Carslaw, K. S. (2010). Effects of boundary layer particle formation on cloud droplet number and changes in cloud albedo from 1850 to 2000. *Atmospheric Chemistry and Physics*, *10*(2), 695–705. https://doi.org/10.5194/acp-10-695-2010

Mitchell, D. L., & Lamb, D. (1989). Influence of riming on the chemical composition of snow in winter orographic storms. *Journal of Geophysical Research: Atmospheres*, *94*(D12), 14831–14840. https://doi.org/10.1029/JD094iD12p14831

Mitrescu, C., L'Ecuyer, T., Haynes, J., Miller, S., & Turk, J. (2010). CloudSat Precipitation Profiling Algorithm—Model Description. Journal of Applied Meteorology and Climatology, 49(5), 991–1003. https://doi.org/10.1175/2009JAMC2181.1

Mohrmann, J., Wood, R., McGibbon, J., Eastman, R., & Luke, E. (2018). Drivers of Seasonal Variability in Marine Boundary Layer Aerosol Number Concentration Investigated Using a Steady State Approach. *Journal of Geophysical Research: Atmospheres*, *123*(2), 1097–1112. https://doi.org/10.1002/2017JD027443

Monahan, E. C., & Muircheartaigh, I. (1980). Optimal Power-Law Description of Oceanic Whitecap Coverage Dependence on Wind Speed. *Journal of Physical Oceanography*, *10*(12), 2094–2099. https://doi.org/10.1175/1520-0485(1980)010<2094:OPLDOO>2.0.CO;2

Montoya Duque, E., Huang, Y., Siems, S. T., May, P. T., Protat, A., & McFarquhar, G. M. (2022). A Characterization of Clouds and Precipitation Over the Southern Ocean From Synoptic to Micro Scales During the CAPRICORN Field Campaigns. Journal of Geophysical Research: Atmospheres, 127(17), e2022JD036796. https://doi.org/10.1029/2022JD036796

Mülmenstädt, J., Salzmann, M., Kay, J. E., Zelinka, M. D., Ma, P.-L., Nam, C., et al. (2021). An underestimated negative cloud feedback from cloud lifetime changes. Nature Climate Change, 11(6), 508–513. https://doi.org/10.1038/s41558-021-01038-1

NCAR/EOL HCR Team & NCAR/EOL HSRL Team . (2021). SOCRATES: NCAR HCR radar and HSRL lidar moments data. Version 3.1 [Dataset]. UCAR/NCAR - Earth Observing Laboratory. https://doi.org/10.5065/D64J0CZS

Nicholls, S. (1984). The dynamics of stratocumulus: Aircraft observations and comparisons with a mixed layer model. Quarterly Journal of the Royal Meteorological Society, 110(466), 783–820. https://doi.org/10.1002/qj.49711046603

O'Connor, E. J., Hogan, R. J., & Illingworth, A. J. (2005). Retrieving Stratocumulus Drizzle Parameters Using Doppler Radar and Lidar. *Journal of Applied Meteorology and Climatology*, *44*(1), 14–27. https://doi.org/10.1175/JAM-2181.1

O'Shea, S. J., Choularton, T. W., Lloyd, G., Crosier, J., Bower, K. N., Gallagher, M., et al. (2016). Airborne observations of the microphysical structure of two contrasting cirrus clouds. Journal of Geophysical Research: Atmospheres, 121(22), 13,510-13,536. https://doi.org/10.1002/2016JD025278

Orr, B. W., & Kropfli, R. A. (1999). A Method for Estimating Particle Fall Velocities from Vertically Pointing Doppler Radar. Journal of Atmospheric and Oceanic Technology, 16(1), 29–37. https://doi.org/10.1175/1520-0426(1999)016<0029:AMFEPF>2.0.CO;2

Pawlowska, H., & Brenguier, J.-L. (2003). An observational study of drizzle formation in stratocumulus clouds for general circulation model (GCM) parameterizations. Journal of Geophysical Research: Atmospheres, 108(D15). https://doi.org/10.1029/2002JD002679

Petty, G. W., & Huang, W. (2011). The Modified Gamma Size Distribution Applied to Inhomogeneous and Nonspherical Particles: Key Relationships and Conversions. Journal of the Atmospheric Sciences, 68(7), 1460–1473. https://doi.org/10.1175/2011JAS3645.1

Prahl, S. (2023). miepython: Pure python implementation of Mie scattering. [Software]. Zenodo. https://zenodo.org/records/8218010

Protat, A., Klepp, C., Louf, V., Petersen, W. A., Alexander, S. P., Barros, A., et al. (2019a). The Latitudinal Variability of Oceanic Rainfall Properties and Its Implication for Satellite Retrievals: 1. Drop Size Distribution Properties. Journal of Geophysical Research: Atmospheres, 124(23), 13291–13311. https://doi.org/10.1029/2019JD031010

Protat, A., Klepp, C., Louf, V., Petersen, W. A., Alexander, S. P., Barros, A., et al. (2019b). The Latitudinal Variability of Oceanic Rainfall Properties and Its Implication for Satellite Retrievals: 1. Drop Size Distribution Properties. Journal of Geophysical Research: Atmospheres, 124(23), 13291–13311. https://doi.org/10.1029/2019JD031010

Qi, L., Li, Q., Li, Y., & He, C. (2017). Factors controlling black carbon distribution in the Arctic. *Atmospheric Chemistry and Physics*, *17*(2), 1037–1059. https://doi.org/10.5194/acp-17-1037-2017

Quinn, P. K., Coffman, D. J., Johnson, J. E., Upchurch, L. M., & Bates, T. S. (2017). Small fraction of marine cloud condensation nuclei made up of sea spray aerosol. *Nature Geoscience*, *10*(9), 674–679. https://doi.org/10.1038/ngeo3003

Raes, F. (1995). Entrainment of free tropospheric aerosols as a regulating mechanism for cloud condensation nuclei in the remote marine boundary layer. Journal of Geophysical Research: Atmospheres, 100(D2), 2893–2903. https://doi.org/10.1029/94JD02832

Rasch, P. J., Xie, S., Ma, P.-L., Lin, W., Wang, H., Tang, Q., et al. (2019). An Overview of the Atmospheric Component of the Energy Exascale Earth System Model. Journal of Advances in Modeling Earth Systems, 11(8), 2377–2411. https://doi.org/10.1029/2019MS001629

Revell, L. E., Kremser, S., Hartery, S., Harvey, M., Mulcahy, J. P., Williams, J., et al. (2019). The sensitivity of Southern Ocean aerosols and cloud microphysics to sea spray and sulfate

aerosol production in the HadGEM3-GA7.1 chemistry–climate model. *Atmospheric Chemistry and Physics*, *19*(24), 15447–15466. https://doi.org/10.5194/acp-19-15447-2019

Roberts, G. C., & Nenes, A. (2005). A Continuous-Flow Streamwise Thermal-Gradient CCN Chamber for Atmospheric Measurements. Aerosol Science and Technology, 39(3), 206–221. https://doi.org/10.1080/027868290913988

Romatschke, U., Dixon, M., Tsai, P., Loew, E., Vivekanandan, J., Emmett, J., & Rilling, R. (2021). The NCAR Airborne 94-GHz Cloud Radar: Calibration and Data Processing. Data, 6(6), 66. https://doi.org/10.3390/data6060066

Rosenfeld, D., & Ulbrich, C. W. (2003). Cloud Microphysical Properties, Processes, and Rainfall Estimation Opportunities. Meteorological Monographs, 30(52), 237–258. https://doi.org/10.1175/0065-9401(2003)030<0237:CMPPAR>2.0.CO;2

Rosenfeld, D., Kokhanovsky, A., Goren, T., Gryspeerdt, E., Hasekamp, O., Jia, H., et al. (2023). Frontiers in Satellite-Based Estimates of Cloud-Mediated Aerosol Forcing. Reviews of Geophysics, 61(4), e2022RG000799. https://doi.org/10.1029/2022RG000799

Sallée, J.-B., Shuckburgh, E., Bruneau, N., Meijers, A. J. S., Bracegirdle, T. J., Wang, Z., & Roy, T. (2013). Assessment of Southern Ocean water mass circulation and characteristics in CMIP5 models: Historical bias and forcing response. *Journal of Geophysical Research: Oceans*, *118*(4), 1830–1844. https://doi.org/10.1002/jgrc.20135

Sanchez, K. J., Roberts, G. C., Saliba, G., Russell, L. M., Twohy, C., Reeves, J. M., et al. (2021). Measurement report: Cloud processes and the transport of biological emissions affect southern ocean particle and cloud condensation nuclei concentrations. Atmospheric Chemistry and Physics, 21(5), 3427–3446. https://doi.org/10.5194/acp-21-3427-2021

Sanchez, K. J., Roberts, G. C., Saliba, G., Russell, L. M., Twohy, C., Reeves, J. M., et al. (2021). Measurement report: Cloud processes and the transport of biological emissions affect southern ocean particle and cloud condensation nuclei concentrations. Atmospheric Chemistry and Physics, 21(5), 3427–3446. https://doi.org/10.5194/acp-21-3427-2021

Sarkar, M., Zuidema, P., & Ghate, V. (2021). Clarifying Remotely Retrieved Precipitation of Shallow Marine Clouds from the NSF/NCAR Gulfstream V. Journal of Atmospheric and Oceanic Technology, 38(9), 1657–1670. https://doi.org/10.1175/JTECH-D-20-0166.1

Schima, J., McFarquhar, G., Romatschke, U., Vivekanandan, J., D'Alessandro, J., Haggerty, J., et al. (2022). Characterization of Southern Ocean Boundary Layer Clouds Using Airborne Radar, Lidar, and In Situ Cloud Data: Results From SOCRATES. Journal of Geophysical Research: Atmospheres, 127(21), e2022JD037277. https://doi.org/10.1029/2022JD037277

Schneider, D. P., & Reusch, D. B. (2016). Antarctic and Southern Ocean Surface Temperatures in CMIP5 Models in the Context of the Surface Energy Budget. *Journal of Climate*, *29*(5), 1689–1716. https://doi.org/10.1175/JCLI-D-15-0429.1

Schuddeboom, A. J., & McDonald, A. J. (2021). The Southern Ocean Radiative Bias, Cloud Compensating Errors, and Equilibrium Climate Sensitivity in CMIP6 Models. Journal of Geophysical Research: Atmospheres, 126(22), e2021JD035310. https://doi.org/10.1029/2021JD035310

Schwartz, M. C., Ghate, V. P., Albrecht, B. A., Zuidema, P., Cadeddu, M. P., Vivekanandan, J., et al. (2019). Merged Cloud and Precipitation Dataset from the HIAPER GV for the Cloud System Evolution in the Trades (CSET) Campaign. Journal of Atmospheric and Oceanic Technology, 36(6), 921–940. https://doi.org/10.1175/JTECH-D-18-0111.1

Seinfeld, J. H., & Pandis, S. N. (1998). Atmospheric Chemistry and Physics: From Air Pollution to Climate Change. Wiley.

Seto, S., Iguchi, T., & Oki, T. (2013). The Basic Performance of a Precipitation Retrieval Algorithm for the Global Precipitation Measurement Mission's Single/Dual-Frequency Radar Measurements. IEEE Transactions on Geoscience and Remote Sensing, 51(12), 5239–5251. https://doi.org/10.1109/TGRS.2012.2231686

Siems, S. T., Huang, Y., & Manton, M. J. (2022). Southern Ocean precipitation: Toward a process-level understanding. WIREs Climate Change, 13(6), e800. https://doi.org/10.1002/wcc.800

Sihto, S.-L., Kulmala, M., Kerminen, V.-M., Dal Maso, M., Petäjä, T., Riipinen, I., et al. (2006). Atmospheric sulphuric acid and aerosol formation: implications from atmospheric measurements for nucleation and early growth mechanisms. Atmospheric Chemistry and Physics, 6(12), 4079–4091. https://doi.org/10.5194/acp-6-4079-2006

Smalley, K. M., Lebsock, M. D., Eastman, R., Smalley, M., & Witte, M. K. (2022). A Lagrangian analysis of pockets of open cells over the southeastern Pacific. Atmospheric Chemistry and Physics, 22(12), 8197–8219. https://doi.org/10.5194/acp-22-8197-2022

Smith, W., & Minnis, P. (2018). NASA SatCORPS Himawari cloud retrieval data Version 2.1 (Version 2.1) [Data set]. UCAR/NCAR - Earth Observing Laboratory. https://doi.org/10.5065/D6CC0ZFJ

Spracklen, D. V., Pringle, K. J., Carslaw, K. S., Mann, G. W., Manktelow, P., & Heintzenberg, J. (2007). Evaluation of a global aerosol microphysics model against size-resolved particle statistics in the marine atmosphere. Atmospheric Chemistry and Physics, 7(8), 2073–2090. https://doi.org/10.5194/acp-7-2073-2007

Stephens, G. L., L'Ecuyer, T., Forbes, R., Gettelmen, A., Golaz, J.-C., Bodas-Salcedo, A., et al. (2010). Dreary state of precipitation in global models. Journal of Geophysical Research: Atmospheres, 115(D24). https://doi.org/10.1029/2010JD014532

Tan, I., Storelvmo, T., & Zelinka, M. D. (2016). Observational constraints on mixed-phase clouds imply higher climate sensitivity. Science, 352(6282), 224–227. https://doi.org/10.1126/science.aad5300

Tang, Q., Golaz, J.-C., Van Roekel, L. P., Taylor, M. A., Lin, W., Hillman, B. R., et al. (2023). The fully coupled regionally refined model of E3SM version 2: overview of the atmosphere, land, and river results. Geoscientific Model Development, 16(13), 3953–3995. https://doi.org/10.5194/gmd-16-3953-2023

Tang, S., Varble, A. C., Fast, J. D., Zhang, K., Wu, P., Dong, X., et al. (2023). Earth System Model Aerosol–Cloud Diagnostics (ESMAC Diags) package, version 2: assessing aerosols, clouds, and aerosol–cloud interactions via field campaign and long-term observations. Geoscientific Model Development, 16(21), 6355–6376. https://doi.org/10.5194/gmd-16-6355-2023

Tansey, E., Marchand, R., Alexander, S. P., Klekociuk, A. R., & Protat, A. (2023). Southern Ocean Low Cloud and Precipitation Phase Observed During the Macquarie Island Cloud and Radiation Experiment (MICRE). Journal of Geophysical Research: Atmospheres, 128(17), e2023JD039205. https://doi.org/10.1029/2023JD039205

Tansey, E., Marchand, R., Protat, A., Alexander, S. P., & Ding, S. (2022). Southern Ocean Precipitation Characteristics Observed From CloudSat and Ground Instrumentation During the Macquarie Island Cloud & Radiation Experiment (MICRE): April 2016 to March 2017. Journal of Geophysical Research: Atmospheres, 127(5), e2021JD035370. https://doi.org/10.1029/2021JD035370

Tansey, E., Marchand, R., Protat, A., Alexander, S. P., & Ding, S. (2022). Southern Ocean Precipitation Characteristics Observed From CloudSat and Ground Instrumentation During the Macquarie Island Cloud & Radiation Experiment (MICRE): April 2016 to March 2017. Journal of Geophysical Research: Atmospheres, 127(5), e2021JD035370. https://doi.org/10.1029/2021JD035370

Teng, Z.-J., Qin, Q.-L., Zhang, W., Li, J., Fu, H.-H., Wang, P., et al. (2021). Biogeographic traits of dimethyl sulfide and dimethylsulfoniopropionate cycling in polar oceans. Microbiome, 9(1), 207. https://doi.org/10.1186/s40168-021-01153-3

Terai, C. R., Wood, R., Leon, D. C., & Zuidema, P. (2012). Does precipitation susceptibility vary with increasing cloud thickness in marine stratocumulus? Atmospheric Chemistry and Physics, 12(10), 4567–4583. https://doi.org/10.5194/acp-12-4567-2012

Thompson, C. R., Wofsy, S. C., Prather, M. J., Newman, P. A., Hanisco, T. F., Ryerson, T. B., et al. (2022). The NASA Atmospheric Tomography (ATom) Mission: Imaging the Chemistry of the Global Atmosphere. Bulletin of the American Meteorological Society, 103(3), E761–E790. https://doi.org/10.1175/BAMS-D-20-0315.1

Tie, X., Brasseur, G., Emmons, L., Horowitz, L., & Kinnison, D. (2001). Effects of aerosols on tropospheric oxidants: A global model study. Journal of Geophysical Research: Atmospheres, 106(D19), 22931–22964. https://doi.org/10.1029/2001JD900206

Trenberth, K. E., & Fasullo, J. T. (2010). Simulation of Present-Day and Twenty-First-Century Energy Budgets of the Southern Oceans. Journal of Climate, 23(2), 440–454. https://doi.org/10.1175/2009JCLI3152.1

Twohy, C. H., DeMott, P. J., Russell, L. M., Toohey, D. W., Rainwater, B., Geiss, R., et al. (2021). Cloud-Nucleating Particles Over the Southern Ocean in a Changing Climate. Earth's Future, 9(3), e2020EF001673. https://doi.org/10.1029/2020EF001673

Twomey, S. (1977). The Influence of Pollution on the Shortwave Albedo of Clouds. Journal of the Atmospheric Sciences, 34(7), 1149–1152. https://doi.org/10.1175/1520-0469(1977)034<1149:TIOPOT>2.0.CO;2

UCAR/NCAR-Earth Observing Laboratory. (2022). SOCRATES: Low Rate (LRT - 1 sps) Navigation, State Parameter, and Microphysics Flight-Level Data. Version 1.4 [Dataset]. UCAR/NCAR - Earth Observing Laboratory. https://doi.org/10.5065/D6M32TM9

Ulbrich, C. W. (1983). Natural Variations in the Analytical Form of the Raindrop Size Distribution. Journal of Applied Meteorology and Climatology, 22(10), 1764–1775. https://doi.org/10.1175/1520-0450(1983)022<1764:NVITAF>2.0.CO;2

vanZanten, M. C., Stevens, B., Vali, G., & Lenschow, D. H. (2005). Observations of Drizzle in Nocturnal Marine Stratocumulus. Journal of the Atmospheric Sciences, 62(1), 88–106. https://doi.org/10.1175/JAS-3355.1

Varble, A. C., Ma, P.-L., Christensen, M. W., Mülmenstädt, J., Tang, S., & Fast, J. (2023). Evaluation of liquid cloud albedo susceptibility in E3SM using coupled eastern North Atlantic surface and satellite retrievals. Atmospheric Chemistry and Physics, 23(20), 13523–13553. https://doi.org/10.5194/acp-23-13523-2023

Vehkamäki, H., Kulmala, M., Napari, I., Lehtinen, K. E. J., Timmreck, C., Noppel, M., & Laaksonen, A. (2002). An improved parameterization for sulfuric acid–water nucleation rates for tropospheric and stratospheric conditions. Journal of Geophysical Research: Atmospheres, 107(D22), AAC 3-1-AAC 3-10. https://doi.org/10.1029/2002JD002184

Vivekanandan, J., Ellis, S., Tsai, P., Loew, E., Lee, W.-C., Emmett, J., et al. (2015). A wing pod-based millimeter wavelength airborne cloud radar. Geoscientific Instrumentation, Methods and Data Systems, 4(2), 161–176. https://doi.org/10.5194/gi-4-161-2015

Wang, H., & Feingold, G. (2009). Modeling Mesoscale Cellular Structures and Drizzle in Marine Stratocumulus. Part I: Impact of Drizzle on the Formation and Evolution of Open Cells. Journal of the Atmospheric Sciences, 66(11), 3237–3256. https://doi.org/10.1175/2009JAS3022.1

Wang, S., Maltrud, M., Elliott, S., Cameron-Smith, P., & Jonko, A. (2018). Influence of dimethyl sulfide on the carbon cycle and biological production. *Biogeochemistry*, *138*(1), 49–68. https://doi.org/10.1007/s10533-018-0430-5

Wang, Hailong, Easter, R. C., Zhang, R., Ma, P.-L., Singh, B., Zhang, K., et al. (2020). Aerosols in the E3SM Version 1: New Developments and Their Impacts on Radiative Forcing. Journal of Advances in Modeling Earth Systems, 12(1), e2019MS001851. https://doi.org/10.1029/2019MS001851

Wang, Haoran, Klekociuk, A. R., French, W. J. R., Alexander, S. P., & Warner, T. A. (2020). Measurements of Cloud Radiative Effect across the Southern Ocean (43° S–79° S, 63° E–158° W). Atmosphere, 11(9), 949. https://doi.org/10.3390/atmos11090949

Wang, M., & Penner, J. E. (2009). Aerosol indirect forcing in a global model with particle nucleation. Atmospheric Chemistry and Physics, 9(1), 239–260. https://doi.org/10.5194/acp-9-239-2009

Wang, W.-L., Song, G., Primeau, F., Saltzman, E. S., Bell, T. G., & Moore, J. K. (2020). Global ocean dimethyl sulfide climatology estimated from observations and an artificial neural network. Biogeosciences, 17(21), 5335–5354. https://doi.org/10.5194/bg-17-5335-2020

Wang, Y., McFarquhar, G. M., Rauber, R. M., Zhao, C., Wu, W., Finlon, J. A., et al. (2020). Microphysical Properties of Generating Cells Over the Southern Ocean: Results From SOCRATES. *Journal of Geophysical Research: Atmospheres*, *125*(13), e2019JD032237. https://doi.org/10.1029/2019JD032237

Wang, Y., Xia, W., Liu, X., Xie, S., Lin, W., Tang, Q., et al. (2021). Disproportionate control on aerosol burden by light rain. *Nature Geoscience*, *14*(2), 72–76. https://doi.org/10.1038/s41561-020-00675-z

Webb, A. L., van Leeuwe, M. A., den Os, D., Meredith, M. P., J. Venables, H., & Stefels, J. (2019). Extreme spikes in DMS flux double estimates of biogenic sulfur export from the Antarctic coastal zone to the atmosphere. Scientific Reports, 9(1), 2233. https://doi.org/10.1038/s41598-019-38714-4

Weber, R. J., Moore, K., Kapustin, V., Clarke, A., Mauldin, R. L., Kosciuch, E., et al. (2001). Nucleation in the equatorial Pacific during PEM-Tropics B: Enhanced boundary layer H2SO4 with no particle production. *Journal of Geophysical Research: Atmospheres*, *106*(D23), 32767–32776. https://doi.org/10.1029/2001JD900250

Wilks, D. S. (1997). Resampling Hypothesis Tests for Autocorrelated Fields. Journal of Climate, 10(1), 65–82. https://doi.org/10.1175/1520-0442(1997)010<0065:RHTFAF>2.0.CO;2

Williamson, C. J., Kupc, A., Axisa, D., Bilsback, K. R., Bui, T., Campuzano-Jost, P., et al. (2019). A large source of cloud condensation nuclei from new particle formation in the tropics. Nature, 574(7778), 399–403. https://doi.org/10.1038/s41586-019-1638-9

Wiscombe, J. (1979). Mie Scattering Calculations: Advances in Technique and Fast, Vector-speed Computer Codes. https://doi.org/10.5065/D6ZP4414

Wood, R. (2005). Drizzle in Stratiform Boundary Layer Clouds. Part II: Microphysical Aspects. Journal of the Atmospheric Sciences, 62(9), 3034–3050. https://doi.org/10.1175/JAS3530.1

Wood, R. (2012). Stratocumulus Clouds. Monthly Weather Review, 140(8), 2373–2423. https://doi.org/10.1175/MWR-D-11-00121.1

Wood, R., Bretherton, C. S., Leon, D., Clarke, A. D., Zuidema, P., Allen, G., & Coe, H. (2011). An aircraft case study of the spatial transition from closed to open mesoscale cellular convection over the Southeast Pacific. Atmospheric Chemistry and Physics, 11(5), 2341–2370. https://doi.org/10.5194/acp-11-2341-2011

Wood, Robert, Leon, D., Lebsock, M., Snider, J., & Clarke, A. D. (2012). Precipitation driving of droplet concentration variability in marine low clouds. Journal of Geophysical Research: Atmospheres, 117(D19). https://doi.org/10.1029/2012JD018305

Wood, Robert. (2006). Rate of loss of cloud droplets by coalescence in warm clouds. *Journal of Geophysical Research: Atmospheres*, *111*(D21). https://doi.org/10.1029/2006JD007553

Wu, W., & McFarquhar, G. (2019). NSF/NCAR GV HIAPER 2D-S Particle Size Distribution (PSD) Product Data. Version 1.1 (Version 1.1) [Dataset]. UCAR/NCAR - Earth Observing Laboratory. https://doi.org/10.26023/8HMG-WQP3-XA0X

Wyant, M. C., Bretherton, C. S., Wood, R., Blossey, P. N., & McCoy, I. L. (2022). High Free-Tropospheric Aitken-Mode Aerosol Concentrations Buffer Cloud Droplet Concentrations in

Large-Eddy Simulations of Precipitating Stratocumulus. Journal of Advances in Modeling Earth Systems, 14(6), e2021MS002930. https://doi.org/10.1029/2021MS002930

Xie, S., Lin, W., Rasch, P. J., Ma, P.-L., Neale, R., Larson, V. E., et al. (2018). Understanding Cloud and Convective Characteristics in Version 1 of the E3SM Atmosphere Model. Journal of Advances in Modeling Earth Systems, 10(10), 2618–2644. https://doi.org/10.1029/2018MS001350

Xu, J., Zhang, J., Liu, J., Yi, K., Xiang, S., Hu, X., et al. (2019). Influence of cloud microphysical processes on black carbon wet removal, global distributions, and radiative forcing. *Atmospheric Chemistry and Physics*, *19*(3), 1587–1603. https://doi.org/10.5194/acp-19-1587-2019

Yamaguchi, T., & Feingold, G. (2015). On the relationship between open cellular convective cloud patterns and the spatial distribution of precipitation. Atmospheric Chemistry and Physics, 15(3), 1237–1251. https://doi.org/10.5194/acp-15-1237-2015

Yang, F., Luke, E. P., Kollias, P., Kostinski, A. B., & Vogelmann, A. M. (2018). Scaling of drizzle virga depth with cloud thickness for marine stratocumulus clouds. Geophysical Research Letters, 45(8), 3746–3753. https://doi.org/10.1029/2018GL077145

Yum, S. S., & Hudson, J. G. (2004). Wintertime/summertime contrasts of cloud condensation nuclei and cloud microphysics over the Southern Ocean. *Journal of Geophysical Research: Atmospheres*, *109*(D6). https://doi.org/10.1029/2003JD003864

Zelinka, M. D., Myers, T. A., McCoy, D. T., Po-Chedley, S., Caldwell, P. M., Ceppi, P., et al. (2020). Causes of Higher Climate Sensitivity in CMIP6 Models. Geophysical Research Letters, 47(1), e2019GL085782. https://doi.org/10.1029/2019GL085782

Zhang, D., Wang, Z., Luo, T., Yin, Y., & Flynn, C. (2017). The occurrence of ice production in slightly supercooled Arctic stratiform clouds as observed by ground-based remote sensors at the ARM NSA site. Journal of Geophysical Research: Atmospheres, 122(5), 2867–2877. https://doi.org/10.1002/2016JD026226

Zhang, G. J., & McFarlane, N. A. (1995). Sensitivity of climate simulations to the parameterization of cumulus convection in the Canadian climate centre general circulation model. Atmosphere-Ocean, 33(3), 407–446. https://doi.org/10.1080/07055900.1995.9649539

Zhang, L., Gong, S., Padro, J., & Barrie, L. (2001). A size-segregated particle dry deposition scheme for an atmospheric aerosol module. Atmospheric Environment, 35(3), 549–560. https://doi.org/10.1016/S1352-2310(00)00326-5

Zhao, C., & Garrett, T. J. (2015). Effects of Arctic haze on surface cloud radiative forcing. *Geophysical Research Letters*, *42*(2), 557–564. https://doi.org/10.1002/2014GL062015

Zhao, J., Zhang, Y., Bie, S., Yang, G.-P., Bilsback, K. R., Pierce, J. R., & Chen, Y. (2024). Improving Estimates of Dynamic Global Marine DMS and Implications for Aerosol Radiative Effect. Journal of Geophysical Research: Atmospheres, 129(2), e2023JD039314. https://doi.org/10.1029/2023JD039314

Zhao, L., Zhao, C., Wang, Y., Wang, Y., & Yang, Y. (2020). Evaluation of Cloud Microphysical Properties Derived From MODIS and Himawari-8 Using In Situ Aircraft Measurements Over the

Southern Ocean. *Earth and Space Science*, *7*(5), e2020EA001137. https://doi.org/10.1029/2020EA001137

Zheng, G., Wang, Y., Aiken, A. C., Gallo, F., Jensen, M. P., Kollias, P., et al. (2018). Marine boundary layer aerosol in the eastern North Atlantic: seasonal variations and key controlling processes. *Atmospheric Chemistry and Physics*, *18*(23), 17615–17635. https://doi.org/10.5194/acp-18-17615-2018

Zhou, X., Atlas, R., McCoy, I. L., Bretherton, C. S., Bardeen, C., Gettelman, A., et al. (2021). Evaluation of Cloud and Precipitation Simulations in CAM6 and AM4 Using Observations Over the Southern Ocean. Earth and Space Science, 8(2), e2020EA001241. https://doi.org/10.1029/2020EA001241

Appendix A: Chapter 2 Supplemental Information

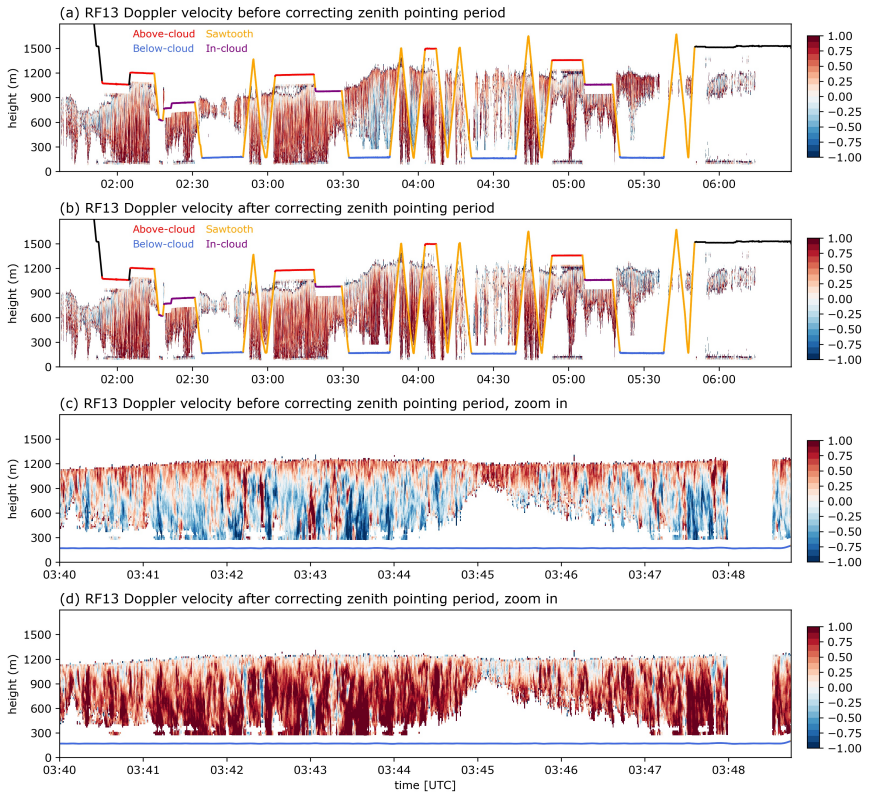

Figure A 1. An example of the zenith pointing Doppler velocity fields from RF13 (a) before and (b) after the correction of the zenith pointing data, as well as the zoom-in view for the zenith-pointing period starting from 03:40 UTC (c) before and (d) after the correction.

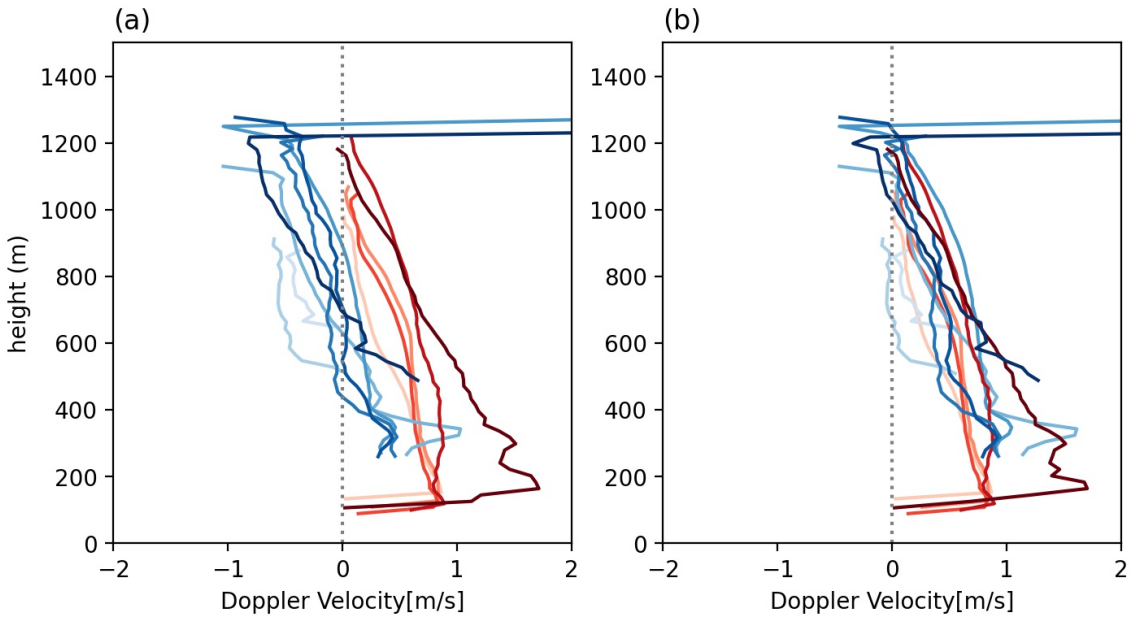

Figure A 2. Mean velocity profiles for nadir pointing and zenith pointing data from RF13 (a) before the correcting and (b) after the correcting the zenith pointing data. Here each profile represents the average mean velocity profile averaged over either nadir pointing times (denoted as red) or zenith pointing times (denoted as blue). The vertical dashed line represents the 0 m s^{-1} for reference.

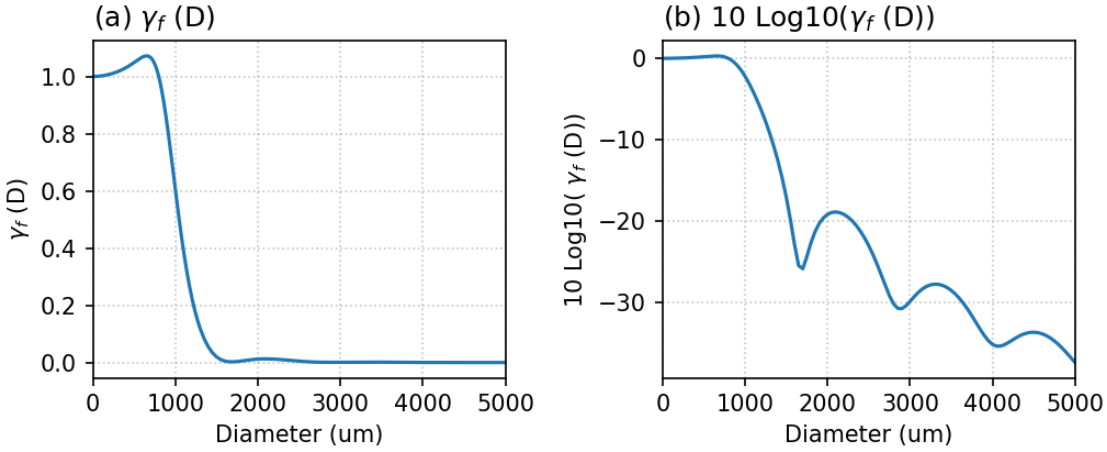

Figure A 3. The Mie-to-Rayleigh backscatter ratio (a) $\gamma_f(D)$, and (b) 10 $\log_{10}(\gamma_f(D))$. $\gamma_f(D)$ is the ratio of the backscatter efficiency of Mie scattering for W-band (94-GHz), calculated using the miepython package based on Wiscombe(1979), and the backscatter efficiency of Rayleigh scattering (Bohren & Huffman, 1983).

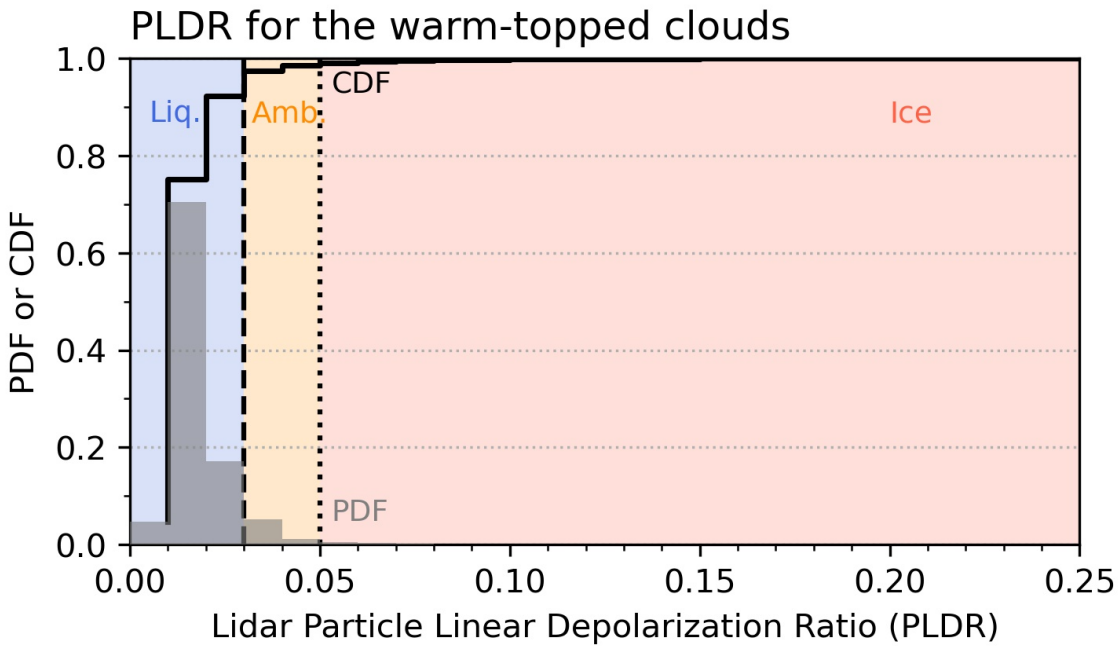

Figure A 4. Probability and cumulative density functions of below-cloud lidar particle linear depolarization ratio (PLDR) for all warm-topped clouds (when cloud top temperature > 0°C). To distinguish different precipitation types, liquid precipitation is marked as blue, ice precipitation is marked as red, and ambiguous precipitation is marked as orange.

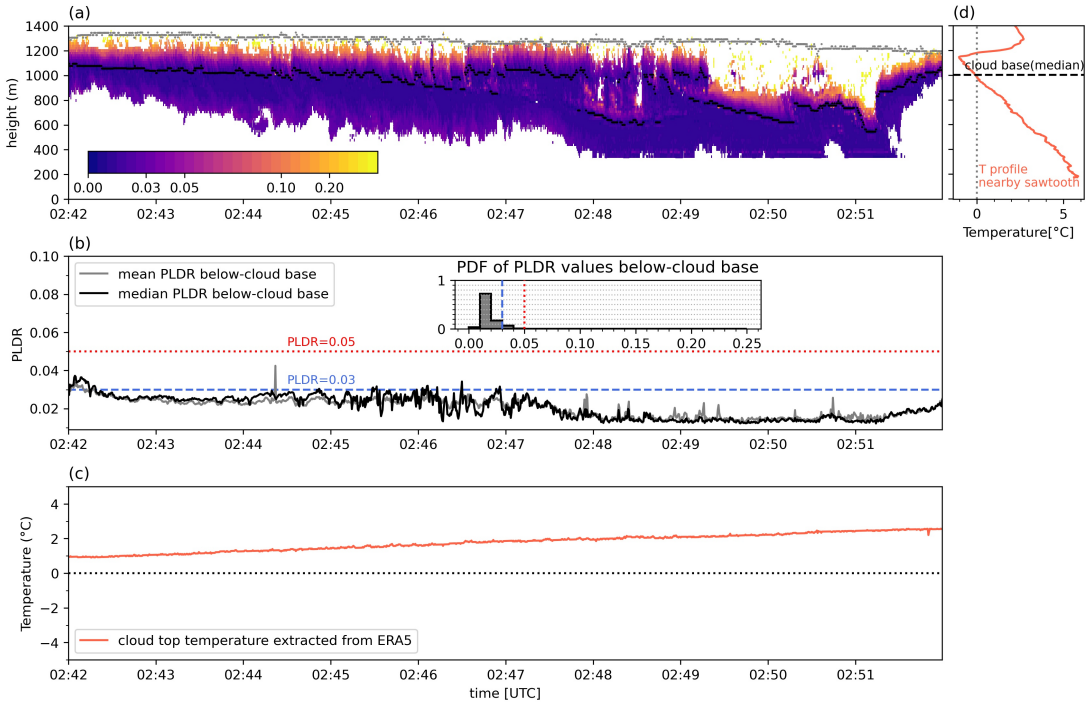

Figure A 5. An example case from research flight 10 (RF10) on 2018 Feb. 8th during 02:42-02:52 UTC with (a) lidar particle linear depolarization ratio (PLDR), (b) time series of median PLDR (black) or mean PLDR (grey) values below-cloud base, and the probability density

function (PDF) of PLDR values below-cloud base, (c) the cloud top temperature extracted from ERA5 reanalysis data, and (d) temperature profile measured by aircraft from an adjacent sawtooth leg (2018 Feb. 8th during 02:52-02:58 UTC). The grey dotted line in panels c and d represents 0°C for reference. The blue and red line on panel b shows the threshold or PLDR equals 0.03 or 0.05.

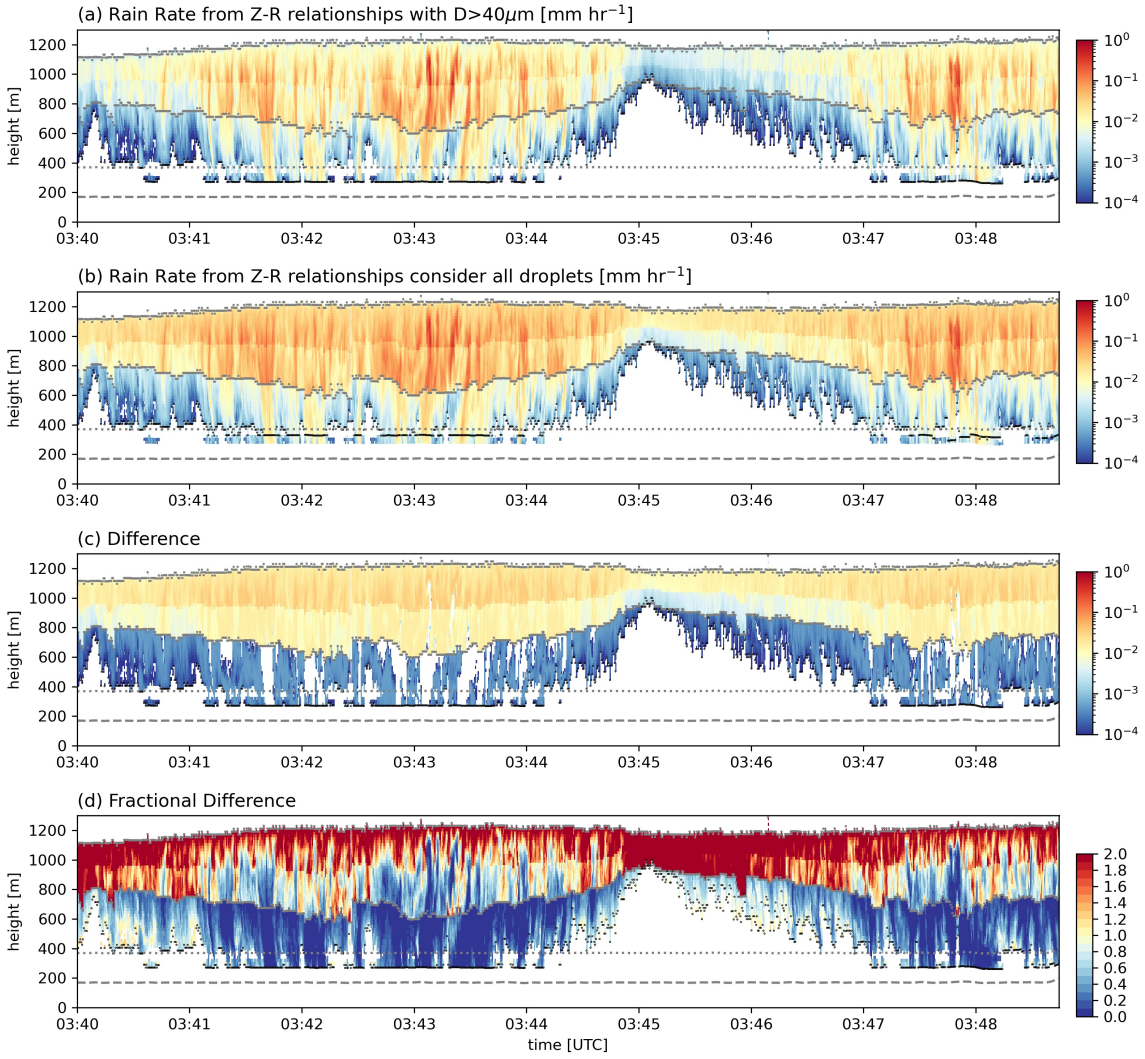

Figure A 6. Z-R relationships derived rain rate. Panel a uses the Z-R relationships that have D >40 μm cutoff, while Z-R relationships used in panel b do not apply any cutoff, and consider all droplet sizes. Panel c shows the difference calculated as $RR_{panel\ b} - RR_{panel\ a}$. Panel d shows the fractional difference calculated as $(RR_{panel\ b} - RR_{panel\ a}) / RR_{panel\ a}$

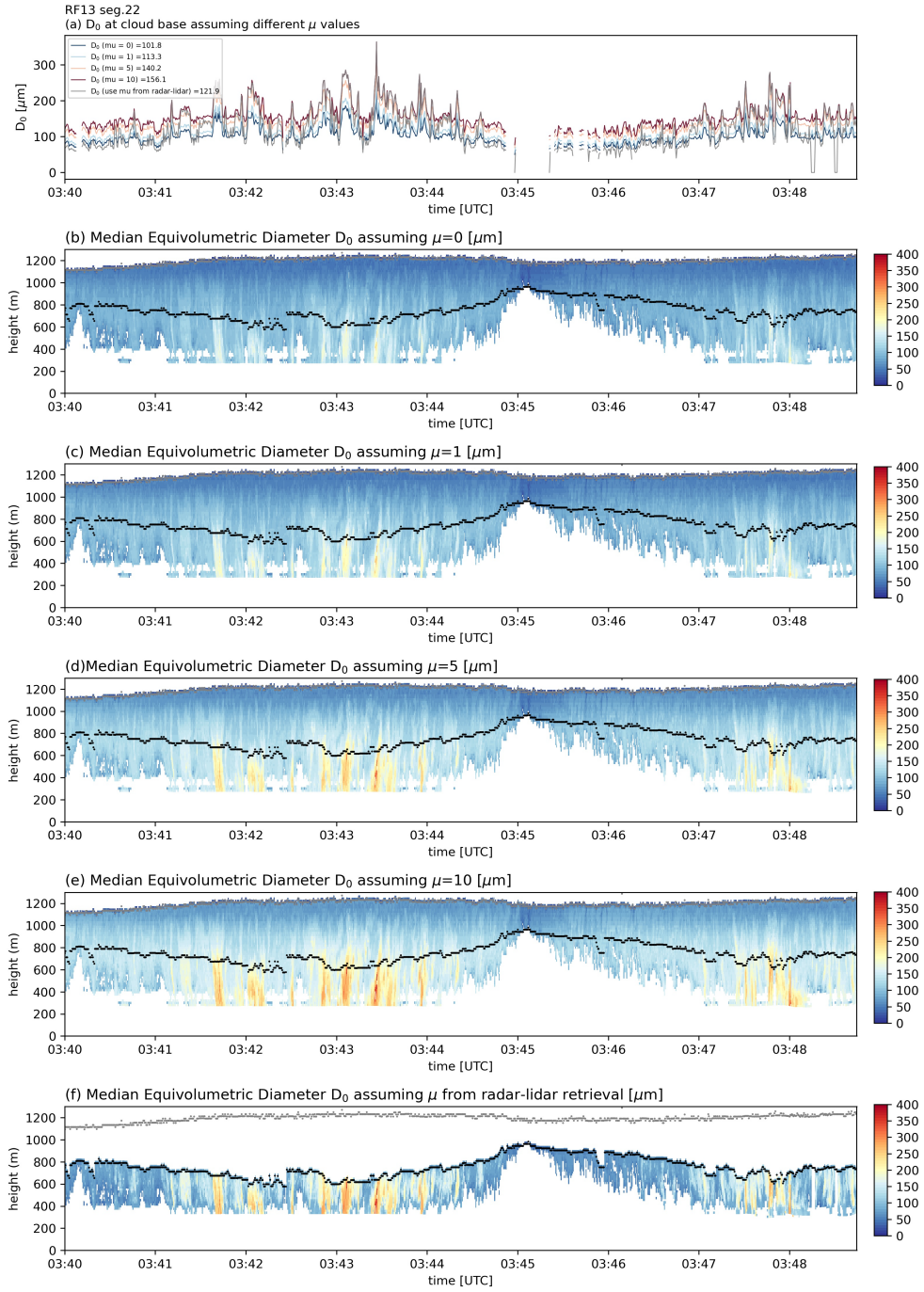

Figure A 7. ZV retrieved median equivolumetric diameter D_0 assuming different shape factor

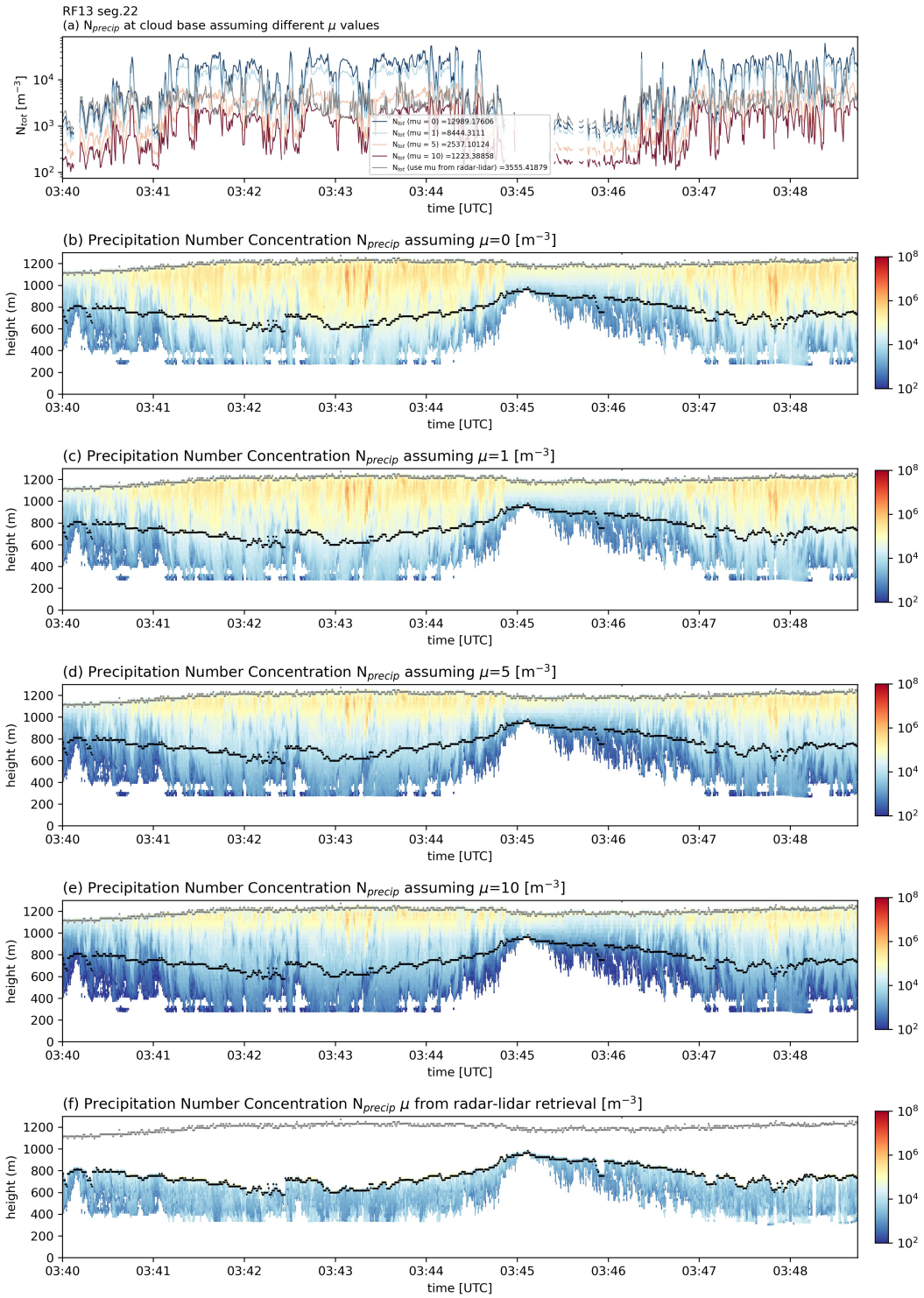

Figure A 8. ZV retrieved median equivolumetric diameter N_{precip} assuming different shape factor

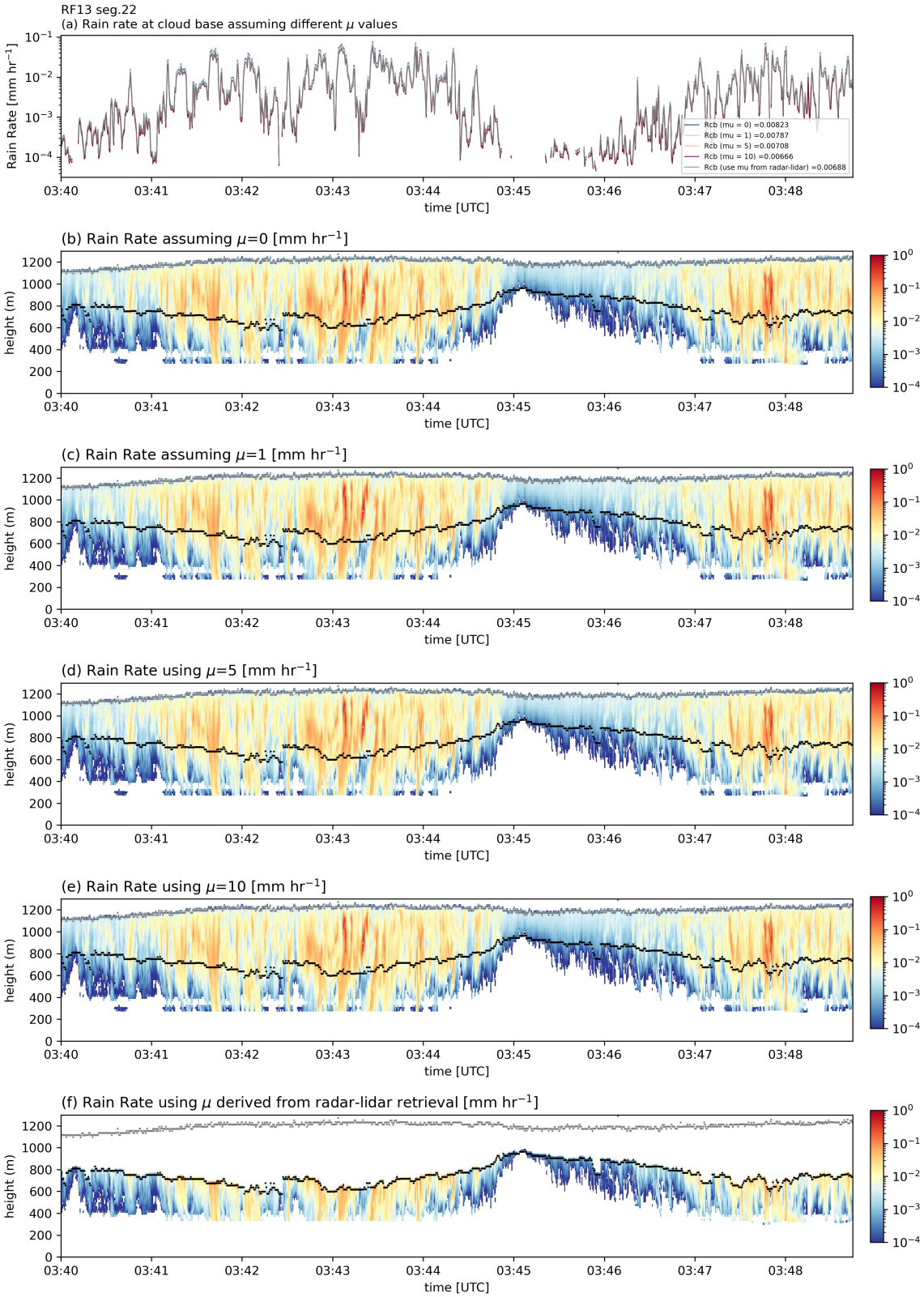

Figure A 9. ZV retrieved rain rate assuming different shape factor

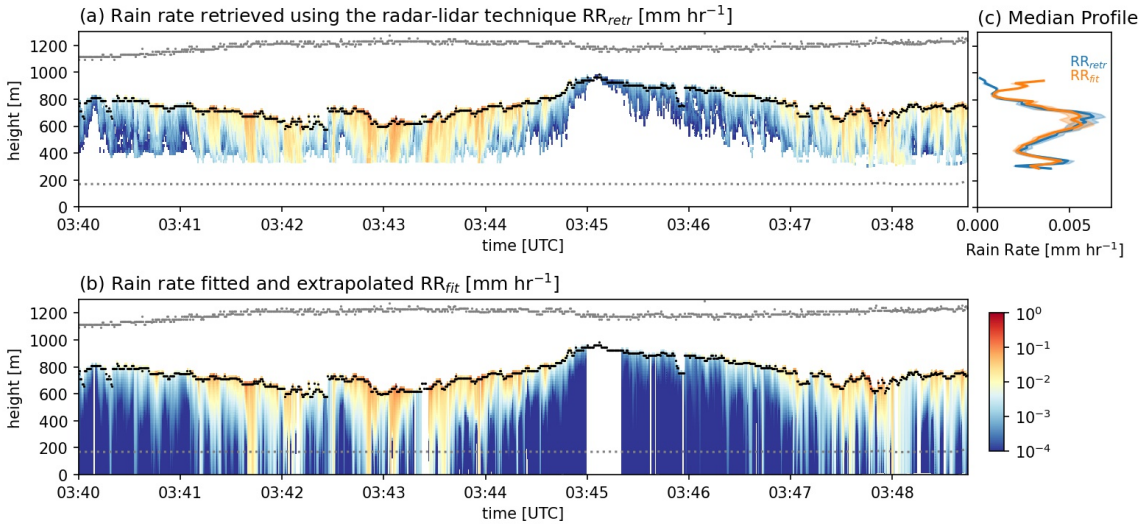

Figure A 10. An example case with (a) radar-lidar retrieved rain rate, (b) rain rate derived from the exponential fitting the retrieved rain rates and extrapolated to the aircraft level (marked as the dashed line), and (c) median rain rate profiles of from radar-lidar retrieval (blue) or exponentially fit (orange). In the panel c, the median profiles are calculated over the area where radar-lidar retrieved rain rates are available.

Appendix B: Chapter 3 Supplemental Information

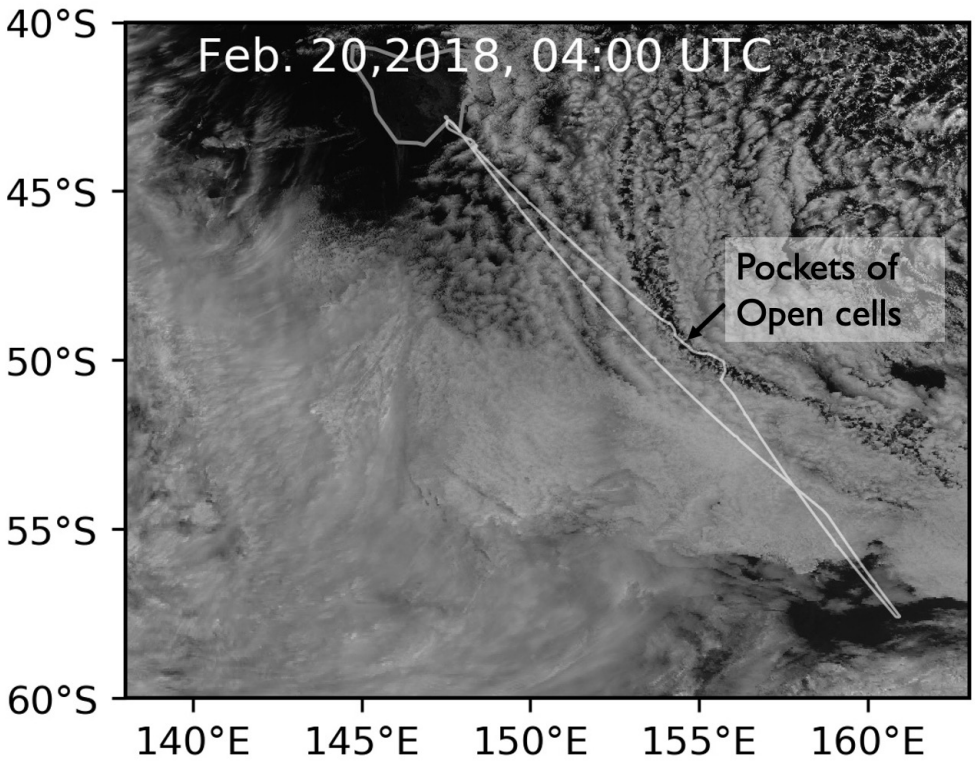

Figure B 1. Himawari-8 visible image for RF13 (Feb. 20, 4:00 UTC). The white line shows the flight track of the aircraft.

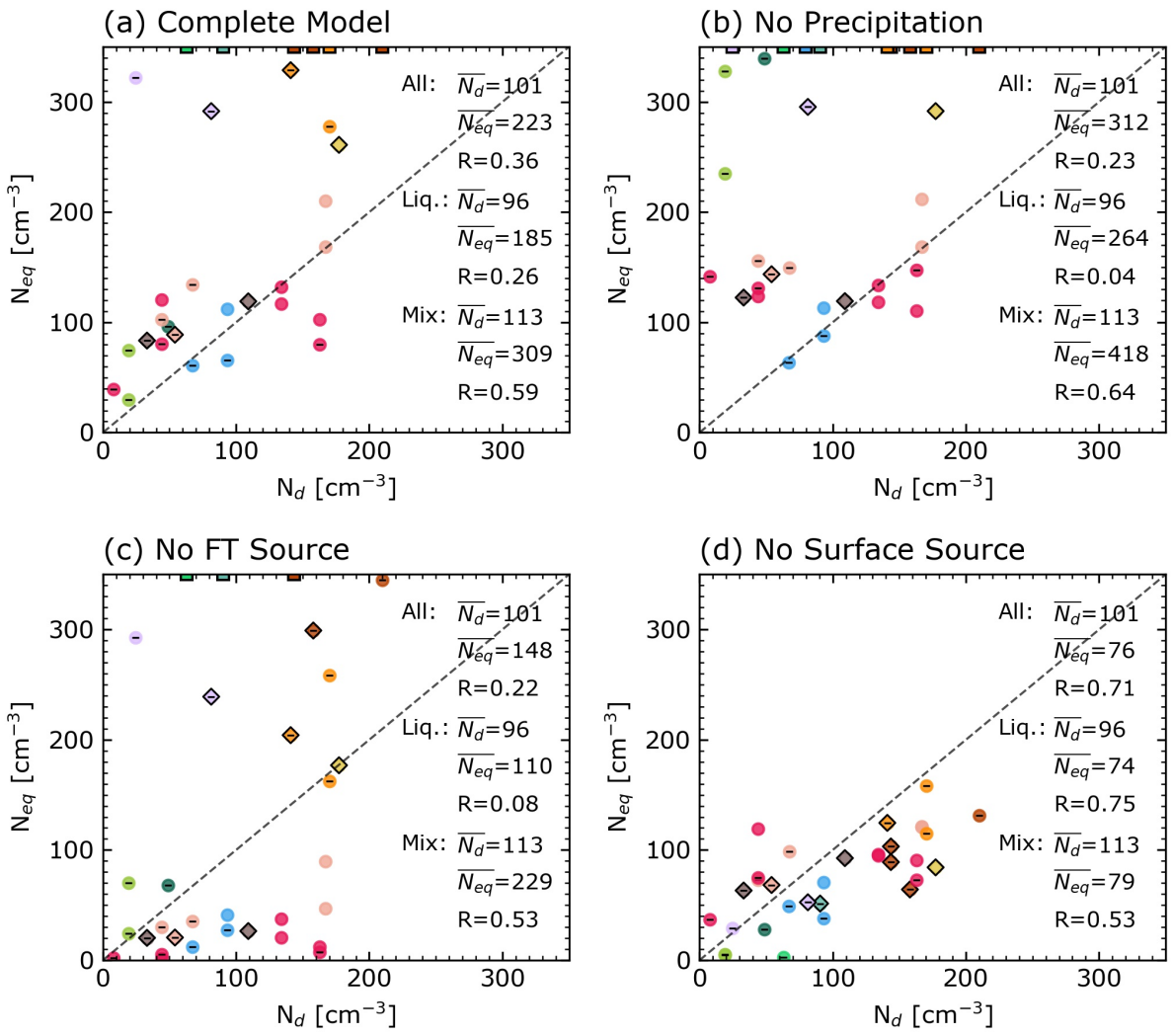

Figure B 2. Comparison between observed N_d and computed N_{eq} using the budget model for SOCRATES flights with $\boldsymbol{U_{10}^{3.41}}$ in the surface source parametrization: (a) with all the source and sink terms, (b) without the precipitation sink, (c) without the free tropospheric source, and (d) without the surface source. Cases with N_{eq} > 350 cm^{-3} are shown as having a concentration of 350 cm^{-3} (affixed to the top of the plot). Different colors represent different flights. Black hyphens marked the cases with rain rate > 0.001 mm h^{-1}. Circular points are cases associated with liquid precipitation. Black diamonds are the cases associated with ice precipitation, and, for these cases, retrieved rain rates from liquid-column are used in the budget model.

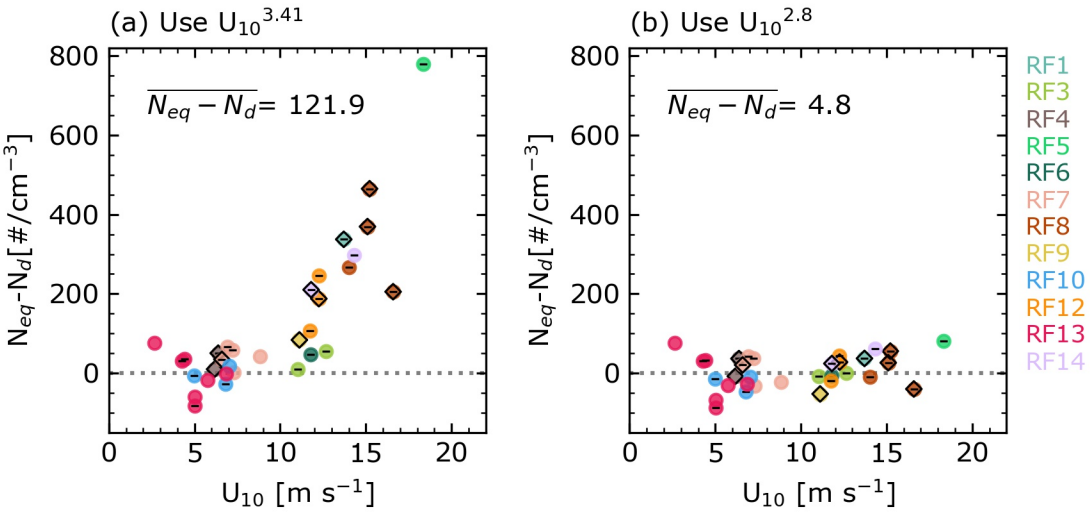

Figure B 3. The difference between predicted N_{eq} and observed N_d as a function of surface wind speed at 10m using (a) $U_{10}^{3.41}$ or (b) $U_{10}^{2.8}$ in the surface source parametrization for the budget model. Different colors represent different flights. Black hyphens marked the cases with rain rate > 0.001 mm h^{-1}. Circular points are cases associated with liquid precipitation. Black diamonds are the cases associated with ice precipitation, and, for these cases, retrieved rain rates from liquid-columns are used in the budget model.

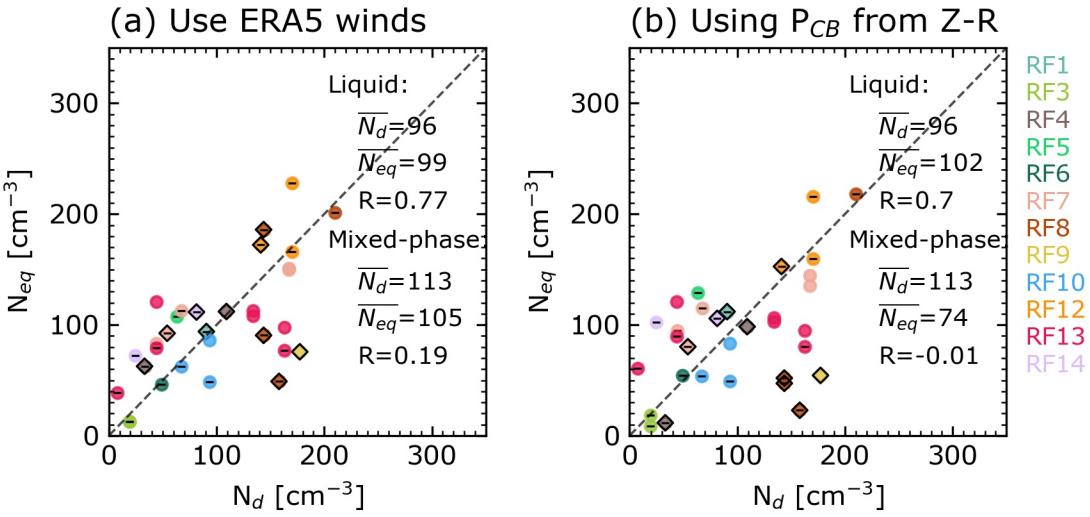

Figure B 4. Comparison between observed N_d and computed N_{eq} using the budget model for SOCRATES flights with (a) ERA5 surface wind speed or (b) precipitation rate at the cloud base estimated using a simple radar reflectivity to rain rate (Z-R) relationship developed by Comstock et al. (2004). Circular points are cases associated with liquid precipitation. Black diamonds are the cases associated with ice precipitation, and, for these cases, retrieved rain rates from liquid

columns are used in the budget model in panel a, while in panel b rain rates are derived from the Z-R relationship.

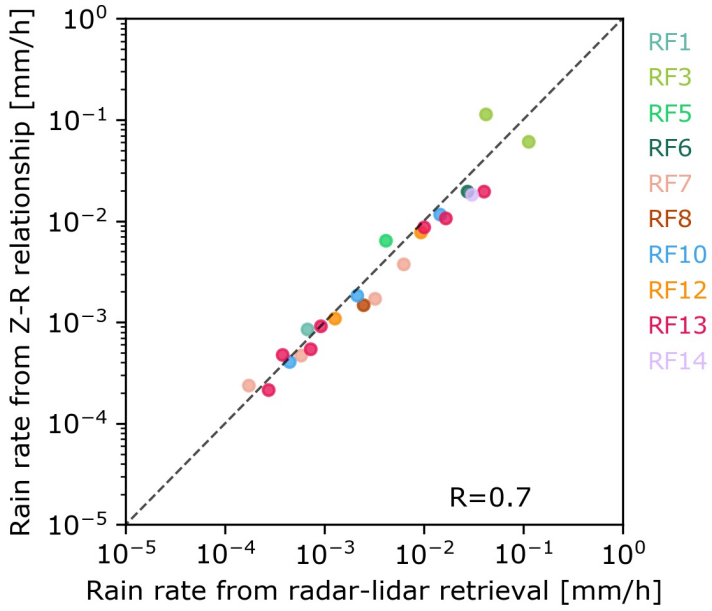

Figure B 5. Comparison for liquid cases between rain rate retrieved based on the radar-lidar technique of O'Connor et al. (2005) with rain rate derived using the Z-R relationship developed by Comstock et al. (2004). Different colors represent different flights.

Table B1 Summary of the cases used in this study

RF	Below-cloud leg							Above-cloud leg(nearby)	Sawtooth leg(nearby)	
	Date	Start Time	End Time	Retrieved P_{CB} [mm/h]	Phase	U_{10} [m/s]	Sea Spray aerosol concentration calculated using parametrization [cm^{-3}]	N_{FT} [cm^{-3}]	Cloud depth [m]	N_d [cm^{-3}]
1	2018/1/16	2:27	2:36	0.00305	mixed	13.7[13.5-14.0]	81.7[77.7-86.4]	55[22-100]	150	91[83-100]
3	2018/1/22	23:56	0:02	0.11259	liquid	11.0[10.7-11.4]	44.4[41.2-48.7]	43[35-50]	392	19[13-27]
3	2018/1/23	1:19	1:29	0.04233	liquid	12.7[12.3-13.1]	65.3[60.0-71.3]	21[15-26]	513	19[16-22]
4	2018/1/24	3:40	3:47	9.00E-05	mixed	6.2[5.9-6.4]	8.7[7.9-9.7]	93[84-102]	115	109[101-124]
4	2018/1/24	3:47	3:52	0.00275	mixed	6.4[6.0-6.7]	9.6[8.3-11.1]	93[84-102]	1092	33[26-40]
5	2018/1/26	2:30	2:32	0.00415	liquid	18.3[18.0-18.5]	184.3[174.8-189.5]	3[0-4]	455	63[49-80]
6	2018/1/29	1:54	2:04	0.02755	liquid	11.8[11.4-12.2]	53.4[48.7-58.9]	99[87-110]	588	49[84-135]
7	2018/1/31	4:34	4:42	0.00627	liquid	7.2[6.8-7.6]	13.6[11.5-15.7]	110[101-120]	531	44[34-53]
7	2018/1/31	4:49	4:51	0.00322	liquid	6.9[6.7-7.1]	12.1[11.2-13.2]	110[101-120]	232	67[59-82]
7	2018/1/31	5:03	5:11	0.02612	mixed	6.6[6.1-7.1]	10.5[8.6-12.7]	110[101-120]	152	54[50-59]
7	2018/1/31	6:30	6:41	0.00058	liquid	8.8[8.4-9.3]	23.9[20.9-27.2]	122[112-131]	88	167[154-209]
7	2018/1/31	6:44	6:54	0.00017	liquid	7.3[7.0-7.6]	14.0[12.4-15.9]	122[112-131]	88	167[154-209]
8	2018/2/4	3:12	3:22	0.00246	liquid	14.0[13.6-14.5]	87.1[79.4-96.1]	166[145-188]	687	210[170-251]
8	2018/2/4	4:00	4:14	0.01482	mixed	16.6[15.7-17.5]	139.3[119.7-161.4]	166[145-188]	687	158[87-212]
8	2018/2/4	5:01	5:07	0.00111	mixed	15.2[14.5-16.0]	109.4[94.7-125.9]	118[105-128]	804	144[101-191]
8	2018/2/4	5:07	5:11	0.00256	mixed	15.1[14.4-15.8]	106.9[93.9-121.5]	118[105-128]	804	144[101-191]
9	2018/2/5	3:24	3:31	0.00078	mixed	11.1[10.5-11.8]	45.5[38.8-53.1]	94[84-105]	961	177[112-217]
10	2018/2/8	2:39	2:42	0.00044	liquid	7.0[6.7-7.5]	12.6[10.8-14.8]	72[46-92]	148	93[81-108]
10	2018/2/8	2:42	2:52	0.0145	liquid	6.8[6.5-7.1]	11.4[10.1-13.0]	51[39-62]	148	93[81-108]
10	2018/2/8	3:40	3:45	0.00213	liquid	5.0[4.6-5.3]	4.8[3.9-5.7]	51[39-62]	132	67[61-79]
12	2018/2/18	3:42	3:52	0.00571	mixed	12.3[11.8-12.8]	59.7[53.1-67.0]	168[151-191]	391	141[123-166]
12	2018/2/18	4:46	4:54	0.00126	liquid	12.2[11.5-12.9]	59.6[50.2-69.5]	168[151-191]	318	170[151-202]
12	2018/2/18	4:54	5:08	0.00925	liquid	11.7[11.1-12.3]	52.8[45.4-60.2]	168[151-191]	318	170[151-202]
13	2018/2/20	2:34	2:46	0.00027	liquid	6.9[6.3-7.3]	11.8[9.4-13.9]	96[83-106]	248	134[121-148]
13	2018/2/20	2:46	2:50	0.00038	liquid	5.8[5.5-6.0]	7.2[6.4-8.0]	98[72-126]	248	134[121-148]
13	2018/2/20	3:32	3:40	0.00092	liquid	5.0[4.7-5.4]	4.9[4.0-6.1]	98[72-126]	538	163[145-190]
13	2018/2/20	3:40	3:48	0.01008	liquid	5.0[4.7-5.4]	4.9[4.0-6.1]	134[123-145]	538	163[145-190]
13	2018/2/20	4:21	4:30	0.04025	liquid	4.3[4.0-4.5]	3.1[2.7-3.6]	134[123-145]	417	8[2-10]
13	2018/2/20	4:30	4:39	0.01653	liquid	4.4[4.1-4.9]	3.5[2.7-4.6]	122[112-134]	244	44[24-58]
13	2018/2/20	5:20	5:38	0.00073	liquid	2.6[2.3-3.0]	0.8[0.6-1.1]	122[112-134]	244	44[24-58]
14	2018/2/22	3:09	3:24	0.03048	liquid	14.3[14.0-14.7]	92.3[87.1-98.4]	47[39-53]	126	25[14-33]
14	2018/2/22	4:16	4:32	0.0019	mixed	11.8[11.2-12.4]	53.7[46.9-61.4]	53[38-68]	44	81[38-118]

Note: Here precipitation phase is determined from the lidar particle linear depolarization ratio as described in Section 2. Sea Spray aerosol concentration is calculated based on the parametrization (i.e., the 2nd term on the numerator in equation 3.2). For Wind Speed at 10m(U_{10}), Sea Spray aerosol concentration, N_{FT} and N_d, the values are presented as mean [25th-75th percentile].

Table B2 Summary of the statistics of observed N_d and calculated N_{eq} for various model configurations

Model Configurations or Observation	All Cases (N=32)			Liquid precip. Cases (N=22)			Mixed-phase precip. Cases (N=10)		
	Mean [cm^{-3}]	R	Bias [cm^{-3}]	Mean	R	Bias [cm^{-3}]	Mean	R	Bias [cm^{-3}]
Observations	101	-	-	96	-	-	113	-	-
Model, complete	106	0.72	5	97	0.72	1	126	0.7	13
Model, no precip.	144	0.53	43	133	0.48	37	169	0.67	56
Model, no FT source	31	0.26	-71	23	0.14	-73	47	0.53	-66
Model, no Surface source	76	0.71	-26	74	0.75	-22	79	0.53	-34
Model, complete, use ERA5 winds	101	0.66	-1	99	0.77	3	105	0.19	-9
Model, complete use P_{CB} derived from Z-R relationship	93	0.49	-8	102	0.7	6	74	-0.01	-39
Model, complete, using $U_{10}^{3.41}$ in the surface source parametrization	223	0.36	122	185	0.26	89	309	0.59	195

Note: Here R is the correlation coefficient between observed N_d and calculated N_{eq} at 95% confidence, and bias is the mean of N_{eq} minus the mean of N_d.

Acknowledgements

Reflecting on my journey thus far, I would like to express my deepest gratitude to my advisor, Roger Marchand, for being an amazing mentor and role model to me. I am grateful for the opportunity to be his student and for his exceptional mentorship, guidance, and unwavering support. I am immensely thankful for his willingness to invest his time and for his genuine care for students' well-being and development, which has been instrumental in my academic pursuits and personal growth. I am also grateful for the opportunity to participate in the field campaign, which not only enriched my research journey but also helped me gain a real-life perspective on the data we use. Moreover, I appreciate the thoroughness and rigor of Roger's approach to science, which is a testament to his dedication and character.

I would like to express heartfelt appreciation for my co-advisor, Rob Wood. Many feedback and insights he shared along the way have been invaluable in shaping my understanding during the research. One aspect of Rob's mentorship that I hold in high regard is his Socratic style of learning and teaching through asking thought-provoking questions, which has challenged me to think about science differently and has fostered further exploration. Rob is another role model for me, showing how to be professionally exceptional, but also remain approachable, supportive, and genuinely caring.

I would also like to extend my gratitude to my other committee members: Qiang Fu, Lynn McMurdie, and Kevin Jamieson, for their invaluable feedback on my defense and dissertation. A special thanks go to Qiang for his timely encouragement this January.

I would like to express my gratitude to several people who have played pivotal roles in my journey. Firstly, I extend my gratitude to Thomas Ackerman. Our paths first crossed in 2015 during Tom and Linda's visit to Lanzhou University, where I had the privilege of serving as their tour guide. Tom encouraged me to apply to UW if I would like to pursue a Ph.D. Little did Tom know then that he would embark on an adventure along the Yellow River on a sheepskin raft in Lanzhou, just as I could never have imagined flying across the Pacific to Seattle and experiencing this incredible journey. I am also grateful to Professor Kenneth Carslaw at the University of Leeds. I took several classes taught by him when I was in a one-year study abroad program. His lectures and research inspired me to pursue a career in atmospheric science, particularly in the study of aerosols and clouds. Moreover, I wish to express my appreciation to Professor Jianping Huang and Siyu Chen, my advisors at Lanzhou University. They were my first mentors in the field and taught me how to do research and write the very first paper in my life.

I would like to thank my collaborators during my time in graduate school: Isabel McCoy, Po-Lun Ma, Meng Huang, Becky Alexander, Ursula Jongebloed, Zhihua Zheng, Qi Ge, Aaron Donohoe, Gerard Roe, Kyle Armour, and William Smith. I am deeply thankful for the opportunity to work with such a talented group of people. Special thanks to Gerard and Kyle for encouraging me and Zhihua to work with Qi on the undergraduate research project. I would like to extend my

appreciation to Po-Lun and Meng for their dedicated efforts in the model development and running the simulations for the diagnosis.

I am very grateful to our department for creating a collegial and supportive environment and for many staff working behind the scenes to support students. I would like to thank Roger's research group for always being there and providing feedback. Special thanks to my friend Emily Tansey. I am grateful that we are in the same group and started graduate school the same year, supporting each other along the way. I am also very grateful for my cohort grad 17, who are the first group of friends that I have made in Seattle.

I am deeply grateful to all my friends who have consistently provided support, joy, and love throughout my graduate school journey. I give special thanks to my dear friend, Zekun Sun. We started graduate school together and shared countless highs and lows. Her encouragement during challenging times was invaluable, and I don't think I could have come this far without her support. She is truly a role model for me in many ways, and I especially appreciate her courage and integrity. I am grateful for this gift of friendship and for her honest words that help me grow as a person. I am also grateful to my faithful friend, Zijun Wu, whose unwavering love and care have been a constant source of strength for me. I have lost count of the times she has offered her encouragement, lifting my spirits through challenges. I am also thankful for Zening Qu, whose companionship has been invaluable. Her passion for research is truly inspiring and has motivated me to strive for excellence in academic endeavors. I am also thankful for Ping-Ping Narenpitak, Diane Yoon, Ebenezer Prasanna, David Simmons, Yue Dong, Xiaoli Zhou, Shuting Zhai, Muting Chien, Yanlin Li, Joanna Tien, Nixi Wang, Jinze Zheng, Heidi Chaffee, John Chaffee, Kristina Chaffe, Qiao Cui, Jenny Lee, Sabrina Wang, and Yajun Wu, for their love and for many joyful times we spent together. I extend my gratitude to Daniel Chin, Ellen Chin, Danny Geng, and Judy Zhang, who have consistently supported me, imparting their wisdom on life's journey and setting admirable examples in the path of faith. Finally, I am grateful to my housemates and friends from various communities. Despite the rainy days in Seattle, the joyful memories we created together are a gift I hold dear.

Lastly, I express my heartfelt gratitude to my father and mother, for giving me the gift of life, and for their unwavering love and support throughout my life.

I would like to end with a haiku for the Southern Ocean clouds, which are created so beautifully. It is a humbling and awe-inspiring experience to study them.

Born, shine brightly, rain lightly.

Dance with water, wind, and wanderers.

It's not a bad life.